# The β-phase of Pigment Red 170: Structure Determination and Disorder Modelling

**Dissertation**

zur

Erlangung der naturwissenschaftlichen Doktorwürde

(Dr. sc. nat.)

vorgelegt der

Mathematisch-naturwissenschaftlichen Fakultät

der

**Universität Zürich**

von

**Rangana Warshamanage**

aus Sri Lanka

Promotionskomitee:

Prof. Dr. Anthony Linden (Vorsitz)

Prof. Dr. Hans-Beat Bürgi

Prof. Dr. Karl-Heinz Ernst

Zürich, 2014

## Acknowledgements

I wish to express my sincere gratitude to following people and organizations for their support during this work.

Prof. Dr. Anthony Linden for giving me the opportunity to undertake my studies in his lab and offering guidance and support throughout the work.

Prof. Dr. Hans-Beat Bürgi for supervision, motivation, advice, discussions, openness and placing confidence in me.

Prof. Dr. Karl Heinz Ernst for examining the thesis and providing constructive criticism about the work.

Dr. Thomas Weber for the XCAVATE source code and helpful discussions.

Dr. Arkadiy Simonov for MATLAB scripts and continuous help during diffuse scattering data processing.

Dr. Lukas Ahrenberg for computational support and helpful discussions.

Dr. Michal Chodkiewicz for guidance with the ZODS program and tutorials.

The Swiss National Science Foundation and the University of Zürich for financial support.

Present and former colleagues for warm discussions, coffee and lunches.

Timm Reumann for the nice company, chats and dinners.

My family for support and sympathy.

My wife Sandamali Warshamanage for her patience, awesome foods and filling me with love.

## Abstract

The single-crystal X-ray diffraction pattern from the β-phase of the industrially important Pigment Red 170 (β-P.R.170) consists of a difficult-to-disentangle mixture of Bragg diffraction superimposed by rods of diffuse scattering and satellite peaks. This extremely complicated diffraction pattern illustrates the complexity of real world crystals, whose underlying structure is far from the concept of a crystal being a regular periodic arrangement of unit cells usually presented in introductory crystallography textbooks. Such complex structures still present a big challenge to practitioners of X-ray crystallography.

Understanding of the photochemical properties of this pigment would benefit from knowledge of the specific local arrangement of molecules in the crystal structure, but such information was not available due to the disordered nature of this material. The focus of this thesis was to model the crystal structure of this material by an analysis of the total diffraction pattern.

The disorder in this material manifests itself as rods of strong diffuse scattering in the diffraction pattern. According to the mathematical description presented in the first part of the thesis, the type of disorder present in this material is stacking faults. These faults can occur during the stacking of the two dimensionally ordered molecular layers when the crystal grows. A detailed analysis of the diffraction pattern revealed that the rods of diffuse scattering pass through the Bragg reflections. Furthermore, it showed that a considerable percentage of the Bragg reflections is completely immersed in the strong diffuse streaks. As a result, the unit cell indexation and the accurate Bragg intensity estimation were extremely difficult.

An analysis of only the Bragg reflections resulted in two plausible average structures. Both structures have the same unit cell dimensions, but occur in different space groups, namely $B2_1/g$ and $P2_1/a$. The model developed in $B2_1/g$ has only one symmetry-independent disordered molecular layer in which there are two symmetry-independent molecules, both of which are disordered over two positions with an occupancy ratio 0.91:0.09 related by the vector [0, -0.158**b**, 0]. In contrast, the model developed in $P2_1/a$ has two symmetry independent molecular layers of which only one is disordered. The disordered layer is similar to the unique layer of the other model, but this time the occupancy ratio is 0.65:0.35. In addition, the two models differ in the number of molecules in the asymmetric unit, relative placement of molecular layers in the unit cell and the number of crystallographic and non-crystallographic symmetry elements in the average unit cell. The agreement *R*-factors

calculated from both models implied that the $B2_1/g$ model is the better description of the average structure.

The basic structural unit in both models is the same. It possesses the layer group symmetry $p\ 1\ 2_1/c\ 1$. The geometries of all adjacent layer pairs in both models are equivalent. According to Order-Disorder theory, this implies that the two models belong to the same polytypic family, but they differ in their layer stacking sequences.

The last part of the work presents the initial attempts taken to estimate the layer stacking sequence in the real crystal using model crystals. Two model crystals were constructed in the computer with the aid of a random number generator using the atomic coordinates and site occupancies obtained from the two average structures. The correlations between the interacting layers were introduced and the total interaction energy of each crystal was minimized according to the Monte Carlo (MC) method. The MC minimized crystals were then used to calculate total scattering intensities.

Both disordered model crystals constructed and tested in this work produced broad diffuse scattering features superimposed with some fine structure. So far, the match with the experimental data is poor. It is not yet known whether the observed fine structure in each calculated pattern is due to some underlying periodicity of the molecular layers in the model crystal, or is just a consequence of the statistical noise in the MC simulations. Resolution of this problem will require future additional time-consuming calculations.

## Zusammensfassung

Das Einkristall-Röntgenstreumuster der β-Phase des industriell wichtigen Pigment- Rots 170 (β-P.R.170) besteht aus einer schwer zu trennenden Mischung von Bragg-Brechungen überlagert von Säulen diffuser Streuung und Satellitensignalen. Dieses äusserst komplizierte Brechungsmuster illustriert die Komplexität von realen Kristallen, deren zugrunde liegende Struktur weit entfernt ist von der Vorstellung eines Kristalls als regelmässige, periodische Anordnung von Elementarzellen, wie sie gewöhnlich in einfachen Büchern zur Kristallografie gezeigt wird. Solch komplexe Strukturen sind nach wie vor eine grosse Herausforderung für praktizierende Kristallografen.

Die Kenntnis der genauen räumlichen Anordnung der Moleküle in der Kristallstruktur würde zum Verständnis der fotochemischen Eigenschaften dieses Pigments beitragen. Diese aber war wegen der ungeordneten Struktur des Materials nicht verfügbar. Das Ziel dieser Arbeit ist, die Kristallstruktur dieses Materials durch eine Analyse des gesamten Brechungsmusters zu modellieren.

Die Unordnung im Material zeigt sich als Steifen starker diffuser Streuung im Brechungsmuster. Nach der mathematischen Beschreibung im ersten Teil dieser Arbeit ist die Art der Unordnung ein Stapelfehler. Solche Fehler können bei der Stapelung der zweidimensionalen geordneten molekularen Schichten während des Kristallwachstums auftreten. Eine detaillierte Analyse der Brechungsmuster zeigt, dass die Säulen der diffusen Streuung durch die Bragg-Reflektionen verlaufen. Weiterhin zeigte sich, dass ein beachtlicher Anteil der Bragg-Reflektionen vollständig von der diffusen Streuung verdeckt wird. Das erschwerte die Indexierung der Elementarzelle und Abschätzung der Bragg-Intensitäten wesentlich.

Eine Analyse der Bragg-Reflexe allein ergab zwei plausible Durchschnittsstrukturen. Beide Strukturen haben die gleichen Dimensionen in ihren Elementarzellen, gehören aber zu verschiedenen Raumgruppen, nämlich $B2_1/g$ und $P2_1/a$. Das in $B2_1/g$ entwickelte Model besitzt nur eine symmetrieunabhängige, ungeordnete molekulare Schicht, in welcher es zwei symmetrieunabhängige Moleküle gibt, von denen beide über zwei Positionen ungeordnet sind mit einem Besetzungsverhältnis von 0,91:0,09, gegeneinander um den Vektor [0; -0,158**b**; 0] verschoben. Im Gegensatz dazu hat das in $P2_1/a$ entwickelte Model zwei symmetrieunabhängige molekulare Schichten von denen nur eine ungeordnet ist. Diese

ungeordnete Schicht ist ähnlich zu der symmetrie-eindeutigen Schicht des anderen Models, aber weist ein Besetzungsverhältnis von 0,65:0,35 auf. Zusätzlich unterscheiden sich die beiden Modelle in der Anzahl der Moleküle in der asymmetrischen Einheit, in der relativen Platzierung der molekularen Schichten in der Elementarzelle und in der Anzahl der kristallografischen und nicht-kristallografischen Symmetrieelemente in der Durchschnittszelle. Da das $B2_1/g$-Modell den tieferen *R*-Faktor aufweist, ist es wahrscheinlich näher an der tatsächlichen Durchschnittsstruktur. Nach den für beiden Modelle berechneten R-Faktoren der Uebereinstimmung ist das $B2_1/g$-Modell die bessere Beschreibung der durchschnittlichen Struktur.

Die strukturelle Grundeinheit in beiden Modellen ist die gleiche. Sie besitzt die Schichtgruppensymmetrie $p\ 1\ 2_1/c\ 1$. Alle aneinander liegenden Schichtenpaare in beiden Modellen sind gleichwertig. Nach der Theorie der geordneten und ungeordneten Strukturen von Schichten gehören beide Modelle zur gleichen polytypischen Familie, unterscheiden sich aber in der Stapelungsreihenfolge ihrer Schichten.

Der letzte Teil der Arbeit präsentiert die ersten Versuche, mit Hilfe von Modellkristallen die Stapelungsreihenfolge der Schichten im wirklichen Kristall abzuschätzen. Zwei Modellkristalle wurden im Computer mit Hilfe eines Zufallszahlengenerators aus den Atomkoordinaten und Stellenbesetzungen der Durchschnittsstrukturen konstruiert. Korrelationen zwischen den wechselwirkenden Schichten wurden eingeführt und die gesamte Wechselwirkungsenergie jedes Kristalls wurde nach der Monte-Carlo-Methode minimiert. Die so optimierten Modellkristalle wurden dann benutzt, um die gesamten Streuungsintensitäten zu berechnen.

Beide konstruierten und getesteten ungeordneten Modellkristalle in dieser Arbeit ergaben breite, diffuse, mit einigen Feinstrukturen überlagerte Streuungsmerkmale. Ihre Uebereinstimmung mit den experimentellen Daten ist schlecht. Es ist noch nicht bekannt, ob die Feinstrukturen in jedem berechneten Muster wegen einer zugrunde liegenden Periodizität der molekularen Schichten im Modellkristall auftreten oder nur eine Folge des statistischen Rauschens der MC-Simulation sind. Die Klärung dieses Problems wird zusätzliche zeitaufwendige Berechnungen erfordern.

# Table of Contents

**Acknowledgements** iii

**Abstract** v

**Zusammensfassung** vii

**Table of contents** ix

**Chapter 1: Introduction**

1.1 Motivation of the thesis 1

1.2 Complexity of crystals 3

1.3 Probes for local crystallography 5

1.3.1 Monte Carlo (MC) simulation technique 6

1.3.2 Atomic Pair Distribution Function (PDF) technique 8

1.4 The structure of the thesis 11

1.5 Bibliography 12

**Chapter 2: Mathematical and symmetry aspects of crystals**

2.1 Disorder in crystals 15

2.1.1 Different types of disorder present in crystals 21

2.1.1.1 Static disorder 21

2.1.1.1.1 Substitutional disorder 21

2.1.1.1.2 Displacement disorder 27

2.1.1.1.2.1 Stacking faults 32

2.1.1.2 Dynamic disorder 34

2.1.1.3 Magnetic disorder 35

2.2 Polytypism in layered structures 36

2.2.1 Order-Disorder (OD) theory of polytypes 37

2.2.2 Stacking ambiguities in close-packed structures and NFZ relationship 40

2.2.3 MDO polytypes 42

2.2.4 The groupoid symbol 44

2.2.5 Diffraction features of OD structures 45

2.2.6 Categories of OD structures 48

2.2.6.1 OD structures of equivalent layers 48

2.3 Bibliography 50

**Chapter 3: Diffraction pattern of a crystal of the β-phase of Pigment Red 170**

3.1 Pigment Red 170 53
3.1.1 Crystallization of the β-phase of Pigment Red 170 55
3.1.2 X-ray data collection 55
3.2 Diffraction pattern 56
3.2.1 Coarse features 56
3.2.2 Fine features 57
3.3 Bibliography 60

**Chapter 4: The average structure of β-Pigment Red 170**

4.1 Introduction to the average structure of β-Pigment Red 170 61
4.1.1 Indexing and unit cell determination 61
4.1.2 Extraction of the Bragg intensities 63
4.1.3 Space group determination 64
4.1.4 Attempts at structure solution and refinement 65
4.2 Description of the average structure 68
4.2.1 Model 1 69
4.2.2 Model 2 70
4.2.3 Similarities and differences between model 1 and model 2 72
4.2.3.1 Similarities and differences in direct space, OD analysis 72
4.2.3.2 Similarities and differences in reciprocal space 76
4.3 Subgroup analysis 79
4.4 Summary and Conclusions 80
4.5 Bibliography 82

**Chapter 5: Beyond the average structure of β-P.R.170**

5.1 Introduction to the local structure of β-P.R.170 85
5.2 Experimental data for the local structure modeling 86
5.2.1 Measurement of diffuse scattering 86
5.2.2 Preparation of diffuse data for modeling 91
5.3 Construction of the model crystal 94
5.3.1 Disentanglement of the average structure and defining chemical units 94
5.3.2 Model crystal building and energy minimization 97
5.4 Intensity calculation and qualitative analysis of models 105
5.5 Summary and conclusions 116

5.6 Bibliography 117

**Chapter 6: Conclusions and Outlook** 119

**Appendix: Crystallographic Information Files (CIF)** 123

for the average structure models 1 and 2 (only in electronic version). They are also available from the International Union of Crystallography electronic archives *via* journals.iucr.org (search keyword: og5065).

# Introduction

## 1.1 Motivation of the thesis

Many materials with useful properties have complex structures due to weak or strong disorder. For example, modern electronic materials with remarkable high-temperature superconductivity properties, colossal magnetoresistivity (CMR) or high dielectric response have atomistically complex structures (disordered) which are critically important for their performance (Egami & Billinge, 2003). All these properties are a result of competition of internal forces due to the disorder in the material. CMR oxides such as manganites [$(R_{1-x}A_x)_{n+1}Mn_nO_{3n+1}$ where R= La, Pr, Nd; A= Sr, Ba, Ca, Pb] for instance are located at the metal-to-insulator (MI) transition in the phase diagram of temperature versus concentration ($x$) of R. In these materials, the localized and delocalized charge carriers are balanced at the MI transition. By the application of an external magnetic field, this balance can be greatly perturbed thereby changing the conduction properties of the material (Egami & Billinge, 2003).

Composite metals (alloys) can be given as another example of disordered materials. They are of great technological importance as their physical properties can be tailored as needed by mixing the constituents in different proportions. They can be found in various applications in many industries, such as aerospace, sporting goods, automotive, or even home appliances. Porous materials are related to composites, but they contain voids as one of the constituents. Porous materials play increasingly important roles in various applications, such as energy conversion and storage, environmentally friendly catalysis, in various sensors, tissue engineering, DNA sequencing, drug delivery, medical diagnosis, cell-makers, and photonics (Zhao, 2006). They can be of an inorganic, organic or inorganic-organic hybrid nature and are of scientific and technological importance because of their ability to interact with atoms, ions or molecules to load or capture liquid and gas molecules and solid particles. They have become highly attractive in frontier research because of their tunable pore size and pore wall surface (Zhao, 2006). The emergence of new applications will require even more control over the porous properties of these structures.

It has very recently been discovered that disordered materials hold promises for better batteries (MIT News, 2014). Prior to this, it was generally accepted that lithium battery cathodes should be made of an ordered crystalline material or sometimes of layered structure. Any slight deviation from perfect order was believed to decrease the efficiency of the battery and thus disordered materials were generally ignored. The recent discovery showed that certain kinds of disorder can provide a significant boost in the cathode performance, thereby greatly increasing the battery's overall performance. It is apparent that this discovery will open up a new era for lithium ion battery technology.

Some disordered materials, such as the family of lanthanum halides, have the capability of light up-conversion. This refers to the process in which the emitting radiation has more energy than the incident radiation (Auzel, 2004). The famous anti-Stokes Raman emission can be given as an important example. In this process, a vibrationally excited state of an electronic ground state acts as the initial state. The absorption of a photon brings the particle to its excited state which then relaxes back to the electronic as well as vibrational ground state by emitting a photon with a somewhat higher energy. This phenomenon has been used in the anti-Stokes Raman laser technology (White & Henderson, 1981). In addition, other types of light up-conversion can be found in the book "*Luminescence from theory to applications*" by C. Ronda (Ronda, 2007). The property of light up-conversion in disordered materials is widely used in modern laser technology as well as in the smart display technology.

Liu *et al*. very recently showed that imperfections in certain types of crystals enable new functionalities, for example random lasers. In these devices, the lasing relies on random multiple scattering (Liu *et al*., 2014). As Liu explains, when the light is sent to an imperfect crystal made of gallium arsenide, it hits on many irregular holes and starts reflecting in random directions. The light is spontaneously captured in the nanostructure due to the frequent random reflections. This process allows the light to be amplified, resulting in surprisingly good conditions for creating highly efficient and compact lasers.

Given the above overview, it is obvious that disordered materials find applications everywhere. Furthermore, it may be expected that there is great potential for many more new applications. Despite their importance, the structural understanding of disordered materials is still minimal. According to this author's point of view, there are several reasons for this. Crystal structure analysis known as "Crystallography" is the main tool for obtaining information about the three dimensional arrangement of atoms and molecules in the solid

state. Although tools and techniques for routine crystallography; which deals with only ordered materials, are readily available, structure elucidation of disordered crystalline materials requires very specialized techniques, which are far from routine crystallography. Only very few techniques and tools are available today. The second reason is that most of the specialized techniques currently available require a considerable amount of computing power in order to obtain reasonable results. The third reason lies with a lack of motivated personnel who want to engage in this kind of elaborate study. However, given the potential applications of these materials, an attempt at structure elucidation is certainly a must. The motivation of this thesis falls along these lines.

The β-phase of Pigment Red 170 (β-P.R.170) is an important organic pigment used in industry for coloration of plastics, but is subject to fading upon prolonged exposure to sunlight (Schmidt *et al*., 2006). In order to modify and obtain pigments with more photochemical stability, knowledge of the crystal structure is important. X-ray diffraction pattern from a crystal is clearly evidence for the one dimensional disorder of this material. The focus of the work presented in this thesis is to establish the crystal structure of this material at the local level. It is believed that the structural understanding coming from this thesis will be useful for further development in fundamental structural research and also in the development of the pigment industry.

## 1.2 Complexity of crystals

Crystals are often ideally considered as objects that display perfect lattice periodicity in all three dimensions. This consideration has been admired in early scientific developments. For example Max von Laue in 1912 demonstrated the wave-like properties of X-rays by using a copper sulfate crystal (Schmahl & Steurer, 2012). At the time of his experiment, it was believed that the crystals were highly organized arrangements of their constituent entities and that they would thus act as diffraction gratings. His discovery indirectly proved the periodic arrangement of $CuSO_4$ moieties in a crystal. Following von Laue's discovery, William Lawrence Bragg put forward the famous Bragg's Law which shows that sharp discrete diffraction intensities arise from periodicity in the structure (Egami & Billinge, 2003). William Lawrence Bragg with his father Hendry William Bragg determined the structures of many simple compounds using the Bragg's Law (and a lot of intuition). This law is at the heart of all conventional crystallographic methods and tools even today. Even though Bragg's Law is so powerful that it can reduce the number of atomic coordinates of a typical crystal

from 3N x $10^{18}$ to 3N (N being the number of unit cells in the crystal) or can determine the unit cell length up to an accuracy of $10^{-4}$ Å, what's not certain is the appropriateness of the *a priori* assumption they made; the perfect periodicity!

The third law of thermodynamics states that the entropy of a perfect crystal is exactly equal to zero at absolute zero. Again, perfect periodicity is appreciated. Entropy is related to the number of possible microstates and is given by equation 1.

$$S_T = k \ln W_T \qquad (1.1)$$

where $W_T$ is the number of possible microstates at $T$ (K) and $k$ is the Boltzmann constant.

$S$ is zero at absolute zero for a perfect crystalline material, as it possesses only one microstate. Note that $W_T$ depends on the absolute temperature according to the Boltzmann distribution. This equation also shows that any departure from the perfection (i.e. any increase of the randomness) can result in non-zero entropy at absolute zero and is called the residual entropy of the system (Takada *et al*, 2013). Any residual entropy of a crystalline material may indicate some kind of disorder of that material. For example, a disorder situation at absolute zero of temperature is probable if a compound has a degenerate ground state. According to this viewpoint, the residual entropy may be useful for understanding and probably quantifying a material's disorder in the first place.

Even perfect crystals are not always perfectly periodic because of the thermal vibrations even at absolute zero temperature (Billinge & Thorpe, 2002). Any deviation from perfection introduces complexity in the structure by breaking down the crystal symmetry. Two main sources of complexity in crystals can be identified. The first is crystal twinning. In this case a crystal does not grow as a single domain, but as several domains related to each other by some symmetry operation. There may be several reasons for crystal twinning. Most of them are explained with regard to their energy perspectives in the article "*The genesis of twin crystals*" by M.J. Burger (Burger, 1945). The second source of complexity is disorder in crystals. This refers to the situation of loss of crystal symmetry due to one or several reasons. Depending on how the disorder occurs in crystals, it may take several forms such as thermal, orientational, occupational or positional, etc. Also it is possible that a material can exhibit more than one form of disorder simultaneously. A detailed description of different types of disorder is given in chapter 2.

For many routine crystallographic analyses, the complexity due to deviations from perfect periodicity is ignored and the crystal symmetry is restored by imposing the Debye-Waller approximation on the atomic vibrations (Egami & Billinge, 2003). The Debye-Waller approximation is applicable only when the lattice vibrations are harmonic. However, in many complex materials, these vibrations are anharmonic and cannot be described by a Gaussian type function. Therefore the applicability of the Debye-Waller approximation often fails. In such situations, the local viewpoint of the structure is more appropriate than the global viewpoint. Therefore, one needs specific approaches for determining the local crystal structure; something more than just Bragg's Law. Also it is important to understand that what is being given by this kind of approach is probabilistic rather than deterministic.

In general, in order to fully describe the structure of a complex material, two distinct viewpoints are necessary. The global picture of the material is first presented. This picture is based on the analysis of the intensities and positions of Bragg reflections only. The resulting average structure reveals only the long range order of the crystal. In this view, the interactions are averaged over the crystal space and the time of experiment. However, the real interactions occur at local levels. Considering only the global picture masks important local physics of the material. Therefore, a local view of the material is also a must. Deviations from perfect periodicity, in other words from the average structure, manifest themselves as diffuse scattering (DS) in the diffraction pattern. DS contains information about two-body interactions in the crystal (Proffen, 2000). Thus the interpretation of DS can reveal the local structure of the material. The most widely used techniques used in this context are presented in the following section.

## 1.3 Probes for local crystallography

Complete characterization of a material will require a structural as well as a functional description. The purpose of a structural study is to understand the functionalities at the atomic level. Macroscopic properties of materials originating at the atomic level are the consequences of interactions between atoms in the local environment (Egami & Billinge, 2003). Therefore, knowledge of the local arrangement of atoms is very important. In this respect the crystal (site) symmetries are not very important as they may or may not hold (Egami & Billinge, 2003). The next two subsections will present an overview of two methods of local crystallography.

### 1.3.1 Monte Carlo (MC) simulation technique

Monte Carlo simulation techniques are used in a broad range of computational algorithms as well as many physical and mathematical problems (Leach, 2001). They are widely used in three distinct classes of problems: obtaining random draws from a probability distribution, numerical integration schemes and optimization algorithms (Leach, 2001). The use of MC methods in crystal structure analyses became feasible with recent advancements in computer technology because the method is computationally intense. Fast computers and diffuse scattering data collected on area detectors have provided excellent tools for the structure elucidation of disordered materials using diffuse scattering data via MC simulations (Proffen & Welberry, 1998; Proffen, 2000; Weber & Bürgi, 2002; Welberry & Goossens, 2008; Goossens *et al*., 2011).

In general, the determination of the crystal structure of any disordered material by the combined technique of MC simulations and diffuse scattering includes several steps (Weber & Bürgi, 2002). In the first step, a real space model for the disordered crystal is generated in the computer. The model is primarily based on the information obtained from the average structure. If any disorder is seen in the average structure, for example, mixed atom site occupations or more than one possible position for a given atom in the asymmetric unit, that information is transferred into the computer model. The resulting model is described by near-neighbor interatomic or intermolecular interactions. The total energy of the crystal is expressed according to the following equation (Proffen & Welberry, 1998).

$$E_{tot} = \sum_{i,j} \varphi\,(\sigma_i, \boldsymbol{r}_i, \ldots, \sigma_j, \boldsymbol{r}_j, \ldots) \qquad (1.2)$$

where $\varphi$ represents a function of variables at sites $i$ and $j$. $\sigma_i$ is a binary variable representing the occupancy of the site $i$ and $\boldsymbol{r}_i$ is a continuous variable representing the displacement of the site $i$ from its average position. A practical application of eq. 2 is discussed in chapter 4.

The initial model does not contain any correlation of atomic positions or occupancies between neighboring unit cells (Weber & Bürgi, 2002). In the next step, the lowest energy configuration of the model is realized via MC simulations (Metropolis *et al*., 1953). In the last step, the equilibrated model is Fourier transformed, intensities are calculated and compared with experimental data. If the fit is unsatisfactory, the near-neighbor interactions are adjusted and the process is repeated until the desired match is obtained. The latter part of the final step is often called the refinement/optimization of the model. The refinement of the model

parameters is done by least-squares (Welberry *et al*., 1998) or evolutionary algorithms (Weber & Bürgi, 2002).

Several advantages of MC simulations in the context of disordered structure modeling can be identified. The obvious advantage is that it allows one to work in physical space, which allows a physical picture of the disorder to be obtained. Another advantage is that this method offers the possibility of a systematic study of different possible causes of the diffuse scattering (Proffen & Welberry, 1998). Furthermore the emergence of new faster computers, more memory and storage have allowed one to use disordered crystal models with relatively large numbers of atoms/molecules, which in turn leads to better results. Also the post refinement process of the model parameters can be automated (Weber & Bürgi, 2002). That will also lead to fast and reliable results in the end. A detailed description of the MC method as applied to the compound studies in this thesis, i.e. the disordered β-phase of Pigment Red 170, is given in chapter 5.

McGreevy and Pusztai in 1988 first presented a variant method of direct MC called the Reverse Monte Carlo (RMC) method (McGreevy & Pusztai, 1988). This method, when applied to disorder structure modeling, the difference between observed and calculated diffuse scattering intensities is minimized as a function of the positions and occupancies of the atomic sites (Proffen & Welberry, 1998). Steps involved in this method are as follows. In the first step the scattered intensities are calculated from the starting configuration of the model crystal. Then the goodness-of-fit ( $\chi^2$ ) between the experimental and the calculated intensities is obtained as follows,

$$\chi^2 = \sum_{i=1}^{N} \frac{[I_e(\boldsymbol{Q}_i) - I_c(\boldsymbol{Q}_i)]^2}{\sigma^2}$$

where $N$ is the total number of data points $(\boldsymbol{Q}_i)$ measured. $I_e$ and $I_c$ are the experimental and the calculated intensities respectively, while $\sigma$ is a measure of the accuracy of the measurement. During the RMC process a site in the crystal is randomly selected and the variables associated with this site (occupancy, displacement) are perturbed by a random amount and the scattered intensities and the $\chi^2$ are calculated. If the change in $\chi^2$ is negative, that move is accepted. If the change in $\chi^2$ is positive, that move is also accepted with a probability of $P = \exp(-\Delta\chi^2/2)$. This process is repeated until $\chi^2$ reaches its minimum.

This method has been successfully applied to several diffuse scattering studies using powder diffraction data (Nield *et al*, 1992, 1993; Montfrooij *et al*., 1996) and also to several single crystal diffuse scattering studies (Nield *et al*., 1995; Proffen & Welberry, 1997, 1998b; Welberry *et al*., 2013).

### 1.3.2 Atomic Pair Distribution Function (PDF) technique

The scattered intensity measured during an X-ray or neutron experiment is composed of several parts (Egami & Billinge, 2003).

$$I_{total} = I_{coherent} + I_{incoherent} + I_{multiple\text{-}scattering} + I_{background} \qquad (1.3)$$

$I_{total}$ is measured as a function of the scattering angle, $2\theta$, and the wavelength of the radiation used. The observed intensity should be corrected properly for all possible secondary effects such as Lorentz and polarization, absorption and background scattering. The corrected intensity is multiplied with a normalization factor in order to express the coherent scattering cross-section in the appropriate units of intensity per atom (Egami & Billinge, 2003). The resulting normalized, corrected total scattering intensity is a continuous function of the diffraction vector **Q**, and is denoted by $S(\mathbf{Q})$. In general, $S(\mathbf{Q})$ contains sharp intensities at integer values of $|\mathbf{Q}|$ (Bragg positions), while broad diffuse intensities at non-integer values of $|\mathbf{Q}|$. In the case of isotropic scattering, for example scattering by gases, liquids, and glassy materials, the function $S(\mathbf{Q})$ will depend only on the magnitude of the scattering vector, but not on the direction because the magnitude in all directions is the same. This is also true for the case of scattering from an ensemble of finely powdered crystallites. Scattering from one crystallite is not isotropic but from an ensemble is isotropic (Egami & Billinge, 2003). For this reason, the PDF technique, as described below, has primarily been advanced as an analytical tool in the context of powder diffraction. However, the limitations of 1D-PDF are obvious. In this case, the data are averaged over all three dimensions to produce a one dimensional function. During the averaging, interatomic vectors of similar length become indistinguishable even if their spatial orientations differ significantly. Moreover, the frequency of powder PDF peaks increases with $|\boldsymbol{r}|^2$ and thus overlap problems quickly become unwieldy if the interatomic vectors of interest are getting long (Weber & Simonov, 2012). In order to avoid these issues the PDF technique in higher dimensions has recently been developed (Weber & Simonov, 2012). Despite the above-mentioned shortcomings, for the purpose of this discussion 1D-PDF is used because of its didactic simplicity. Towards the end of this section, a short account of the 3D-PDF technique will be presented.

The scattering data can be analyzed either in reciprocal space or in real space. In reciprocal space, this is done by fitting models to the total scattering structure function, *S*(Q). The analysis is considerably facilitated if the data are first Fourier transformed to real-space to obtain the atomic pair distribution function and then carrying out the analysis in real space. The reduced pair distribution function, *G*(*r*) is obtained from *S*(Q) via a sine Fourier transform according to following equation.

$$G(r) = \frac{2}{\pi}\int_{Q_{min}}^{Q_{max}} Q[S(Q) - 1]\sin(Qr)dQ \qquad (1.4)$$

The important observation is that *G*(*r*) has peaks with high probability at the interatomic distances of pairs of atoms. This function can be characterized as follows. It goes to zero as the limit of $r = 0$. It oscillates around zero and asymptotically approaches zero at large *r* values. There are several advantages of *G*(*r*) over other related forms of PDFs which can be found in detail in the book of "*Underneath the Bragg peaks: Structural analysis of complex materials*" by Egami and Billinge (Egami & Billinge, 2003). *G*(*r*) is obtained directly by the Fourier transform of *S*(*Q*) and is thus the most closely related to the experimental data. Because of this, the random uncertainties in the data are constant in *r*. This means that the fluctuations in the difference between the measured and the calculated *G*(*r*) have the same significance in all *r* values. For example if the fluctuations in the difference plot decrease with increasing *r*, that implies that the model is getting better at long *r* values. Another advantage is that the amplitudes of oscillations of *G*(*r*) provide direct information on the measure of the structural coherence of the material. In the case of perfect crystals, these oscillations extend to infinity with constant peak amplitude. In real crystals, the amplitudes of these oscillations fall off gradually as a result of the finite Q-resolution in the measurement. Data to a large range of *r* is obtainable with a high Q-resolution. However in the case of materials with some disorder, the amplitudes of these signals fall off faster than expected for Q-resolution and this information may be taken as a useful measure of structural coherence of the material.

The atomic pair distribution function, *g*(*r*), can be obtained directly from *G*(*r*) according to the following equation.

$$G(r) = 4\pi\rho_0 r(g(r) - 1) \qquad (1.5)$$

where $\rho_0$ is the average number density of the material. The *g*(*r*) is normalized so that it goes to unity when the distance (*r*) approaches infinity. It has the property that when *r* is shorter than the closest distance of atoms, *g*(*r*) is zero.

For the purpose of real-space modeling, the PDF from the model is first calculated according to the following equation.

$$\rho(r) = \rho_0 g(r) = \frac{1}{4\pi N r^2} \sum_\nu \sum_\mu \delta(r - r_{\nu\mu}) \qquad (1.6)$$

where $\rho(r)$ is the atomic pair density function. *N* is the total number of atoms in the system. *v* and $\mu$ refer to two individual atoms while $r_{\nu\mu}$ is the interatomic distance between those two atoms. This function represents the distribution of interatomic distances of the material. The modeling is carried out by fitting the calculated PDF to the experimental one. The fitting is usually done via a least-squares (Proffen & Billinge, 1999) or Reverse Monte-Carlo (RMC) refinement (Nield *et al*., 1994; Toby & Egami, 1992).

Even without modeling, the experimental PDF alone reveals a wealth of information on the underlying structure. The peak positions in the PDF indicate the interatomic distances in the material with those separations. The peak height gives a measure of the probability of the occurrence of that particular interatomic distance (bond) in the solid. The peak width contains information about the thermal motion of atoms and static disorder (Egami & Billinge, 2003), with this information alone it is generally difficult to decide whether the peak broadening is due to static or dynamic effects.

Another representation of the PDF is the radial distribution function denoted as RDF or simply R(r). The R(r) and $\rho(r)$are related to each other according to the following equation,

$$R(r) = 4\pi r^2 \rho_0 g(r) \qquad (1.7)$$

The important aspect of the RDF is that it is directly related to the coordination number of a given origin atom and a given shell. In order to get his number, the function is integrated over the range of the shell as follows,

$$N_c = \int_{r_1}^{r_2} R(r) dr \qquad (1.8)$$

$N_c$ is the coordination number of the shell in question and $r_1$, $r_2$ define the lower and the upper limit of the shell respectively. In the case of samples containing several elements, these numbers are usually obtained after a full-scale structural modeling (Egami & Billinge, 2003).

So far only the one-dimensional PDF was considered. The shortcomings associated with this approach were noted at the beginning of this section and three dimensional PDF was introduced as a remedy for those issues.

With the advent of new area detectors with fast readout, high dynamic range and low background, the 3D-PDF technique seems to be becoming more widely used among the structural scientists (Weber & Simonov, 2012; Schaub *et al*., 2007). Unlike powder PDF, 3D-PDF can reveal the spatial orientation of interatomic vectors. Moreover, if the material has vectors of similar length but differing in direction; they are superimposed in the powder PDF. This may lead to great difficulties in interpreting the pattern. However, this difficulty is avoided in 3D-PDF.

Single crystal X-ray or neutron total scattering data are used in order to obtain 3D-PDFs. Since the scattering data are three-dimensional, the resulting PDFs are also three dimensional. Therefore both the length and the angular information of interatomic vectors are preserved. The analysis is carried out the same way as for powder PDFs, but this time two additional dimensions are considered.

## 1.4 The structure of the thesis

The β-phase of Pigment Red 170 is an industrially important organic pigment but subject to fading over a long exposure to sunlight. The fading occurs as a result of the cleavage of the ethoxy group from the molecular P.R.170 upon the absorption of photon energy. In the layer structure of the g-form, a small vacancy near the ethoxy group allows the cleaved radical to move away from the main molecule, thus lowering the probability of it recombining and leading to slow photochemical degradation of the pigment. Successful attempts to fill these voids about the ethoxy groups in the crystal structure of γ-P.R.170, by suitable modification of the molecule, have been performed (Schmidt *et al*., 2006).

The diffraction pattern from a freshly prepared single crystal of β-P.R.170 is heavy with rods of diffuse scattering implying that the crystal has lost its periodicity along one dimension. This thesis presents the developed models for the average structure and the attempts to model the local structure of this material.

The whole thesis consists of six chapters. The first chapter presents the motivation for studying disordered materials in general and specifically on the β-phase of Pigment Red 170.

The importance of disordered materials is presented through several examples. The methods used to probe the local structure of disordered materials are briefly discussed.

The second chapter covers the mathematical and symmetrical aspects of various types of disorder present in crystals. This chapter lays the necessary grounds for chapter 4 and 5.

The details of the diffraction pattern of the β-phase of Pigment Red 170 crystal are described in chapter 3. Unusual features are identified and interpreted where possible.

Non-trivial indexing and data integration methods used in this study makes the first part of the chapter 4. The difficulties faced during indexing and data integration are discussed and possible justifications are presented using the features of the diffraction pattern discussed in chapter 3. The second part is devoted to describing the two average models developed for this compound. Non-trivial relationships between the two average models are discussed. The next part of the chapter describes the two models as two valid superposition structures belong to the same polytypic family. The two models are compared on the basis of the layer symmetry. Lastly, the two models are compared in the reciprocal space by calculating their structure factors.

The attempts to obtain the local structure of this material are the subject of chapter 5. The first part of the chapter presents various techniques of measuring and preparing diffuse scattering data for a local structure modeling. Next the construction of model crystals using the average structure models is discussed. The last part of the chapter discusses the intensity calculation from the model crystals. The calculated intensities are compared with experimental diffraction data. Towards the end, the whole chapter is summarized. The final chapter concludes the whole study and an outlook is presented.

## 1.5 Bibliography

Auzel, F. (2004). *Chem. Rev*. **104**, 139-173.

Billinge, S. J. L. & Thorpe, M. F. (2002). Editors. *Local Structure from Diffraction*, New York: Kluwer Academic Publishers.

Burger, M. J. (1945). *American Mineralogist*, **30**, 369-482.

Chandler, D. L. (09.01.2014). "*Disordered materials hold promises for better batteries*" MIT News Office.

Egami, T. & Billinge, S. J. L. (2003). *UNDERNEATH THE BRAGG PEAKS: Structural Analysis of Complex Materials*, Pergamon Materials Series, Vol. 7, London: PERGAMON: Elsevier.

Goossens, D. J., Heerdegen, A. P. & Welberry, T. R. (2011), *Metallurgical and Materials Transactions* A, **42**, 23-31.

Leach, A. R. (2001). *Molecular Modelling: PRINCIPLES AND APPLICATIONS*, 2nd ed., Harlow: Pearson Education Limited.

Liu, J., Garcia, P. D., Ek, S., Gregersen, N., Suhr, T., Schubert, M., Mørk, J., Stobbe, S. & Lodhal, P. (2014). *Nature Nanotec*. **9**, 285-289.

McGreevy, R. L. & Pusztai, L. (1988). *Mol. Simul*. **1**, 359-367.

Metropolis, N., Rosenbluth, A.W., Rosenbluth, M. N., Teller, A. H. & Teller, E. J. (1953). *J. Chem. Phys.* **21**, 1087-1094.

Montfrooij, W., McGreevy, R. L., Hadfield, R. & Anderson, N. H. (1996). *J. Appl. Cryst*. **29**, 285-290.

Nield, V. M., Keen, D. A., Hayes, W. & McGreevy, R. L. (1992). *J. Phys. Condens. Matter*, **4**, 6703-6714.

Nield, V. M., Keen, D. A., Hayes, W. & McGreevy, R. L. (1993). *Solid State Ion*. **66**, 247-258.

Nield, V. M., Keen, D. A. & McGreevy, R.L. (1995). *Acta Cryst*. A**51**, 763-771.

Nield, V. M., McGreevy, R. L., Keen, D. A. & Hayes, W. (1994). *Physica* B, **202**, 159-166.

Proffen, Th. (2000). *Z. Kristallogr*. **215**, 1-8.

Proffen, Th., & Welberry, T. R. (1998). *Phase Transitions: A Multilingual Journal,* **67**, 373-397.

Proffen. Th. & Welberry, T. R. (1997). *Acta Cryst*. A**53**, 202-216.

Proffen. Th. & Welberry, T. R. (1998b). *J. Appl. Cryst*. **31**, 318-326

Proffen, Th. & Billinge, S. J. L. (1999). *J. Appl. Cryst*. **32**, 572-575.

Ronda, C. (2007). *Luminescence from theory to applications*, Weinheim: Wiley-VCH.

Schaub, P., Weber, T. & Steurer, W. (2007). *Philosophical Magazine*, **87**, 2781-2787.

Schmahl, W. W. & Steurer, W. (2012). *Acta Cryst*. A**68**, 1-2.

Schmidt, M. U., Hofmann, D. W. M., Buchsbaum, C. & Metz, H. J. (2006). *Angew. Chem*. **118**, 1335-1340, *Angew. Chem. Int. Ed.* 45, 1313-1317.

Takada, A., Conradt, R. & Richet, P. (2013). *J. Non-Cryst. Solids*, **360**, 13-20.

Toby, B. H. & Egami, T. (1992). Acta Cryst. A**48**, 336-346.

Weber, T. & Bürgi, H.-B. (2002). *Acta Cryst*. A**58**, 526-540.

Weber, T. & Simonov, A. (2012). *Z. Kristallogra.* **227**, 238-247.

White, J. C. & Henderson, D. (1981). *Phys. Rev.* A **25**, 1226-1229.

Welberry, T. R., Proffen, Th. & Brown, M. (1998). *Acta Cryst*. A**54**, 661-674.

Welberry, T. R. & Goossens, D. J. (2008). *Acta Cryst*. A**64**, 23-32.

Welberry, T. R., Heerdegen, A. P. & Carr, P. D. (2013). *Aperiodic Crystals*, 243-251.

Zhao, X. S. (2006). *J. Matter. Chem*. **16**, 623-625.

# Mathematical and symmetry aspects of crystals

This chapter covers the mathematical and symmetry aspects of ordered and disordered crystals. The first part of the chapter (§2.1) begins with obtaining the expressions for the structure factors and intensities in the diffraction pattern from ordered crystals. Next, the derivation of analogous expressions for disordered crystals is discussed. A substantial part of §2.1 is devoted to discussion of the mathematical descriptions of various types of disorder present in crystals. The use of those descriptions to explain the disorder present in β-P.R.170 is presented in chapter 5. The second part of the chapter (§2.2) covers the symmetry aspects of ordered and one-dimensionally disordered crystals. First the notion of polytypism is presented. It is followed by the basic elements of Order-Disorder (OD) theory. Next the derivation of the groupoid symbol for a polytypic family is discussed. Lastly the diffraction patterns from a family of polytypic structures are explained. The application of OD theory to β-P.R.170 is presented in chapter 4.

## 2.1 Disorder in crystals

A perfect crystal is made up of a 3-dimensional periodic lattice of identical unit cells each with electron density $\rho(\boldsymbol{r})$. Each unit cell in the crystal corresponds to a particular node in the lattice. For the diffraction calculations, the contribution from the $n^{th}$ unit cell located at the end of the vector $\boldsymbol{r}_n$ away from the global origin of the crystal is given by the corresponding structure factor $F_n(\boldsymbol{R})$.

$$F_n(\boldsymbol{R}) = \int_0^V \rho^n(\boldsymbol{r} + \boldsymbol{r}_n)\, exp[-2\pi i \boldsymbol{R}.(\boldsymbol{r} + \boldsymbol{r}_n)]\, dv_{\boldsymbol{r}} \qquad (2.1)$$

where $\boldsymbol{r} = x\boldsymbol{a} + y\boldsymbol{b} + z\boldsymbol{c}$; $0 \leq$ x, y, z $\leq 1$ and $\boldsymbol{a}$, $\boldsymbol{b}$, $\boldsymbol{c}$ are unit cell parameters; $\boldsymbol{r}_n = p\boldsymbol{a} + q\boldsymbol{b} + r\boldsymbol{c}$; $p$, $q$ and $r$ are integers. $\boldsymbol{R}$ is the diffraction vector and is equal to $(\boldsymbol{S} - \boldsymbol{S}_0)/\lambda$ where $\boldsymbol{S}$ and $\boldsymbol{S}_0$ are unit vectors indicating the scattered and incident waves, respectively. $\lambda$ is the wavelength of the X-ray radiation used. When $R = 0$ the product of $\rho(\boldsymbol{r})$ times a small volume element, $dv$, at $\boldsymbol{r}$ gives the number of electrons in that volume element. The total number of

electrons within the unit cell is obtained by integrating $\rho(\boldsymbol{r})dv_{\boldsymbol{r}}$ over the whole unit cell volume *V*.

An expression for the structure factor $F_n(\boldsymbol{R})$ analogous to eq. 2.1 can be obtained by partitioning the electron density of the $n^{\text{th}}$ unit cell into its constituent individual atomic densities as follows. It is assumed that the centers of the individual atoms are located at $\boldsymbol{r}_1^n$, $\boldsymbol{r}_2^n$, $\boldsymbol{r}_3^n$, …, $\boldsymbol{r}_i^n$ relative to the origin of the $n^{\text{th}}$ unit cell. The electron density of the $i^{\text{th}}$ atom in the $n^{\text{th}}$ unit cell can be written as $\rho_i^n(\boldsymbol{r}-\boldsymbol{r}_i^n)$. Therefore the total electron density $\rho(\boldsymbol{r}+\boldsymbol{r}_n)$ of the $n^{\text{th}}$ unit cell is

$$\rho^n(\boldsymbol{r}+\boldsymbol{r}_n)=\sum_i \rho_i^n(\boldsymbol{r}-\boldsymbol{r}_i^n-\boldsymbol{r}_n). \qquad (2.2)$$

Substituting eq. 2.2 in 2.1,

$$F_n(\boldsymbol{R})=\int_0^V \sum_i \rho_i^n(\boldsymbol{r}-\boldsymbol{r}_i^n)\,exp(-2\pi i\boldsymbol{R}.\boldsymbol{r})\,exp(-2\pi i\boldsymbol{R}.\boldsymbol{r}_n)\,dv_{\boldsymbol{r}}$$

$$=exp(-2\pi i\boldsymbol{R}.\boldsymbol{r}_n)\sum_i\left[\int_0^V \rho_i^n(\boldsymbol{r}-\boldsymbol{r}_i^n)exp(-2\pi i\boldsymbol{R}.\boldsymbol{r})dv_{\boldsymbol{r}}\right]$$

$$=exp(-2\pi i\boldsymbol{R}.\boldsymbol{r}_n)\sum_i\left[\int_0^V \rho_i^n(\boldsymbol{r}-\boldsymbol{r}_i^n)exp\{-2\pi i\boldsymbol{R}.(\boldsymbol{r}-\boldsymbol{r}_i^n)\}dv_{\boldsymbol{r}}\right]exp(-2\pi i\boldsymbol{R}.\boldsymbol{r}_i^n)$$

$$=exp(-2\pi i\boldsymbol{R}.\boldsymbol{r}_n)\sum_i f_i^n(\boldsymbol{R})exp(-2\pi i\boldsymbol{R}.\boldsymbol{r}_i^n) \qquad (2.3)$$

where $f_i^n(\boldsymbol{R})=\left[\int_0^V \rho_i^n(\boldsymbol{r}-\boldsymbol{r}_i^n)exp\{-2\pi i\boldsymbol{R}.(\boldsymbol{r}-\boldsymbol{r}_i^n)\}dv_{\boldsymbol{r}}\right]$.

$f_i^n(\boldsymbol{R})$ is the atomic form factor of $i^{\text{th}}$ atom in the $n^{\text{th}}$ unit cell. It is the Fourier transform of the electron density distribution of that atom and is independent of $\boldsymbol{r}_i^n$ and $\boldsymbol{r}_n$. It can be explicitly written as $f_i(\boldsymbol{R})=\int \rho_i(\boldsymbol{r})exp(-2\pi i\boldsymbol{R}.\boldsymbol{r})$. Note that when $R = 0$, the atomic form factor takes its maximum value and is equal to the atomic number of that atom.

In the case of perfect crystals $\rho_i^n(\boldsymbol{r})=\rho_i(\boldsymbol{r})$; $f_i^n(\boldsymbol{R})=f_i(\boldsymbol{R})$ and $\boldsymbol{r}_i^n=\boldsymbol{r}_i$. The structure factor for the $n^{\text{th}}$ unit cell is the same for all other unit cells. The structure factor of the superposition wave $F_N(\boldsymbol{R})$ discussing the scattering from the entire crystal with *N* unit cells is

$$F_N(\boldsymbol{R})=\sum_n F_n(\boldsymbol{R})$$

$$=\sum_n exp(-2\pi i\boldsymbol{R}.\boldsymbol{r}_n)\sum_i f_i^n(\boldsymbol{R})\,exp(-2\pi i\boldsymbol{R}.\boldsymbol{r}_i^n).$$

Due to the lattice function [$L(\boldsymbol{R}) = \sum exp(-2\pi i \boldsymbol{R}.\boldsymbol{r}_n)$], $F_N(\boldsymbol{R})$ is equal to zero except for $\boldsymbol{R} = h\mathbf{a}^* + k\mathbf{b}^* + l\mathbf{c}^*$ where $h$, $k$ and $l$ are integers and $\mathbf{a}^*$, $\mathbf{b}^*$ and $\mathbf{c}^*$ are the reciprocal lattice vectors.

Diffraction experiments are generally measuring only the intensities of the diffracted waves, not the diffracted amplitudes. The intensity of the diffracted wave $I_N(\boldsymbol{R})$ is the product of the complex amplitude $F_N(\boldsymbol{R})$ and its complex conjugate $F_N^*(\boldsymbol{R})$. Thus

$$I_N(\boldsymbol{R}) = F_N(\boldsymbol{R})F_N^*(\boldsymbol{R}). \qquad (2.4)$$

Given $\rho_i^n(\boldsymbol{r}) = \rho_i(\boldsymbol{r})$; $f_i^n(\boldsymbol{R}) = f_i(\boldsymbol{R})$ and $\boldsymbol{r}_i^n = \boldsymbol{r}_i$ for perfect crystals, eq. 2.4 can be written as:

$$I_N(\boldsymbol{R}) = L(\boldsymbol{R}) \int_0^V \rho(\boldsymbol{r}) exp(-2\pi i \boldsymbol{R}.\boldsymbol{r})\, dv_{\boldsymbol{r}}\, L^*(\boldsymbol{R}) \int_0^V \rho(\boldsymbol{r}')\, exp(2\pi i \boldsymbol{R}.\boldsymbol{r}')\, dv_{\boldsymbol{r}'}$$

$$= L(\boldsymbol{R})L^*(\boldsymbol{R}) \iint_0^V \rho(\boldsymbol{r})\rho(\boldsymbol{r}')\, exp(-2\pi i \boldsymbol{R}.\boldsymbol{r})\, exp(2\pi i \boldsymbol{R}.\boldsymbol{r}')\, dv_{\boldsymbol{r}} dv_{\boldsymbol{r}'}$$

$$= L(\boldsymbol{R})L^*(\boldsymbol{R}) \iint_0^V \rho(\boldsymbol{r})\rho(\boldsymbol{r}')\, exp(-2\pi i \boldsymbol{R}.(\boldsymbol{r} - \boldsymbol{r}'))\, dv_{\boldsymbol{r}} dv_{\boldsymbol{r}'}$$

Let $\boldsymbol{r}' = \boldsymbol{r} + \boldsymbol{x}$, then

$$= L(\boldsymbol{R})L^*(\boldsymbol{R}) \iint_0^V \rho(\boldsymbol{r})\rho(\boldsymbol{r} + \boldsymbol{x})\, exp(2\pi i \boldsymbol{R}.\boldsymbol{x}))\, dv_{\boldsymbol{r}} dv_{\boldsymbol{x}}$$

$$= L(\boldsymbol{R})L^*(\boldsymbol{R}) \int \left\{ \int_0^V \rho(\boldsymbol{r})\rho(\boldsymbol{r} + \boldsymbol{x}) dv_{\boldsymbol{r}} \right\} exp(2\pi i \boldsymbol{R}.\boldsymbol{x}) dv_{\boldsymbol{x}}$$

The self-convolution $\int_0^V \rho(\boldsymbol{r})\rho(\boldsymbol{r} + \boldsymbol{x}) dv_{\boldsymbol{r}}$ is the Patterson function $P(\boldsymbol{x})$ (Dunitz, 1995). It is defined in real space and has the units of electrons squared per unit cell. It is closely related to the electron density. The Patterson function does not solve the phase problem but under special conditions (see Dunitz, 1995) it helps to solve this problem. Thus

$$I_N(\boldsymbol{R}) = L(\boldsymbol{R})L^*(\boldsymbol{R}) \int_0^V P(\boldsymbol{x})\, exp(2\pi i \boldsymbol{R}.\boldsymbol{x})\, dv_{\boldsymbol{x}}. \qquad (2.5)$$

Eq. 2.5 gives the intensity of the diffracted wave as a Fourier transform of the Patterson function. The inverse Fourier transform yields the Patterson function from measured intensities.

Unlike in perfect crystals, the type and the positions of atoms in imperfect crystals may be different from one unit cell to another. As a result, the electron density is no longer periodic.

In order to derive expressions for the structure factor and diffraction intensities from imperfect crystals, several assumptions were made here and are listed below.

1. The disordered crystal has *N* unit cells.
2. Each unit cell contains only one atom.
3. The atom in any one unit cell can be of a different element depending on the cell or it can be of the same type but displaced from its average position or both.
4. The electron density of each unit cell is represented by $\rho^n(\boldsymbol{r})$ where *n* enumerates the unit cells.

Let the types of atoms in the crystal be A, B, C, …, I, … and their occupancy ratio be $c_{\mathrm{A}}$, $c_{\mathrm{B}}$, $c_{\mathrm{C}}$, …, $c_{\mathrm{I}}$,… respectively. Let the electron densities of A, B, C, …, I, … be $\rho_A(\boldsymbol{r})$, $\rho_B(\boldsymbol{r})$, $\rho_C(\boldsymbol{r})$, …,$\rho_I(\boldsymbol{r})$,… and the distribution functions of A, B, C, …, I, … be $\varphi_{\mathrm{A}}(\boldsymbol{r}_A)$, $\varphi_{\mathrm{B}}(\boldsymbol{r}_B)$, $\varphi_{\mathrm{C}}(\boldsymbol{r}_C)$, …,$\varphi_{\mathrm{I}}(\boldsymbol{r}_I)$,… respectively.

Let $a = \{A, B, C, \dots, I, \dots\}$, thus $\boldsymbol{r}_a = \{\boldsymbol{r}_A, \boldsymbol{r}_B, \boldsymbol{r}_C, \dots, \boldsymbol{r}_I, \dots\}$; $c_a = \{c_A, c_B, c_C, \dots, c_I, \dots\}$; $\varphi_a(\boldsymbol{r}) = \{\varphi_A(\boldsymbol{r}), \varphi_B(\boldsymbol{r}), \varphi_C(\boldsymbol{r}), \dots, \varphi_I(\boldsymbol{r})\}$ and $\rho_a(\boldsymbol{r}) = \{\rho_A(\boldsymbol{r}), \rho_B(\boldsymbol{r}), \rho_C(\boldsymbol{r}), \dots, \rho_I(\boldsymbol{r}), \dots\}$.

Also,

$$\varphi_I(\boldsymbol{r}) = \sum_n \delta(\boldsymbol{r} - \boldsymbol{r}_I^n - \boldsymbol{r}_n) S_I^n$$

where $S_I^n = 1$ when $\rho_I^n = \rho_I$; $S_I^n = 0$ when $\rho_I^n = 0$.

The average position of $\rho_I(\boldsymbol{r})$ relative to $\boldsymbol{r}_n$ is

$$\bar{\boldsymbol{r}}_I = \int \boldsymbol{r}\varphi_I(\boldsymbol{r} - \boldsymbol{r}_I)d\boldsymbol{r}.$$

The electron density of each unit cell can be expressed as the sum of the average electron density $\overline{\rho^n}(\boldsymbol{r})$ averaged over the positions and the types of atoms in the crystal, and the deviation electron density $\Delta\rho_I^n(\boldsymbol{r})$ between the real density of the $n^{\text{th}}$ unit cell and the average density.

The average electron density can be expressed as

$$\overline{\rho^n}(\boldsymbol{r}) = c_A\rho_A(\boldsymbol{r}) \otimes \varphi_{\mathrm{A}}(\boldsymbol{r} - \bar{\boldsymbol{r}}_A - \boldsymbol{r}_n) + c_B\rho_B(\boldsymbol{r}) \otimes \varphi_{\mathrm{B}}(\boldsymbol{r} - \bar{\boldsymbol{r}}_B - \boldsymbol{r}_n)$$

$$+ c_C\rho_C(\boldsymbol{r}) \otimes \varphi_C(\boldsymbol{r} - \bar{\boldsymbol{r}}_C - \boldsymbol{r}_n) + \cdots$$

This can be written as

$$\overline{\rho^n}(\boldsymbol{r}) = \sum_I c_I \rho_I(\boldsymbol{r}) \otimes \varphi_I(\boldsymbol{r} - \bar{\boldsymbol{r}}_I - \boldsymbol{r}_n) \qquad (2.6)$$

where $\boldsymbol{r}_n$ is the lattice vector.

The average electron density in any unit cell is the same. Thus $\overline{\rho^n}(\boldsymbol{r}) = \bar{\rho}(\boldsymbol{r})$.

The Fourier transform of the average electron density corresponds to the average structure factor and is

$$\bar{F}_n(\boldsymbol{R}) = \sum_I c_I f_I(\boldsymbol{R}) \Phi_I(\boldsymbol{R}) exp(-2\pi i R.\bar{\boldsymbol{r}}_I) exp(-2\pi i R.\boldsymbol{r}_n) \qquad (2.7)$$

where $f_I(\boldsymbol{R})$ and $\Phi_I(\boldsymbol{R})$ are the Fourier transformed quantities of $\rho_I(\boldsymbol{r})$ and $\varphi_I(\boldsymbol{r})$ respectively.

The electron density of the $n^{\text{th}}$ unit cell is $\rho_I^n(\boldsymbol{r} - \boldsymbol{r}_I)$. Therefore the difference electron density of the $n^{\text{th}}$ unit cell can be written as

$$\Delta\rho_I^n(\boldsymbol{r}) = \rho_I^n(\boldsymbol{r} - \boldsymbol{r}_I) - \bar{\rho}(\boldsymbol{r}).$$

The Fourier transform of $\Delta\rho_I^n(\boldsymbol{r})$ is

$$\Delta F_n(\boldsymbol{R}) = f_I^n(\boldsymbol{R}) exp(-2\pi i \boldsymbol{R}.\boldsymbol{r}_I) exp(-2\pi i \boldsymbol{R}.\boldsymbol{r}_n) - \bar{F}(\boldsymbol{R}). \qquad (2.8)$$

Let $F_n(\boldsymbol{R}) = f_I^n(\boldsymbol{R}) exp(-2\pi i \boldsymbol{R}.\boldsymbol{r}_I) exp(-2\pi i \boldsymbol{R}.\boldsymbol{r}_n)$, then eq. 2.8 can be rewritten as

$$F_n(\boldsymbol{R}) = \bar{F}_n(\boldsymbol{R}) + \Delta F_n(\boldsymbol{R}). \qquad (2.9)$$

The structure factor of the superposition wave is

$$F_N(\boldsymbol{R}) = \sum_n F_n(\boldsymbol{R})$$

$$= \sum_n [\bar{F}_n(\boldsymbol{R}) + \Delta F_n(\boldsymbol{R})]$$

Let $\bar{F}_N(\boldsymbol{R}) = \sum_n \bar{F}_n(\boldsymbol{R})$ and $\Delta F_N(\boldsymbol{R}) = \sum_n \Delta F_n(\boldsymbol{R})$, then

$$F_N(\boldsymbol{R}) = \bar{F}_N(\boldsymbol{R}) + \Delta F_N(\boldsymbol{R}). \qquad (2.10)$$

According to eq. 2.4, the intensity of the superposition wave is

$$I_N(\boldsymbol{R}) = [\bar{F}_N(\boldsymbol{R}) + \Delta F_N(\boldsymbol{R})][\bar{F}_N(\boldsymbol{R}) + \Delta F_N(\boldsymbol{R})]^*$$

$$= \bar{F}_N(\boldsymbol{R})\bar{F}_N^*(\boldsymbol{R}) + \bar{F}_N(\boldsymbol{R})\Delta F_N^*(\boldsymbol{R}) + \bar{F}_N^*(\boldsymbol{R})\Delta F_N(\boldsymbol{R}) + \Delta F_N(\boldsymbol{R})\Delta F_N^*(\boldsymbol{R}). \qquad (2.11)$$

The second and the third terms in eq. 2.11 are zero, as shown by Fultz & Howe (2013). Their explanation is given below.

Consider the second term in eq. 2.11,

$\bar{F}_N(\boldsymbol{R})\Delta F_N^*(\boldsymbol{R})$

The Fourier transformation of the above term is

$\int \bar{F}_N(\boldsymbol{R}) exp(2\pi i \boldsymbol{R}.\boldsymbol{r}) d\boldsymbol{r} \otimes \int \Delta F_N^*(\boldsymbol{R}) exp(2\pi i \boldsymbol{R}.\boldsymbol{r}) d\boldsymbol{r}$

$= \bar{\rho}_N(\boldsymbol{r}) \otimes \Delta\rho_N(-\boldsymbol{r})$

$= \{\overline{\rho^n}(\boldsymbol{r}) \otimes \sum_n \delta[\boldsymbol{r} - (\bar{\boldsymbol{r}}_I + \boldsymbol{r}_n)]\} \otimes \Delta\rho_N(-\boldsymbol{r}).$

Let $\boldsymbol{A}_n = \bar{\boldsymbol{r}}_a + \boldsymbol{r}_n$, thus

$= \{\overline{\rho^n}(\boldsymbol{r}) \otimes \sum_n \delta(\boldsymbol{r} - \boldsymbol{A}_n)\} \otimes \Delta\rho_N(-\boldsymbol{r}).$

Convolutions are associative, thus

$= \overline{\rho^n}(\boldsymbol{r}) \otimes \{\sum_n \delta(\boldsymbol{r} - \boldsymbol{A}_n) \otimes \Delta\rho_N(-\boldsymbol{r})\}$

$= \overline{\rho^n}(\boldsymbol{r}) \otimes \{\sum_n \int \delta(\boldsymbol{r} - \boldsymbol{A}_n)\, \Delta\rho_N(-\boldsymbol{r})\}$

$= \overline{\rho^n}(\boldsymbol{r}) \otimes \sum_n \Delta\rho_N(-\boldsymbol{A}_n).$

However, $\sum_n \Delta\rho_N(-\boldsymbol{A}_n) = 0$. Thus

$\bar{F}_N(\boldsymbol{R})\Delta F_N^*(\boldsymbol{R}) = 0.$

Similarly, $\bar{F}_N^*(\boldsymbol{R})\Delta F_N(\boldsymbol{R}) = 0.$

Eq. 2.11 takes the new form

$$I_N(\boldsymbol{R}) = \bar{F}_N(\boldsymbol{R})\bar{F}_N^*(\boldsymbol{R}) + \Delta F_N(\boldsymbol{R})\Delta F_N^*(\boldsymbol{R}) \qquad (2.12)$$

The first term gives the Bragg intensity due to the average crystal while the second term gives the diffuse intensity due to the deviations of the imperfect crystal from the average crystal.

Eq. 2.12 can be rewritten as the sum of Fourier transforms of the Patterson function $P_{avg}(\boldsymbol{x})$ of the average crystal and the Patterson function $P_{dev}(\boldsymbol{x})$ of the deviation crystal as follows:

$$I_N(\boldsymbol{R}) = \int_{-\infty}^{\infty} P_{avg}(\boldsymbol{x})\, exp(2\pi i \boldsymbol{R}.\boldsymbol{x}) d\boldsymbol{x} + \int_{-\infty}^{\infty} P_{dev}(\boldsymbol{x})\, exp(2\pi i \boldsymbol{R}.\boldsymbol{x}) d\boldsymbol{x}$$

In routine crystal structure analyses, only the first term is considered. The Patterson function obtained from the observed Bragg intensities are used to solve the phase problem (Dunitz, 1995). The use of the second term recently has been increasingly applied to the modeling of disordered structures. It is the most important quantity in the analysis of the difference pair distribution function (ΔPDF) (Weber & Simonov, 2012; Simonov *et al.*, 2014).

In the following subsections, different types of disorder present in crystals will be discussed. General expressions derived in the present section will be used where appropriate.

### 2.1.1 Different types of disorder present in crystals

#### 2.1.1.1 Static disorder

This type of disorder refers to a wide range of defects in a crystal. The important structural concept behind static disorder is that the disorder is solely due to the static arrangement of atoms or molecules in the crystal. Static disorder does not include disorder caused by motion of atoms or molecules within the crystal and it maintains a mean lattice as a function of temperature (Nield & Keen, 2001). Sub-categories of static disorder and how they manifest themselves in diffuse scattering in the diffraction pattern are described below.

##### 2.1.1.1.1 Substitutional disorder

In this type, the lattice positions in different unit cells may contain different elements. It is also possible that some lattice positions in some unit cells are void. An early and typical example of the former type of substitution is the $Cu_3Au$ crystal (Guinier, 1963) and an example for the latter type is high-$T_c$ superconductors with oxygen voids (Nield & Keen, 2001). The average structures of these types of disordered crystals will show mixed sites and the occupation factors associated with a particular site will give the proportions of different elements or voids averaged over the entire crystal. The average structure does not give the distribution of different elements in the crystal; this is the subject of modeling of local structure. Moreover, the existence of this type of disordered crystals is quite common; in fact, this is the predominant type of disorder found in alloys and non-stoichiometric materials, for example, oxides, nitrides and carbides of transition metals (Nield & Keen, 2001).

The structure factor for random substitution disorder can be derived from eq. 2.9. Since the crystal maintains a mean lattice, the displacements of atoms from their mean positions are ignored for the moment. Furthermore, the following assumptions are implied.

1. The crystal contains $N$ unit cells and each unit cell has only one atom in it.
2. There are only two types of atoms A and B in the crystal.
3. They are randomly distributed in the crystal with proportions $c_A$ and $c_B$, with $c_A + c_B = 1$.
4. The atomic form factors of atoms A and B are $f_A$ and $f_B$ respectively.

5. The magnitudes of the atomic radii of A and B are equal.

According to eq. 2.9,

$$F_n(\boldsymbol{R}) = \bar{F}_n(\boldsymbol{R}) + \Delta F_n(\boldsymbol{R})$$

$\bar{F}_n(\boldsymbol{R})$ is given by eq. 2.7. Since in this case atomic displacements from their mean positions are assumed to be zero, $\Phi_I(\boldsymbol{R})$ =constant and $\boldsymbol{r}_I = \bar{\boldsymbol{r}}_I$. Thus,

$$\bar{F}_n(\boldsymbol{R}) = \sum_I c_I f_I(\boldsymbol{R}) exp(-2\pi i \boldsymbol{R}.\boldsymbol{r}_I) exp(-2\pi i \boldsymbol{R}.\boldsymbol{r}_n)$$

$$= [c_A f_A(\boldsymbol{R}) exp(-2\pi i \boldsymbol{R}.\boldsymbol{r}_A) + c_B f_B(\boldsymbol{R}) exp(-2\pi i \boldsymbol{R}.\boldsymbol{r}_B)] exp(-2\pi i \boldsymbol{R}.\boldsymbol{r}_n).$$

Since, for pure random substitutional disorder, $\boldsymbol{r} = \boldsymbol{r}_A = \boldsymbol{r}_B$.

$$\bar{F}_n(\boldsymbol{R}) = [c_A f_A(\boldsymbol{R}) + c_B f_B(\boldsymbol{R})] exp(-2\pi i \boldsymbol{R}.\boldsymbol{r}) exp(-2\pi i \boldsymbol{R}.\boldsymbol{r}_n)$$

$c_A f_A(\boldsymbol{R}) + c_B f_B(\boldsymbol{R})$ can be replaced with the average form factor $\bar{f}(\boldsymbol{R})$. Thus

$$\bar{F}_n(\boldsymbol{R}) = \bar{f}(\boldsymbol{R}) exp(-2\pi i \boldsymbol{R}.\boldsymbol{r}) exp(-2\pi i \boldsymbol{R}.\boldsymbol{r}_n)$$

$$= \bar{f}(\boldsymbol{R}) exp[-2\pi i \boldsymbol{R}.(\boldsymbol{r} + \boldsymbol{r}_n)] \qquad (2.13)$$

The average structure factor of the superposition wave from the crystal is

$$\bar{F}_N(\boldsymbol{R}) = \sum_n \bar{F}_n(\boldsymbol{R})$$

$$= \sum_n \bar{f}(\boldsymbol{R}) exp[-2\pi i \boldsymbol{R}.(\boldsymbol{r} + \boldsymbol{r}_n)] \qquad (2.14)$$

The Bragg intensity is obtained according to eq. 2.4 as

$$I_{Bragg}(\boldsymbol{R}) = \bar{F}_N(\boldsymbol{R}) \bar{F}_N^*(\boldsymbol{R})$$

$$= \sum_n \sum_{n'} \bar{f}(\boldsymbol{R}) \bar{f}^*(\boldsymbol{R}) exp[-2\pi i \boldsymbol{R}.(\boldsymbol{r} + \boldsymbol{r}_n)] \, exp[2\pi i \boldsymbol{R}.(\boldsymbol{r} + \boldsymbol{r}_{n'})]$$

$$= \bar{f}^2(\boldsymbol{R}) \sum_n \sum_{n'} exp[-2\pi i \boldsymbol{R}.\{(\boldsymbol{r} + \boldsymbol{r}_n) - (\boldsymbol{r} + \boldsymbol{r}_{n'})\}]$$

$$= \bar{f}^2(\boldsymbol{R}) \sum_n \sum_{n'} exp[-2\pi i \boldsymbol{R}.\{\boldsymbol{r}_n - \boldsymbol{r}_{n'}\}].$$

The Bragg scattering is non-zero only for $\boldsymbol{R} = h\mathbf{a}^* + k\mathbf{b}^* + l\mathbf{c}^*$ where $h$, $k$ and $l$ are integers. The vector $\{\boldsymbol{r}_n - \boldsymbol{r}_{n'}\}$ defines points on a regular lattice. Under these conditions, the Bragg intensity is equal to

$$I_{Bragg}(\boldsymbol{R}) = N^2 \bar{f}^2(\boldsymbol{R}). \qquad (2.15)$$

Bragg scattering depends on the scattering vector because of its periodic nature. The intensity remains constant throughout reciprocal space in the case of point atoms. However, if the atoms are represented by Gaussian functions the Bragg intensity will follow the scattering factor distribution.

$\Delta F_n(\boldsymbol{R})$ is given by eq. 2.8 as follows:

$$\Delta F_n(\boldsymbol{R}) = f_I^n(\boldsymbol{R}) exp(-2\pi i \boldsymbol{R}.\boldsymbol{r}_I) exp(-2\pi i \boldsymbol{R}.\boldsymbol{r}_n) - \bar{F}(\boldsymbol{R})$$

$$= f_I^n(\boldsymbol{R}) exp(-2\pi i \boldsymbol{R}.\boldsymbol{r}_I) exp(-2\pi i \boldsymbol{R}.\boldsymbol{r}_n) - \bar{f}(\boldsymbol{R}) exp(-2\pi i \boldsymbol{R}.\boldsymbol{r}) exp(-2\pi i \boldsymbol{R}.\boldsymbol{r}_n).$$

Since $\boldsymbol{r} = \boldsymbol{r}_I$,

$$\Delta F_n(\boldsymbol{R}) = \left[f_I^n(\boldsymbol{R}) - \bar{f}(\boldsymbol{R})\right] exp(-2\pi i \boldsymbol{R}.\boldsymbol{r}) exp(-2\pi i \boldsymbol{R}.\boldsymbol{r}_n).$$

Let $\Delta f_I^n(\boldsymbol{R}) = \left[f_I^n(\boldsymbol{R}) - \bar{f}(\boldsymbol{R})\right]$. Thus,

$$\Delta F_n(\boldsymbol{R}) = \Delta f_I^n(\boldsymbol{R}) exp(-2\pi i \boldsymbol{R}.\boldsymbol{r}) exp(-2\pi i \boldsymbol{R}.\boldsymbol{r}_n)$$

$$= \Delta f_I^n(\boldsymbol{R}) exp[-2\pi i \boldsymbol{R}.(\boldsymbol{r} + \boldsymbol{r}_n)]. \qquad (2.16)$$

The $n^{\text{th}}$ unit cell contains either a type A or a type B atom. Therefore,

$$f_I^n(\boldsymbol{R}) = \{f_A^n(\boldsymbol{R}), f_B^n(\boldsymbol{R})\}$$

$$\Delta f_I^n(\boldsymbol{R}) = \{\Delta f_A^n(\boldsymbol{R}), \Delta f_B^n(\boldsymbol{R})\}$$

The difference structure factor of the superposition wave from the crystal is

$$\Delta F_N(\boldsymbol{R}) = \sum_n \Delta F_n(\boldsymbol{R})$$

$$= \sum_n \Delta f_I^n(\boldsymbol{R}) exp[-2\pi i R.(\boldsymbol{r} + \boldsymbol{r}_n)]. \qquad (2.17)$$

According to eq. 2.4, the diffuse intensity can be written as

$$I_{diffuse}(\boldsymbol{R}) = \Delta F_N(\boldsymbol{R}) \Delta F_N^*(\boldsymbol{R})$$

$$= \sum_n \sum_{n'} \Delta f_I^n(\boldsymbol{R}) \Delta f_I^{n'}(\boldsymbol{R}) exp[-2\pi i \boldsymbol{R}.(\boldsymbol{r} + \boldsymbol{r}_n)] exp[2\pi i \boldsymbol{R}.(\boldsymbol{r} + \boldsymbol{r}_{n'})]$$

$$= \sum_n \sum_{n'} \Delta f_I^n(\boldsymbol{R}) \Delta f_I^{n'}(\boldsymbol{R}) exp[-2\pi i \boldsymbol{R}.\{(\boldsymbol{r} + \boldsymbol{r}_n) - (\boldsymbol{r} + \boldsymbol{r}_{n'})\}]$$

$$= \sum_{n=n'} \Delta f_I^{n\,2}(\boldsymbol{R}) + \sum_n \sum_{n' \neq n} \Delta f_I^n(\boldsymbol{R}) \Delta f_I^{n'}(\boldsymbol{R}) exp[-2\pi i \boldsymbol{R}.\{\boldsymbol{r}_n - \boldsymbol{r}_{n'}\}].$$

The second term is equal to zero and thus the diffuse intensity is

$$I_{diffuse}(\boldsymbol{R}) = \sum_n \Delta f_I^{n\,2}(\boldsymbol{R}) = N\left[c_A\left(f_A^n(\boldsymbol{R}) - \bar{f}(\boldsymbol{R})\right)^2 + c_B\left(f_B^n(\boldsymbol{R}) - \bar{f}(\boldsymbol{R})\right)^2\right]. \quad (2.18)$$

Eq. 2.18 can be expressed in a much simpler way as follows:

$$I_{diffuse}(\boldsymbol{R}) = N\left[c_A\left(f_A^n - \bar{f}\right)^2 + c_B\left(f_B^n - \bar{f}\right)^2\right]$$

$$= N\left[c_A\left(f_A^{n\,2} - 2f_A^n\bar{f} + \bar{f}^2\right) + c_B\left(f_B^{n\,2} - 2f_B^n\bar{f} + \bar{f}^2\right)\right]$$

By solving and rearranging the terms within square brackets,

$$I_{diffuse}(\boldsymbol{R}) = N\left[c_A f_A^{n\,2} + c_B f_B^{n\,2} - 2\bar{f}(c_A f_A^n + c_B f_B^n) + \bar{f}^2(c_A + c_B)\right]$$

Since $\bar{f} = (c_A f_A^n + c_B f_B^n)$

$$I_{diffuse}(\boldsymbol{R}) = N\left[c_A f_A^{n\,2} + c_B f_B^{n\,2} - \bar{f}^2\right]$$

$$= N\left[c_A f_A^{n\,2} + c_B f_B^{n\,2} - (c_A f_A^n + c_B f_B^n)^2\right]$$

$$= N\left[c_A f_A^{n\,2} + c_B f_B^{n\,2} - c_A{}^2 f_A^{n\,2} - 2c_A c_B f_A^n f_B^n - c_B{}^2 f_B^{n\,2}\right]$$

$$= N\left[c_A f_A^{n\,2}(1 - c_A) + c_B f_B^{n\,2}(1 - c_B) - 2c_A c_B f_A^n f_B^n\right]$$

Since $c_B = 1 - c_A$ and $c_A = 1 - c_B$,

$$= N\left[c_A c_B f_A^{n\,2} + c_A c_B f_B^{n\,2} - 2c_A c_B f_A^n f_B^n\right]$$

$$= N\left[c_A c_B (f_A^{n\,2} - 2f_A^n f_B^n + f_B^{n\,2}\right]$$

$$= N[c_A c_B (f_A^n - f_B^n)^2]$$

Finally the simple expression for the diffuse scattering is

$$I_{Diffuse}(\boldsymbol{R}) = N[c_A c_B (f_A^n(\boldsymbol{R}) - f_B^n(\boldsymbol{R}))^2]. \quad (2.19)$$

The important thing to note is that, according to eq. 2.19, the magnitude of the diffuse intensity depends on the difference between the atomic scattering factors of the two species. The largest diffuse intensity is possible when the difference is greatest and $c_A = c_B$, while the

minimum is possible when the two scattering factors are about the same magnitude. In such situations, the distinction between the two constituents may be possible with neutron diffraction provided that their neutron form factors are significantly different. The other important feature of this type of diffuse scattering is that it does not depend on the scattering vector as it does not involve any periodicity. In the case of point atom and random substitutional disorder, the diffuse intensity is uniformly distributed throughout the whole reciprocal space. However, if atoms are assumed to be a Gaussian distribution of electron densities, then the diffuse intensity will have a fall-off at higher diffraction angles. Also note that the difference form factor [i.e.$(f_A - f_B)$] does not need to follow a Gaussian distribution. Therefore, in the case of random substitution disorder, any modulation of the diffuse intensity in reciprocal space results from the difference form factor.

Finally the total intensity for a crystal with random substitutional disorder can be given as the combination of the Bragg intensity and the diffuse intensity.

$$I_{tot} = N^2 \bar{f}^2(\boldsymbol{R}) + N c_A c_B |f_A(\boldsymbol{R}) - f_B(\boldsymbol{R})|^2. \qquad (2.20)$$

So far, only the case of random substitutional disorder, in which atoms do not have any preference for their nearest neighbors, was considered. Such a situation in crystals is not common. Usually short-range correlations between atomic species in the crystal exist and they span over a few interatomic distances (Guinier, 1963). This type of correlation usually generates preferred species in the crystal. For example, type A atoms may prefer having the same type of atoms (i.e. A) in their environment or they may prefer the other type of atom (i.e. B) to be within their environment. Consequently, there may be a modulation in the diffuse intensity distribution that is different from that resulting from random substitutional disorder.

In order to derive intensity expressions for a crystal with short-range order, the same crystal with random substitutional disorder will be considered. In this case, it is assumed that a given atom has an influence on its surroundings, as discussed in the last paragraph. The strength of the influence will be assessed by a parameter called the *Order parameter* ($\alpha_m$) (Guinier, 1963). This can be given as follows:

$$\alpha_m = 1 - \frac{p_{A|B(m)}}{c_A} = 1 - \frac{p_{B|A(m)}}{c_B} \qquad (2.21)$$

In eq. 2.21, $p_{A|B(m)}$ and $p_{B|A(m)}$ are conditional probabilities and can be understood as follows:

$p_{A|B(m)}$ : the probability of finding an A atom at the end of the vector $\boldsymbol{x}_m$ given a B atom at the origin of $\boldsymbol{x}_m$.

$p_{B|A(m)}$ : the probability of finding a B atom at the end of the vector $\boldsymbol{x}_m$ given an A atom at the origin of $\boldsymbol{x}_m$.

Eq. 2.21 can be rewritten as,

$$p_{A|B(m)} = c_A(1 - \alpha_m) \qquad (2.22)$$

$$p_{B|A(m)} = c_B(1 - \alpha_m) \qquad (2.23)$$

By adding eqs. 2.22 and 2.23,

$p_{A|B(m)} + p_{B|A(m)} = (c_A + c_B)\,(1 - \alpha_m)$.

Since $c_A + c_B = 1$,

$$p_{A|B(m)} + p_{B|A(m)} = (1 - \alpha_m). \qquad (2.24)$$

The maximum and the minimum values of the right side of eq. 2.24 are 2 and 0 respectively. Therefore, the order parameter has the range $-1 \leq \alpha_m \leq +1$. By looking at eq. 2.22 or 2.23 and substituting suitable values for the order parameter, various situations within the crystal can be realized.

For example, $\alpha_m < 0$ results in the situation of $p_{A|B(m)} > c_A$. This means that atoms A prefer atoms B to be at $\boldsymbol{x}_m$ for small *m* values. $\alpha_m = 0$ results in the situation of $p_{A|B(m)} = c_A$ indicating a random substitutional disorder, as discussed earlier. $\alpha_m > 0$ results from the situation where $p_{A|B(m)} < c_A$, indicating that atoms of the same type prefer to span $\boldsymbol{x}_m$. The extremities -1 and +1 of $\alpha_m$ indicate the situations of complete mixing [superstructure, $(AB)_N$] and phase separation [$A_N B_N$], respectively.

Let the proportions of the various types of pairs separated by the vector $\boldsymbol{x}_m$ in the crystal be $N_{AA}$ , $N_{AB}$ , $N_{BA}$ , $N_{BB}$. These proportions must satisfy the condition (Welberry, 2004) that

$$N_{AA} + N_{AB} + N_{BA} + N_{BB} = 1.$$

Conditional probabilities are

$$p_{A|B(m)} = \frac{N_{AB}}{N_{AA}+N_{AB}} \qquad (2.25)$$

$$p_{B|A(m)} = \frac{N_{BA}}{N_{BB}+N_{BA}} \qquad (2.26)$$

Cross multiplication of eq. 2.21 yields

$$p_{A|B(m)}c_B = p_{B|A(m)}c_A. \qquad (2.27)$$

When both sides of eq. 2.27 are multiplied by the number of atoms in the crystal (i.e. *N*), it follows that the number of A-B pairs is equal to the number of B-A pairs. This means that the joint probabilities of A-B pairs and B-A pairs are identical. Marginal probabilities (i.e. $c_A$ and $c_B$) are obtained by the ratios between the joint probabilities and the conditional probabilities as follows:

$$c_A = \frac{N_{AB}}{N_{AB}/(N_{AA}+N_{AB})} = N_{AA} + N_{AB}$$

$$c_B = \frac{N_{BA}}{N_{BA}/(N_{BB}+N_{BA})} = N_{BB} + N_{BA}$$

The diffuse intensity $I_{Diffuse}(\boldsymbol{R})$ for the deviation crystal with short-range order is easily obtained by incorporating the $\alpha_m$ into eq. 2.19. That can be given as follows,

$$I_{Diffuse}(\boldsymbol{R}) = Nc_Ac_B|f_A(\boldsymbol{R}) - f_B(\boldsymbol{R})|^2 \sum_{m=-\infty}^{\infty} \alpha_m exp(2\pi i \boldsymbol{R}.\boldsymbol{x}_m). \qquad (2.28)$$

Since $|\boldsymbol{x}_m| = |\boldsymbol{x}_{-m}|$: $\alpha_m = \alpha_{-m}$ and $\alpha_0 = 1$. Then eq. 2.28 can be rewritten as follows:

$$I_{Diffuse}(\boldsymbol{R}) = Nc_Ac_B|f_A(\boldsymbol{R}) - f_B(\boldsymbol{R})|^2\{1 + 2\sum_{m=1}^{\infty} \alpha_m cos(2\pi \boldsymbol{R}.\boldsymbol{x}_m)\}. \qquad (2.29)$$

According to eq. 2.29, the diffuse intensity is the sum of the diffuse intensity when there is no short-range order and a series of terms which oscillate repeatedly with a period equal to the reciprocal lattice vector. The periodic nature of short-range order diffuse scattering can be used to separate it from other types of diffuse scattering (Guinier, 1963; Fultz & Howe, 2013).

#### 2.1.1.1.2 Displacement disorder

This type of disorder refers to the situation in which the atoms are displaced from their average positions in the crystal lattice. In the case of pure displacement disorder, all crystal imperfections are solely due to the atomic displacements.

In order to derive expressions for the structure factors and the intensities in the diffraction pattern from a crystal with pure displacement disorder, the following assumptions are made.

1. The crystal contains *N* unit cells.
2. Each unit cell contains only one atom of type A whose atomic scattering power is represented by $f_A$.
3. The vector $\boldsymbol{r}_A$ is from the unit cell origin to the center of the electron density of atom A.
4. The distribution function of $\boldsymbol{r}_A$ is $\varphi_A(\boldsymbol{r})$.

The average electron density in the average unit cell is located at $\bar{\boldsymbol{r}}_A$ obtained from

$$\bar{\boldsymbol{r}}_A = \int \boldsymbol{r}\varphi_A(\boldsymbol{r} - \boldsymbol{r}_A)d\boldsymbol{r}$$

The average electron density $\overline{\rho^n}(\boldsymbol{r})$ in the $n^{\text{th}}$ unit cell is

$$\overline{\rho^n}(\boldsymbol{r}) = \rho_A(\boldsymbol{r}) \otimes \varphi_A(\boldsymbol{r} - \bar{\boldsymbol{r}}_A - \boldsymbol{r}_n). \qquad (2.30)$$

The Fourier transform of the average electron density corresponds to the average structure factor and is

$$\begin{aligned}\bar{F}_n(\boldsymbol{R}) &= f_A(\boldsymbol{R})\Phi_A(\boldsymbol{R})exp(-2\pi i\boldsymbol{R}.\bar{\boldsymbol{r}}_A)exp(-2\pi i\boldsymbol{R}.\boldsymbol{r}_n) \\ &= f_A(\boldsymbol{R})\Phi_A(\boldsymbol{R})exp[-2\pi i\boldsymbol{R}.(\bar{\boldsymbol{r}}_A + \boldsymbol{r}_n)]. \qquad (2.31)\end{aligned}$$

where $f_A(\boldsymbol{R})$ and $\Phi_A(\boldsymbol{R})$ are the Fourier transformed quantities of $\rho_A(\boldsymbol{r})$ and $\varphi_A(\boldsymbol{r})$, respectively.

The structure factor of the superposition wave of the crystal is

$$\begin{aligned}\bar{F}_N(\boldsymbol{R}) &= \textstyle\sum_n \bar{F}_n(\boldsymbol{R}) \\ &= \textstyle\sum_n f_A(\boldsymbol{R})\Phi_A(\boldsymbol{R})exp[-2\pi i\boldsymbol{R}.(\bar{\boldsymbol{r}}_A + \boldsymbol{r}_n)].\end{aligned}$$

The Bragg intensity of the superposition wave is

$$\begin{aligned}I_{Bragg}(\boldsymbol{R}) &= \bar{F}_N(\boldsymbol{R})\bar{F}_N^*(\boldsymbol{R}) \\ &= \textstyle\sum_n \sum_{n'} f_A(\boldsymbol{R})f_A^*(\boldsymbol{R})\Phi_A(\boldsymbol{R})\Phi_A(\boldsymbol{R})exp[-2\pi i\boldsymbol{R}.(\bar{\boldsymbol{r}}_A + \boldsymbol{r}_n)]\, exp[2\pi i\boldsymbol{R}.(\bar{\boldsymbol{r}}_A + \boldsymbol{r}_{n'})] \\ &= f_A^2(\boldsymbol{R})\Phi_A^2(\boldsymbol{R}) \textstyle\sum_n \sum_{n'} exp[-2\pi i\boldsymbol{R}.\{(\bar{\boldsymbol{r}}_A + \boldsymbol{r}_n) - (\bar{\boldsymbol{r}}_A + \boldsymbol{r}_{n'})\}]\end{aligned}$$

$$= f_A^2(\boldsymbol{R})\Phi_A^2(\boldsymbol{R})\sum_n \sum_{n'} exp[-2\pi i \boldsymbol{R}.\{\boldsymbol{r}_n - \boldsymbol{r}_{n'}\}].$$

The Bragg scattering is obtained only when $\boldsymbol{R} = h\mathbf{a}^* + k\mathbf{b}^* + l\mathbf{c}^*$ where $h$, $k$ and $l$ are integers. The vector $(\boldsymbol{r}_n - \boldsymbol{r}_{n'})$ defines points on a regular lattice. Under these conditions, the Bragg intensity is equal to

$$I_{Bragg}(\boldsymbol{R}) = N^2 f_A^2(\boldsymbol{R}). \qquad (2.32)$$

Eq. 2.32 should be compared with eq. 2.15. The only difference between the two equations is that the atomic scattering factor of the type A atom in eq. 2.32 is replaced by the atomic scattering factor of an average atom type in eq. 2.15.

Let the electron density of the $n^{\text{th}}$ unit cell be $\rho_A^n(\boldsymbol{r})$. Then the difference electron density of the $n^{\text{th}}$ unit cell can be written as

$$\Delta\rho_A^n(\boldsymbol{r}) = \rho_A^n(\boldsymbol{r}) - \bar{\rho}(\boldsymbol{r}).$$

The Fourier transform of $\Delta\rho_A^n(\boldsymbol{r})$ is

$$\Delta F_n(\boldsymbol{R}) = f_A^n(\boldsymbol{R})exp(-2\pi i \boldsymbol{R}.\boldsymbol{r}_A^n)exp(-2\pi i \boldsymbol{R}.\boldsymbol{r}_n) - \bar{F}(\boldsymbol{R})$$

$$= f_A^n(\boldsymbol{R})exp(-2\pi i \boldsymbol{R}.\boldsymbol{r}_A^n)exp(-2\pi i \boldsymbol{R}.\boldsymbol{r}_n)$$

$$-f_A(\boldsymbol{R})\Phi_A(\boldsymbol{R})exp(-2\pi i \boldsymbol{R}.\bar{\boldsymbol{r}}_A)exp(-2\pi i \boldsymbol{R}.\boldsymbol{r}_n)$$

Since the crystal is made up of only type A atoms, $f_A^n(\boldsymbol{R}) = f_A(\boldsymbol{R})$. Thus,

$$\Delta F_n(\boldsymbol{R}) = f_A(\boldsymbol{R})exp(-2\pi i \boldsymbol{R}.\boldsymbol{r}_n)\{exp(-2\pi i \boldsymbol{R}.\boldsymbol{r}_A^n) - \Phi_A(\boldsymbol{R})exp(-2\pi i \boldsymbol{R}.\bar{\boldsymbol{r}}_A)\} \qquad (2.33)$$

The difference structure factor of the superposition wave of the crystal is

$$\Delta F_N(\boldsymbol{R}) = \sum_n \Delta F_n(\boldsymbol{R}).$$

The corresponding intensity can be written as

$$I_{diffuse}(\boldsymbol{R}) = \Delta F_N(\boldsymbol{R})\Delta F_N^*(\boldsymbol{R})$$

$$= \left\{\sum_n f_A(\boldsymbol{R})exp[-2\pi i \boldsymbol{R}(r_A^n + r_n)] - f_A(\boldsymbol{R})\Phi_A(\boldsymbol{R})exp[-2\pi i \boldsymbol{R}(\bar{\boldsymbol{r}}_A + \boldsymbol{r}_n)]\right\}$$

$$\left\{\sum_{n'} f_A^*(\boldsymbol{R})exp[2\pi i \boldsymbol{R}(r_A^{n'} + r_{n'})] - f_A^*(\boldsymbol{R})\Phi_A(\boldsymbol{R})exp[2\pi i \boldsymbol{R}(\bar{\boldsymbol{r}}_A + \boldsymbol{r}_{n'})]\right\}$$

$$= \sum_n \sum_{n'} f_A^2(\boldsymbol{R}) exp[-2\pi i \boldsymbol{R}(r_n - r_{n'})]\{exp\left[-2\pi i \boldsymbol{R}\left(r_A^n - r_A^{n'}\right)\right] - \Phi_A(\boldsymbol{R}) exp[-2\pi i \boldsymbol{R}(r_A^n - \bar{\boldsymbol{r}}_A)] - \Phi_A(\boldsymbol{R}) exp\left[-2\pi i \boldsymbol{R}\left(\bar{\boldsymbol{r}}_A - r_A^{n'}\right)\right] + \Phi_A^2(\boldsymbol{R}) exp[-2\pi i \boldsymbol{R}.(\bar{\boldsymbol{r}}_A - \bar{\boldsymbol{r}}_A)]\} \quad (2.34)$$

Eq. 2.34 shows an important feature of displacement disorder. When $R = 0$, the exponential terms equal unity. Also $\Phi_A(0) = 0$, because $\varphi_A(\boldsymbol{r})$ is a distribution function that integrates to unity. Thus the whole expression is zero. It shows that at the center of reciprocal space, the intensity due to displacement disorder is zero. $I_{diffuse}\ (\boldsymbol{R})$ increases as the distance from the center increases. Therefore, the absence of diffuse intensity near the origin of reciprocal space is a characteristic feature of displacement disorder that can often be used to identify the cause of the diffuse scattering.

The displacement of atoms from their average lattice sites usually occurs due to *thermal agitation* in crystals. The atoms in the crystal vibrate with an amplitude that increases with temperature. The amplitude of vibration will never become zero even at absolute zero temperature due to the zero point vibrations. Therefore, atoms are never static in the crystal. Displacement due to thermal agitation in crystals is a dynamic process. A detailed description of this type of disorder will be presented under the dynamic disorder section of this chapter (§2.1.12).

*Planar disorder*

Another type of displacement disorder in crystals is called *planar disorder*. In this situation, a set of parallel lattice planes keeps two-dimensional periodicity within each plane. The disorder occurs as a result of the irregular arrangement of these planes, either because the distance from one plane to the next is not constant, or the planes are displaced parallel to themselves in an irregular fashion, or different planes contain different atoms (Guinier, 1963). Next, the influence of the stacking disorder on the scattering power of the crystal will be presented.

The derivation presented below is essentially the result obtained by Berliner & Werner (1986). The intensity for a crystal of volume *V* containing *N* unit cells is given by

$$I_N(\boldsymbol{R}) = \sum_{n=1}^{N} \sum_{n'=1}^{N'} F_n(\boldsymbol{R}) F_{n'}^*(\boldsymbol{R}) exp[-2\pi i \boldsymbol{R}.(\boldsymbol{r}_a^n - \boldsymbol{r}_a^{n'})] \quad (2.35)$$

where $F_n(\boldsymbol{R})$ is the structure factor of the $n^{\text{th}}$ unit cell located at a distance $|\boldsymbol{r}_a^n|$ away from the arbitrarily chosen origin of the crystal. The vector $\boldsymbol{r}_a^n$ is written as a combination of the lattice vector $\boldsymbol{r}_n$ from the crystal origin to the origin of the nth unit cell and the vector $\boldsymbol{x}_n$ from the unit cell origin to the center of the electron density of the $n^{\text{th}}$ unit cell. Therefore,

$$\boldsymbol{r}_a^n = \boldsymbol{r}_n + \boldsymbol{x}_n \qquad (2.36)$$

Substituting eq. 2.36 in eq. 2.35,

$$I_N(\boldsymbol{R}) = \sum_{n=1}^{N}\sum_{n'=1}^{N'} F_n(\boldsymbol{R})F_{n'}^*(\boldsymbol{R})exp[-2\pi i\boldsymbol{R}.\{(\boldsymbol{r}_n - \boldsymbol{r}_{n'}) + (\boldsymbol{x}_n - \boldsymbol{x}_{n'})\})]$$

Let, $n' = n + m$ and $\boldsymbol{r}_m = \boldsymbol{r}_n - \boldsymbol{r}_{n'}$ and $\Delta\boldsymbol{x}_m = \boldsymbol{x}_n - \boldsymbol{x}_{n'}$; then

$$= \sum_{m=-N}^{N} exp(2\pi i\boldsymbol{R}.\boldsymbol{r}_m)\sum_{n=1}^{N-m} F_n(\boldsymbol{R})F_{n+m}^*(\boldsymbol{R})\, exp(2\pi i\boldsymbol{R}.\Delta\boldsymbol{x}_m) \qquad (2.37)$$

Also,

$$\boldsymbol{A}_m = m_1\boldsymbol{a} + m_2\boldsymbol{b} + m_3\boldsymbol{c}$$

where $m_1$, $m_2$ and $m_3$ are integers.

$$\boldsymbol{R} = h\boldsymbol{a}^* + k\boldsymbol{b}^* + l\boldsymbol{c}^*$$

Let $F_n(\boldsymbol{R})F_{n+m}^*(\boldsymbol{R}) = |F(\boldsymbol{R})|^2$.

Assuming that the crystal is of size $Na \times Nb$ unit cells in the transverse direction and $Nc$ unit cells along the stacking direction, eq. 2.37 can be rewritten as follows:

$$I_N(\boldsymbol{R}) = |F(\boldsymbol{R})|^2 \sum_{m1=-Na}^{Na}(Na - m1)\sum_{m2=-Nb}^{Nb}(Nb - m2)exp(2\pi i\boldsymbol{R}_{\boldsymbol{a}^*\boldsymbol{b}^*}.\boldsymbol{r}_{m1m2})$$

$$\sum_{m3=-Nc}^{Nc}(Nc - m3)exp(2\pi i\boldsymbol{R}_{\boldsymbol{c}^*}.\boldsymbol{r}_{m3})exp(2\pi i\boldsymbol{R}.\Delta\boldsymbol{x}_m)$$

To make the equation less crowded, the ranges of summations will be dropped from here on. The product $\boldsymbol{R}_{\boldsymbol{c}^*}.\boldsymbol{r}_{m3}$ is equal to $lm_3$. Let, $exp(2\pi i\boldsymbol{R}.\Delta\boldsymbol{x}_m) = Y_{m3}$

$$I_N(\boldsymbol{R}) = |F(\boldsymbol{R})|^2 \sum_{m1}(Na - m1)\sum_{m2}(Nb - m2)exp(2\pi i\boldsymbol{R}_{\boldsymbol{a}^*\boldsymbol{b}^*}.\boldsymbol{r}_{m1m2})$$

$$\sum_{m3}(Nc - m3)Y_{m3}exp(2\pi ilm_3)$$

For a macroscopic crystal, $Na$ and $Nb$ are large. Thus, $\frac{Na-m1}{Na} = 1$ and $\frac{Nb-m1}{Nb} = 1$. Therefore,

$$I_N(\boldsymbol{R}) = |F(\boldsymbol{R})|^2 \sum_{m1}\sum_{m2} exp(2\pi i\boldsymbol{R}_{\boldsymbol{a}^*\boldsymbol{b}^*}.\boldsymbol{r}_{m1m2})\sum_{m3}(Nc - m3)Y_{m3}exp(2\pi ilm_3)$$

The intensity is greatest at the reciprocal lattice lines normal to the basal plane specified by $h_0$ and $k_0$, where $h_0$ and $k_0$ are integers, 0, ±1, ±2, … This situation can be represented by two delta functions as follows:

$$I_N(\boldsymbol{R}) = |F(\boldsymbol{R})|^2[NaNb\delta(h-h_0)\delta(k-k_0)\sum_{m3}(Nc-m3)Y_{m3}exp(2\pi ilm_3)] \quad (2.38)$$

Eq. 2.38 gives the intensity variation of a layered crystal. Intensity is found at integer values of *h* and *k* only. The variation along the rows parallel to the stacking direction is determined by the $Y_{m3}$ term. If the atoms are always in the average lattice positions, the resulting arrangement is periodic, and that will lead to diffraction spots (Bragg reflections) at integer *l* along $\boldsymbol{c}^*$. In that case all $Y_{m3}$ are unity. Then the eq. 2.38 will take the form

$$I_N(\boldsymbol{R}) = |F(\boldsymbol{R})|^2[NaNb\delta(h-h_0)\delta(k-k_0)Nc\delta(l-l_0)].$$

If, on the other hand, the stack of layers is perturbed from the regular arrangement ($\Delta\boldsymbol{x}_m \neq 0$), the intensity variation along the rows are determined by the $Y_{m3}$ term.

Two types of displacements are possible. In the first type, the displacement is parallel to the stacking direction and only the $\Delta\boldsymbol{x}_{mc}$ is important. This situation can be realized as a row of *Nc* atoms, where each one is located at the position of the successive planes. Disorder is such that atoms in the linear lattice may be displaced from their average positions along **c**. If the distribution of points (atoms) is random, the resulting diffuse scattering changes as a function of the scattering vector only. The intermediate situation that corresponds with a slight deviation from the average positions will result a reduction of intensity of the Bragg reflections while increasing the width of the Bragg reflections with *l* (Guinier, 1963).

#### 2.1.1.1.2.1 Stacking faults

Layer displacements can occur not only along the direction of stacking, but also perpendicular to the stack i.e. parallel to the layers. The origin of stacking faults with respect to the energy of the crystal and layer symmetry is described in the next section (2.2). In this section, only the effect of stacking on the diffraction pattern will be described.

The irregularities made by stacking faults lead to modulations of the scattering intensity along rows of *l*. Any displacement parallel to the layer plane does not affect the distribution of intensity along 00*l* reciprocal lattice row. This is because the scattering vector $\boldsymbol{R}$ is normal to the displacement vector $\Delta\boldsymbol{x}_m$. The resulting dot product is zero and hence $exp(2\pi i\boldsymbol{R}.\Delta\boldsymbol{x}_m) =$

1. Therefore, along the 00*l* reciprocal lattice row, the scattering is concentrated around the nodes of the regular lattice and the width of the reflection envelope depends only on the number of planes along the stacking direction (Guinier, 1963). For any other reciprocal lattice row, there may be a modulation of intensity that depends on the displacement vector.

According to Guinier, α is the probability that there exists a fault at a given layer. Then the probability that there is no fault is (1- α). The probability that there is no fault on *m*3 consecutive layers is (1- $\alpha$)$^{m3}$. Then the intensity along *l* can be given by

$$I_N(\boldsymbol{R}) = |F(\boldsymbol{R})|^2[NaNb\delta(h-h_0)\delta(k-k_0)\sum_{m3}(Nc-m3)(1-\alpha)^{|m3|}exp(2\pi ilm_3)] \quad (2.39)$$

For an infinite stack of layers, $\frac{Nc-m3}{Nc} \approx 1$. Thus eq. 2.39 can be rewritten in the following form

$$I_N(\boldsymbol{R}) = |F(\boldsymbol{R})|^2[NaNb\delta(h-h_0)\delta(k-k_0)\sum_{m3=-\infty}^{\infty}(1-\alpha)^{|m3|}exp(2\pi ilm_3)]$$

$$= |F(\boldsymbol{R})|^2[NaNb\delta(h-h_0)\delta(k-k_0)\{1+2\sum_{m3=1}^{\infty}(1-\alpha)^{|m3|}cos(2\pi lm_3)\}] \quad (2.40)$$

According to Eq. 2.40, the greatest $I_N(\boldsymbol{R})$ corresponding to a particular integral *l* is obtained when α is zero, meaning that there are no irregularities in the stack. When disorder is present, it only broadens the reflection profile symmetrically without shifting the peak maximum. The situation α = 1 corresponds to a random arrangement of layers along the stacking direction. In this case, the second term in eq. 2.40 is zero and only the first term is remaining. The intensity is distributed along *l* and is dependent only on the layer form factor.

*Linear disorder*

Another type of disorder is called *linear disorder*. In this situation, the periodicity of the lattice is preserved in only one direction. The crystal is composed of periodic parallel rows of atoms, but these rows are irregularly arranged in the crystal, one relative to another (Guinier, 1963). Also, it is possible that some lattice sites are occupied by different types of atoms. The scattering resulting from this type of disordered crystal is then concentrated on parallel planes in reciprocal space, normal to the rows. The distance between the planes of intensity in reciprocal space is equal to the inverse of the periodicity of the row crystal. An example of linear disorder is given in Aebischer *et al*. (2006).

### 2.1.1.2 Dynamic disorder

Dynamic disorder implies any disorder in crystals that changes with time. The most common type of dynamic disorder is due to thermal motion of atoms or molecules in crystals. As a result of the vibrations of atoms in the crystal, their atomic positions deviate from their average positions by a small fraction of the interatomic distance. Thermal motion occurs even at absolute zero due to the zero point vibrations associated with atoms or molecules. Disorder due to thermal motion manifests itself in the diffraction pattern as clouds of diffuse scattering and is often called thermal diffuse scattering (TDS).

In the first part of this section, the effect of atomic vibrations on the Bragg scattering will be discussed. In the second part, the diffuse scattering caused by the thermal motion of atoms in the crystal will be discussed.

The atomic vibrations affect the time and space averaged electron density distribution of atoms by making the distribution more diffuse. This results in a rapid fall-off in the magnitude of the atomic scattering factors (Dunitz, 1995). With an increase of temperature, the atomic mean vibration amplitude also increases. Consequently, the reduction of atomic scattering power at higher angles becomes more pronounced. The reduction of the scattering power is accounted for by a multiplication of the scattering power of the atom at rest with an exponential factor $G(\boldsymbol{R})$. Thus:

$$f(\boldsymbol{R}) = f^0(\boldsymbol{R})G(\boldsymbol{R}) \qquad (2.41)$$

where $f(\boldsymbol{R})$ and $f^0(\boldsymbol{R})$ are the atomic scattering factors not at rest and at rest, respectively. $G(\boldsymbol{R})$ is the modifier for $f^0(\boldsymbol{R})$. For harmonic isotropic motion it is equal to $exp\left(-B\frac{sin^2\theta}{\lambda^2}\right)$, where $B = 8\pi^2\langle U^2\rangle$. $\langle U^2\rangle$ is a mean square vibrational amplitude. Since Peter Debye was the first person to show this effect, the above exponential factor is termed the Debye factor. Because of the slight modification introduced later by Waller, sometimes it is known as Debye-Waller factor (*D*) (Dunitz, 1995).

Thermal vibrations in crystals are anisotropic, meaning that the mean square amplitude varies with direction. The Debye-Waller factor depends on the direction of the scattering vector $\boldsymbol{R}$. In such situations, $G(\boldsymbol{R})$ will take the form

$$G(\boldsymbol{R}) = exp[-2\pi^2(U_1^2R_1^2 + U_2^2R_2^2 + U_3^2R_3^2)]$$

where $R1$, $R2$, $R3$ are the components of the scattering vector $\boldsymbol{R}$ along the principle axes of the vibration ellipsoid. $U_1^2$, $U_2^2$, $U_3^2$ are the mean square amplitudes of vibration along the principle axes.

The thermal vibrations of atoms in crystals do not broaden the Bragg peak profiles. The Bragg diffraction pattern of a crystal is the same as that of a perfect crystal, except for the intensity reduction due to the Debye-Waller factor ($D$). The ratio of the intensity reduction compared to the corresponding intensity when the atom at rest is

$$(e^{-D})^2 = exp(-2D) \qquad (2.42)$$

From the point of view of elastic scattering, the principle of energy conservation raises the question of where the lost intensity goes. The missing intensity is found in the background (Guinier, 1963) and is generally called thermal diffuse scattering (TDS). The distribution of TDS in reciprocal space can be described by looking into the Debye-Waller factor. This factor depends on $|\boldsymbol{R}|$ and the mean-square amplitude of the vibration. In general, the TDS increases with $|\boldsymbol{R}|$ and the mean-square displacement of vibration.

Another type of dynamic disorder that can be found in crystals is due to reorientation of molecules in different unit cells in the crystal. If a molecule or part of a molecule is conformationally flexible, depending on the energy barrier between these conformations, the molecule can transform to another conformation causing dynamic diffuse scattering in the diffraction pattern. This type of disorder is sometimes known as orientational/rotational disorder.

#### 2.1.1.3 Magnetic disorder

One of the most common forms of magnetic disorder occurs when the magnetic spin of the specific same site is different in different unit cells. This situation is similar to substitutional disorder in non-magnetic structures. In addition to this type, other forms of magnetic disorder are also common (Nield & Keen, 2001).

## 2.2 Polytypism in layered structures

Polytypism refers to the situation in which many modes of stacking are possible for a layered structure. The original idea of polytypism and polytypes came from Baumhauer in 1912 and 1915 as a result of his investigations of many SiC single-crystals by optical goniometry (Baumhauer, 1912, 1915). He discovered three SiC types and called this phenomenon polytypism. X-ray crystal-structure determination of those three types later showed that they can be interpreted as members of a family of structures built from identical layers, but differing in their stacking mode (Durovič, 2006).

Over time, many new polypypic compounds have been found and also many views on polytypism have been presented (Thompson, 1981; Angel, 1986). All cases clearly showed that the geometric relationships between nearest-neighbor layers are preserved. Investigations into mica polytypes showed that mica exhibits a large variety of isomorphous replacements (substitutional disorder). Also certain chemical compositions stabilize certain polytypes, raising the question of the chemical composition of polytypic layers. At this point, it was accepted that the sequence of individual kinds of layers in polytypes of the same family should remain the same and that the relative positions in the adjacent layers cannot be completely random. According to this idea, the structures made of mixed layers were declared as non-polytypic. Due to many views, there was a clear need for a proper definition of polytypism. The IUCr *Ad-Hoc* committee on the Nomenclature of Disordered, Modulated and Polytype Structures developed the following official definition of polytypism in 1984.

"An element or compound is polytypic if it occurs in several different structural modifications, each of which may be regarded as built up by stacking layers of (nearly) identical structure and composition, and if the modifications differ only in their stacking sequence. Polytypism is a special case of polymorphism: the two-dimensional translations within the layers are (essentially) preserved whereas the lattice spacings normal to the layers vary between polytypes and are indicative of the stacking period. No such restrictions apply to polymorphism." (Guinier *et al*., 1984).

Although the above official definition allows one to abstract the chemical composition and structural rigidity of layers, the most critical drawback is the fact that it does not clearly define the 'layers' and their stacking modes. Also, it does not state the conditions under which a polytype belongs to a family (Durovič, 2006). Consequently, the assignment of a polytype to

a family is mainly dependent on the level of idealization and/or abstraction of the composition and the planarity of layers.

### 2.2.1 Order-Disorder (OD) theory of polytypes

Kate Dornberger-Schiff first introduced the basic notion of order-disorder structures in 1956 and she and her coworkers further developed this into a dynamic field of research through a series of papers (Dornberger-Schiff, 1956, 1961, 1964, 1966, 1979, and 1982). Her theory on OD structures abstracted from the chemical composition completely and looked for the reasons for polytypism by looking into the symmetry of layers and symmetry relationships between adjacent layers. This theory not only generalized the basic symmetry concepts in classical crystallography, but also redefined the notion of a crystal.

"The introduction of the notion of OD structures was, in the first place, motivated by the task of determining the structure of a crystal exhibiting one-dimensional disorder. Considerations of the causes leading to the tendency to disorder of some crystalline substances led, furthermore, to the conviction that the classical definition of a crystal as a body with three-dimensional periodicity may have its shortcomings; properly speaking, it is not truly atomistic, although it refers to atoms: periodicity, by its very nature, makes statements on parts of the body which are far apart, whereas the forces between atoms are short range forces, falling off rapidly with distance. A truly atomistic crystal definition should, therefore, refer only to the neighboring parts of the structure, and contain conditions understandable from the point of view of atomic theory" (Dornberger-Schiff, 1979).

A crystal in the classical sense may be described as a pile of two-dimensionally ordered periodic layers in which all subsequent layers have one definite arrangement relative to the previous layer, which generates the periodic structure also in the third dimension. Any pair of adjacent layers is geometrically equivalent to any other such pair due to geometric operations between them. This property is at the heart of OD theory.

"This equivalence seems the most important feature of crystals, and may be used for a revision of the crystal definition" (Dornberger-Schiff, 1979).

According to Merlino (1997), the equivalence of pairs of adjacent layers is a necessary condition for periodicity, but when two adjacent layers are equivalent in more than one geometrically equivalent way, an infinite number of ordered as well as disordered layer sequences are possible. OD theory, in general, allows one to understand the possibility of

occurrence of many stacking sequences as well as to select the most probable sequences among many possibilities. Therefore, OD theory is important in order to understand and to systematically analyze, in the simplest case, one-dimensional disorder in crystals.

According to OD theory, a polytype family contains periodic as well as non-periodic members. Non-periodic polytypes do not comply with the classical definition of crystals. However, OD theory places them, together with the periodic ones, in the same hierarchy of the so called VC (Vicinity Condition) structures. The reason is that all periodic as well as non-periodic structures can be thought of as consisting of disjunct, two-dimensionally periodic slabs, the VC layers, which are stacked together according to rules in the Vicinity Condition (Durovič, 2006).

*The Vicinity Condition in OD theory*

The Vicinity Conditions (Dornberger-Schiff, 1979) are at the heart of OD theory. They allow one to judge whether a given layered structure can be considered as an OD structure or not. All Vicinity Conditions are presented in International Tables for Crystallography Volume C. They are:

($\alpha$) VC layers are either geometrically equivalent or, if not, they are relatively few in kind.

($\beta$) Translation groups of all VC layers are either identical or they have a common subgroup.

($\gamma$) Equivalent sides of equivalent layers are faced by equivalent sides of adjacent layers so that the resulting pairs are equivalent.

In the case of ordered structures, the stacking of VC layers is unambiguous at every layer boundary. On the other hand, if the stacking of VC layers is ambiguous at every layer boundary, an OD structure results and the corresponding layers (VC layers) become OD layers. At this point it is important to keep in mind that those OD layers do not need to comply with molecular layers. In fact they may contain half atoms at their boundary. Also the choice of OD layers can depend on the polytypism and on the degree of symmetry idealization (Grell, 1984).

*Different symmetries in OD theory*

OD theory is concerned mainly with the local symmetry principles of structures. It explains the relationship between the symmetry of the layer as well as the symmetry between two

adjacent layers. Therefore, OD theory recognizes two main types of symmetries (Durovič, 2006).

1. λ-symmetry: the symmetry proper of the OD layer. There are 80 layer groups in total (17 polar, 63 non-polar layer groups).
2. σ-symmetry: the symmetry of a layer pair. Sometimes this symmetry is called coincidence symmetry.

Symmetry operations are divided into two classes, each with two types.

1. τ-operations: layer symmetry (λ) or coincidence (σ) operations which do not turn the layer upside down with respect to the layer stacking direction.
2. ρ-operations: layer symmetry (λ) or coincidence (σ) operations which do turn the layer upside down with respect to the layer stacking direction.

The above symmetry operations apply only to a layer or a pair of layers. Therefore, those operations are called partial operations (POs). A set of σ operations does not form a group, because those operations are valid only for a pair of adjacent layers, not for the entire structure. Instead of a group, they form a groupoid of POs.

Partial operation can be multiplied in an analogous way to the proper operations in a group. For example,

$\tau.\tau = \rho.\rho = \tau$

$\tau.\rho = \rho.\tau = \rho$

Another useful concept in OD theory is the so-called "continuation" and "reverse continuation". Let *p*, *q* and *r* represent three consecutive layers in an OD structure. The two layer pairs *pq* and *qr* are equivalent if there exists an (partial) operation which can bring *p* to *q* as well as *q* to *r*. Such an (partial) operation has a continuation from one layer pair to the next layer pair. The POs with continuation can be either τ-type or ρ-type. For example, the two layer pairs *pq* and *qr* are equivalent if there exists either a PO, ${}_{p,q}\tau$ with continuation to ${}_{q,r}\tau$ or a PO, ${}_{q,q}\rho$ with continuation to ${}_{p,r}\rho$.

The reverse continuation is realized when a σ-ρ-PO converts any layer into the adjacent one or *vice versa*. This role is generally played by an inversion center of the σ-type.

### 2.2.2 Stacking ambiguities in close-packed structures and the NFZ relationship

The close packing of equal spheres is an excellent example for a system with one-dimensional disorder. The layers built up with equal spheres are two-dimensionally periodic objects. However, their stacking is ambiguous due to the fact that the second layer ina pair of layers can occupy any one of the two geometrically equivalent positions (B and C) relative to the first layer, as shown in Fig. 2.1.

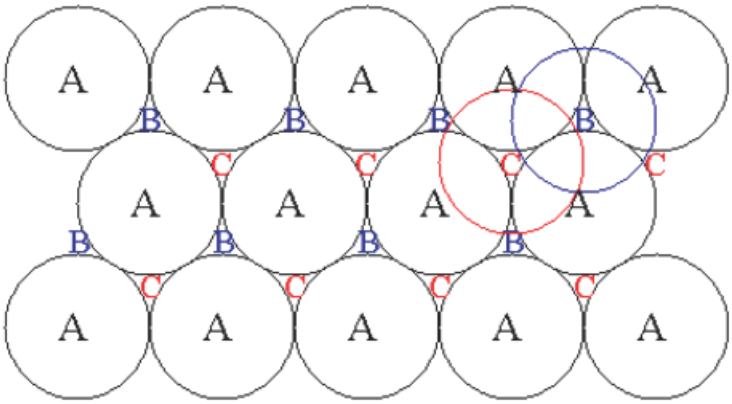


Figure 2.1: Schematic representation of close-packing of equal spheres. The first layer is composed of spheres at A positions. B and C are the geometrically equivalent positions in the next layer. Spheres can exclusively occupy either B positions or C positions (Nespolo, 2009).

Note that the B and C position are geometrically, but not translationally, equivalent. This equivalence is a result of mirror planes perpendicular to the first layer and passing through the centers of mutually contacting A spheres. These mirrors transform A into itself, but B and C into each other. Therefore, the resulting two adjacent layer pairs, AB and AC, are also geometrically equivalent. The layer group of any layer (see Fig 2.2), taken independently, is $P(6/m)mm$. This group contains 24 equivalent operations. All operations are given in Table 2.1. Of these, only 12 are τ-operations and they form the subgroup $P(6)mm$. Of the 12 τ-operations, only 6 (i.e. 1, $6_2$, $6_4$, $3\times m$) have a continuation to the next layer (Table 2.1). This is schematically shown in Fig. 2.2.

Table 2.1: All symmetry operations of a single layer (λ-symmetry) and a pair of layers (σ-symmtry) of close-packed structures of equal spheres.

| | λ-symmetry | σ-symmetry |
|---|---|---|
| τ-operations | *x,y,z*; *-y,x-y,z*; *-x+y,-x,z*; *-x,-y,z*; *y,-x+y,z*; *x-y,x,z*; *-y,-x,z*; *-x+y*,y,z; *x,x-y,z*; *y,x,z*; *x-y,-y,z*; *-x,-x+y,z* | *x,y,z*; *-y,x-y,z*; *-x+y,-x,z*; *-y,-x,z*; *-x+y*,y,z; *x,x-y,z*; |
| ρ-operations | *y,x,-z*; *x-y,-y,-z*; *-x,-x+y,-z*; *-y,-x,-z*; *-x+y,y,-z*; *x,x-y,-z*; *-x,-y,-z*; *y,-x+y,-z*; *x-y,x,-z*; *x,y,-z*; *-y,x-y,-z*; *-x+y,-x,-z* | None |

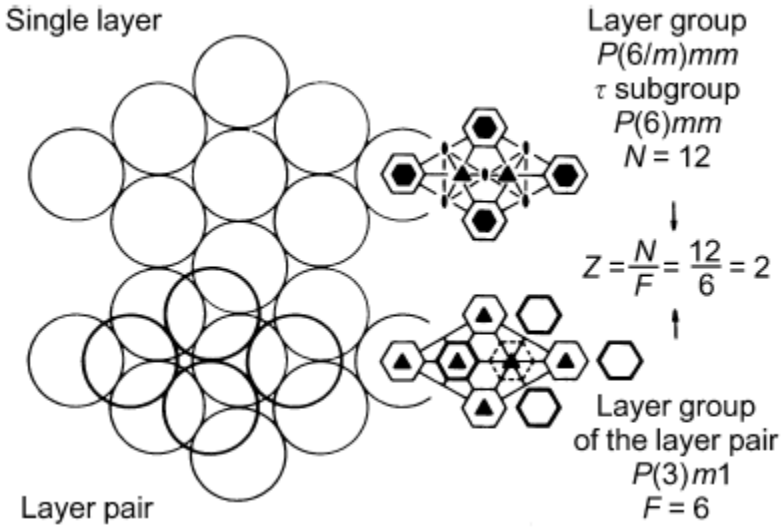


Figure 2.2: Schematic representation of layer groups for a single layer and a pair of layers in the case of a close-packed array of equal spheres (Durovič, 2006).

Let the multiplicity of the τ subgroup of a single layer be *N* and the multiplicity of the τ subgroup with continuation to the adjacent layer be *F*, then

$$Z = N/F \qquad (2.43)$$

where *Z* is the number of geometrically equivalent positions in the adjacent layer.

In the case of close packing of equal spheres, $Z = 2$ means that there are only two geometrically equivalent possibilities in the adjacent layer. This is already known as the B and C positions. Eq. 2.43 is known as the *NFZ* relationship in OD theory and is valid for all categories of OD structures with minor modifications (Merlino, 1997). Based on the *NFZ* relationship, useful inferences about the stacking of structures, which are based on the principle of stacking of equal spheres, can be made. Any such structure will show two

geometrically equivalent ways to achieve the next layer, resulting in two geometrically equivalent layer pairs. Geometric equivalence also maintains the energetic equivalence if all the interactions beyond the first-neighbor are neglected (this is a viable approximation provided the interaction energies are rapidly falling off beyond the first neighbor). In such a situation, two layer pairs are energetically equivalent. Therefore, the probability of the occurrence of both pairs is equal (Durovič, 2006). According to this explanation, it is possible to get an infinite number of polytypes as a result of the stacking of equal spheres. All these polytypes belong to a family called a polytype family.

A *polytype family* in OD theory is defined as a family containing all polytypes of a substance built on the same structural principle. According to this definition, all polytypes derived from the close packing of spheres belongs to one polytype family. An *OD groupoid family* consists of structures of various polytypic families, which may differ by their chemical composition, lattice dimensions, *etc*., but are built according to the same symmetry principle. For example, the polytypic families SiC, ZnS and AgI make one groupoid family (Durovič, 2006). Members of such a family differ only in their relative distribution of coincidence operations.

### 2.2.3 MDO polytypes

According to OD theory, a polytypic family can include an infinite number of periodic and non-periodic members. However, several of them occur more frequently. The OD theory nicely explains their predominance among others in terms of symmetry as well as in terms of energy. When a coincidence partial operation of the τ-type has a continuation in the structure, not only layer pairs, but also all triples, quadruples, …, *n*-tuples are geometrically equivalent, or at least, contain a minimum number of kinds of *n*-tuples (Durovič, 2006). These polytypes are called Maximum Degree of Order (MDO) polytypes in OD theory. For example, in the family of Wollastonite, only two types of triples are possible leading to two MDO structures (Ferraris, 2004). In the "stretched" triples, the direction of the layer-to-layer vectors does not change, whereas in the "bent" triples, the direction of these vectors alternates. These two situations are clearly shown in Fig. 2.3.

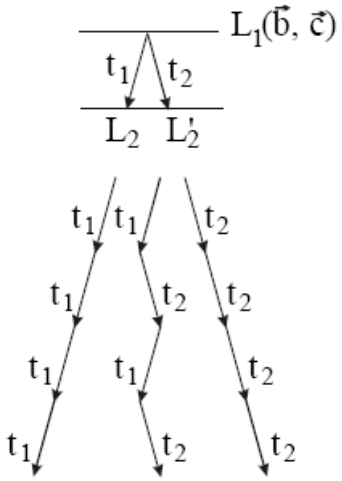


Figure 2.3: The arrangement of stretched and bent triples in a layer-stack which lead to MDO structures in the family of Wollastonite. t1 and t2 are two interlayer vectors pointing from the first layer (L1) to the two possible positions (L2 / L2') in the adjacent layer (Merlino, 1997).

MDO polytypes corresponding to stretched and bent triples are called MDO1 and MDO2, respectively. Note that the repeated application of just t1 or just t2 results in two separate MDO1 polytypes. Their relationship is that of twins with (100) being the twin plane. An alternating arrangement of t1 and t2 results in the MDO2 polytype.

The predominance of MDO structures over the other polytypes of the family is explained in the OD theory (Durovič, 2006).

"The general philosophy behind the MDO polytypes is simple: all interatomic bonding forces decrease rapidly with increasing distance. Therefore, the forces between atoms of adjacent layers are decisive for the build-up of a polytype. Since the pairs of adjacent layers remain geometrically equivalent in all polytypes of a given family, these polytypes are in the first approximation also energetically equivalent. However, if the longer-range interactions are also considered, then it becomes evident that layer triples such as ABA and ABC in close-packed structures are, in general, energetically non-equivalent because they are also geometrically non-equivalent. Even though these forces are much weaker than those between adjacent layers, they may not be negligible and, therefore, under given crystallization conditions, either one or the other kind of triples becomes energetically more favorable. It will occur again and again in the polytype thus formed, and not intermixed with the other kind. "

Polytype formation is very sensitive to the crystallization conditions. A small fluctuation of these conditions may favor an alternative, energetically closely similar possibility leading to

stacking faults and twinning in the structure. In the case of the close packing of equal spheres, there are only two MDO structures. Repeated arrangement of ABC triples results in the cubic close-packed polytype, while the repeated arrangement of ABA triples results in the hexagonal close-packed polytype. In addition to these two polytypes, an infinite number of other packing sequences (polytypes) are theoretically possible.

### 2.2.4 The groupoid symbol

It was mentioned earlier that POs form a groupoid. Strictly speaking, all the λ-symmetries form a layer group whereas σ-symmetries form a groupoid. Therefore the groupoid symbol consists of two parts (Merlino, 1997). In the first line, the layer group is presented. From the second line onwards, within braces, the groupoid of coincidence operations is presented. The stacking direction is indicated by writing the associated symmetry element within parentheses in both parts. As an example, the following groupoid symbol can be given.

| | |
|---|---|
| $P \quad m \quad m \quad (2)$ | λ-symmetry |
| $\{n_{s,2} \;\; n_{2,r} \;\; (2_2)\}$ | σ-symmetry |

The symmetry symbols of σ-POs are obtained as a generalization of the international space group symbols. The translational components along the stacking directions are given as normalized values of the interplanar distance, which is usually denoted by the vector followed by a subscript zero. In the above example, the coincidence operations have the following meanings,

$n_{s,2}$ – glide normal to $\boldsymbol{a}$ with a translation component $s\frac{\boldsymbol{b}}{2} + \boldsymbol{c}_0$;

$n_{2,r}$ – glide normal to $\boldsymbol{b}$ with a translation component $\boldsymbol{c}_0 + r\frac{\boldsymbol{a}}{2}$;

$2_2$ – two-fold screw rotation along $\boldsymbol{c}$ with a translation component $\boldsymbol{c}_0$.

Glide operations are denoted as $n_{r,s}$ where *r* and *s* are the translational components. Their vector positions are given as cyclic permutations of component vectors. For example, when the coincidence operations in a groupoid symbol include three general glides, their vectorial position should be referred to $\{n_{b,c} \; n_{c,a} \; n_{a,b}\}$ (Merlino, 1997). According to the above description, the groupoid symbol for the family of close-packed structures of equal spheres is

*P* (6/*m*) *m* *m*
{(3) *m* *1* }.

Given any layer, the next layer position is obtained at the end of the vector $\boldsymbol{t}_1 = \left(\frac{1}{3}\boldsymbol{a} + \frac{2}{3}\boldsymbol{b}\right) + \boldsymbol{c}_0$ or $\boldsymbol{t}_2 = -\left(\frac{1}{3}\boldsymbol{a} + \frac{2}{3}\boldsymbol{b}\right) + \boldsymbol{c}_0$. The repeated application of just $\boldsymbol{t}_1$ or just $\boldsymbol{t}_2$ results in two MDO polytypes. Each of these twinned structures corresponds to the cubic close-packed structure of equal spheres. An alternating arrangement of $\boldsymbol{t}_1$ and $\boldsymbol{t}_2$ results in the other MDO polytype that corresponds to the hexagonal close-packed structure of equal spheres.

### 2.2.5 Diffraction features of OD structures

A polytype family can contain an infinite number of polytypes. Therefore, it is possible to have an infinite number of average structures each corresponding to an individual polytype. In OD theory, the average structure is termed the superposition structure. It is obtained by superposing two or more identical copies of the same polytype translated by a superposition vector. Usually the superposition vector corresponds to a sub-multiple of a translation vector. The superposition structure is a totally fictitious construct of atoms in space.

A family structure of a polytype family is the structure having all the possible positions of each OD layer. Therefore, the family structure is common to all polytypes of the family (Dornberger-Schiff, 1964; Durovič, 1994). The symmetry of the family structure can be obtained by transforming all the local symmetry operations of a family groupoid into global symmetry operations of a space group (Fichtner, 1977). As is common to all polytypes of the family, the family reflections in the diffraction pattern are also common to all members. They are always sharp and characteristic. When indexed with respect to the basis vectors of any of the polytypes, family reflections show non-space group systematic absences. This is an indication of local symmetries in those member polytypes. Non-family reflections are typical of each polytype. They can be sharp for periodic polytypes but will be diffuse for non-periodic (disordered) polytypes. Note that a family structure exists only if the shifts between adjacent layers are rational.

The relationship between polytypes, family structure and their diffraction features can easily be shown with a simple hypothetical construct (Durovič, 2006), as given in Fig. 2.4.

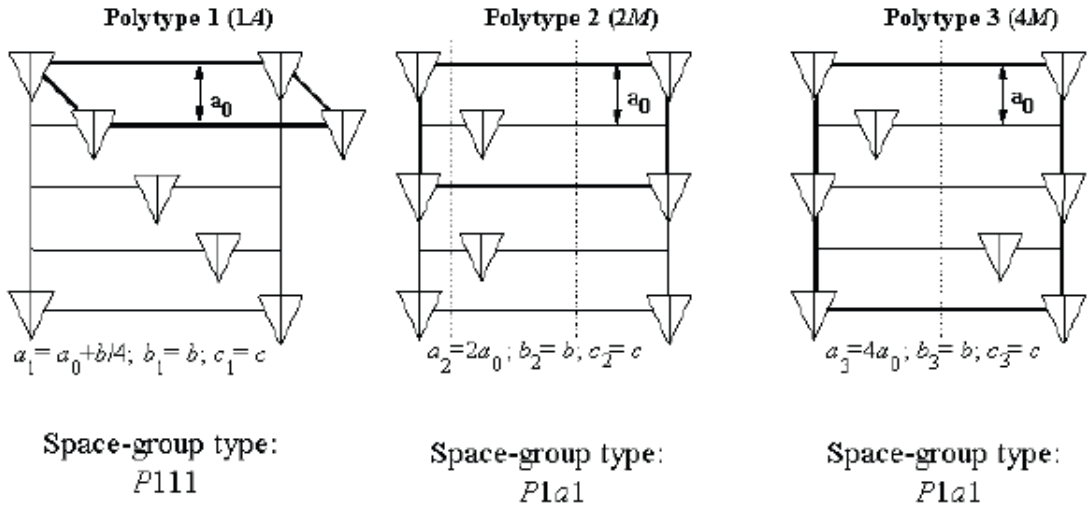


Figure 2.4: Schematic representation of three different polytypes belonging to the same polytype family. The stacking direction is **a** and is vertical. The horizontal direction is **b**. The layers are extending horizontally and coming out of the page. The atomic arrangement in the layers is represented by triangles. The distance between adjacent layers is $\mathbf{a}_0$. All structures are related to a common orthogonal four-layer cell with $\mathbf{a} = 4\mathbf{a}_0$ (Nespolo, 2009).

The three polytypes shown in Fig. 2.4 are built from stacking of equal layers with layer symmetry $P(1)m1$. Polytype 1 has the basis vectors $\boldsymbol{a}1 = \boldsymbol{a}_0 + \boldsymbol{b}/4$, $\boldsymbol{b}1 = \boldsymbol{b}$, $\boldsymbol{c}1 = \boldsymbol{c}$ and the space group is $P111$. The only coincidence operation is the translation with the translation vector of $\boldsymbol{a}_0 + \boldsymbol{b}/4$. Polytype 2 has the basis vectors $\boldsymbol{a}2 = 2\boldsymbol{a}_0$, $\boldsymbol{b}2 = \boldsymbol{b}$, $\boldsymbol{c}2 = \boldsymbol{c}$ and its space group is $P1a1$. It has an *a*-glide normal to $\boldsymbol{b}$ at y = 1/8 and 5/8. Polytype 3 has basis vectors $\boldsymbol{a}3 = 4\boldsymbol{a}_0$, $\boldsymbol{b}3 = \boldsymbol{b}$, $\boldsymbol{c}3 = \boldsymbol{c}$ and its space group is $P1a1$. In this case, there is an *a*-glide normal to $\boldsymbol{b}$ at y = 0 and ½. Polytypes 1 and 2 are MDO type polytypes as they have the repeated arrangement of stretched and bent triples, respectively. In other words, in Polytype 1, the translation has continuation, while in the Polytype 2, the *a*-glide has continuation. On the other hand, Polytype 3 does not have any coincidence operation that has a continuation. Therefore, polytype 3 is periodic in the $\boldsymbol{a}$-direction, it is not a MDO type. Instead, this polytype is built from both stretched and bent triples that alternate in the structure. This also indicates that Polytype 3 is a non-MDO type.

The family structure common to the above three polytypes (also to other possible polytypes) is shown in Fig. 2.5.

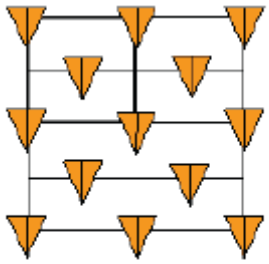

Figure 2.5: Graphical representation of the family structure of the polytypes 1, 2 and 3 described above (Nespolo, 2009).

The family structure has the basis vectors $\mathbf{A} = 2\boldsymbol{a}_0$, $\mathbf{B} = \boldsymbol{b}/2$, $\mathbf{C} = \boldsymbol{c}$ and its space group is $C1m1$. It is clear that any of the above three polytypes and also other possible polytypes can easily be derived from the family structure.

The diffraction patterns from the three polytypes sketched in Fig. 2.4 are shown in Fig. 2.6. Two types of diffraction spots are visible. Reflections shown in open circles are common to all three polytypes (also to other polytypes). They are the family reflections. Those reflections carry information about the family structure.

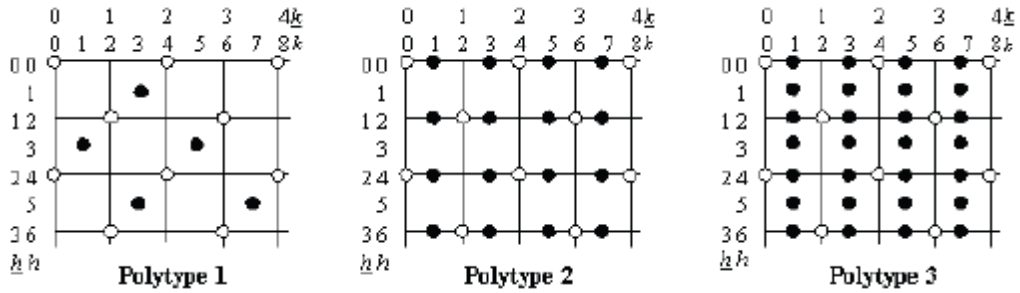


Figure 2.6: Schematic representation of diffraction patterns of polytypes 1, 2 and 3 from Fig. 2.4. Open circles are the family reflections. Filled circles indicate non-family reflections characteristic of individual polytypes (Nespolo, 2009).

As shown in Fig. 2.6, family reflections always occur when $K = 2k$. $K$ is the reciprocal lattice vector in the family structure, while $k$ is that of an individual polytype. This indicates that the superposition vector should be $\boldsymbol{b}/2$. Non-family reflections, shown by filled circles, occur when $K = 2k+1$. These reflections are characteristic of individual polytypes. When the family reflections are indexed in the cell of any polytype (i.e. $\boldsymbol{a} = 4\boldsymbol{a}_0$, $\boldsymbol{b} = \boldsymbol{b}$, $\boldsymbol{c} = \boldsymbol{c}$), systematic absences that cannot be explained by the space group symmetry arise. They are the result of local symmetry operations.

In general, it is not unusual to have the following peculiar features in the diffraction pattern from OD structures.

1. Family reflections.
2. The presence of sharp spots (always for family reflections) and diffuse streaks.
3. Non-space group systematic absences.
4. Diffraction symmetry higher than the point groupsymmetry (diffraction enhancement of symmetry).
5. Evidence for twinning, often polysynthetic twinning (polytypism).

By looking out for these features, one can easily identify the presence of OD structures.

### 2.2.6 Categories of OD structures

OD layers are two-dimensionally periodic slabs extending to infinity. However, the third dimension, which is normal to the layer plane, is not periodic. Depending on the type of layers from which the OD structure is built, there are two basic classes of OD structures. The first class is OD structures built up from equivalent layers. The other class is OD structures built up from more than one kind of layer.

#### 2.2.6.1 OD structures of equivalent layers

These layers are either all polar or all non-polar with respect to their stacking direction. This is a consequence of the equivalence of OD layers. The layer group of polar layers contains only λ-τ-POs. This causes the σ-POs to be either all τ-type or ρ-type. In the case of non-polar layers, the layer group contains both λ-τ-POs and λ-ρ-POs. This allows the σ-POs to be both τ- and ρ-types. Based on the distribution of symmetries in this type of OD layers, there exist three categories.

| Category | λ- character | σ- character |
|---|---|---|
| I | τ , ρ | τ , ρ |
| II | τ | τ |
| III | τ | ρ |

The layers in the first category are non-polar layers; they are denoted by the symmetric letter "A". This indicates that the layers can be transformed into themselves by λ-ρ-POs. The stacking sequence can be given as an array of "A" letters. The second and third categories have only polar layers and are denoted by either the letter "b" or the letter "d". In the second

category, a stacking sequence can be given as either “bbbbbbb…” or “dddddd….”. In the third category, the stacking sequence is given as a sequence of alternating letters “bdbdbd. The stacking sequences of these three categories are graphically shown in Fig. 2.7.

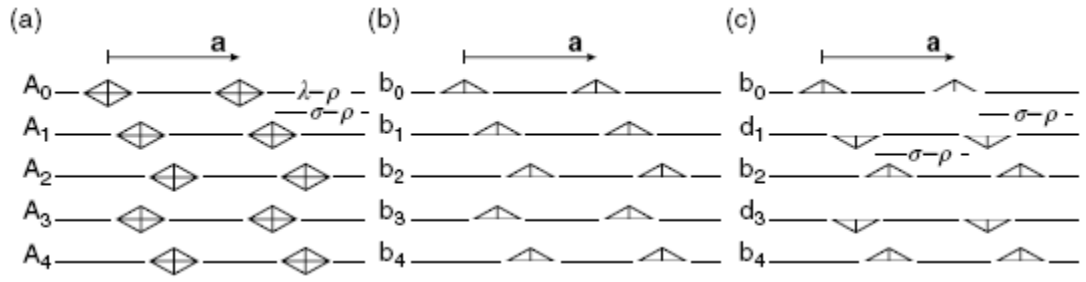


Figure 2.7: Schematic representation of three different categories of OD structures of equivalent layers. (a) category I; (b) category II and (c) category III. ( Durovič, 2006)

Fig. 2.7(a) shows the stacking of non-polar layers in category I. Both λ-(τ, ρ) symmetries and σ-(τ, ρ) symmetries are possible. The stacking sequence in category II is shown in Fig. 2.7(b). It is obvious that λ-τ POs in polar layers are translated into adjacent layers by σ-τ POs. In category III, a polar layer is transformed into its adjacent layer with opposite polarity by σ-ρ POs and is nicely shown in Fig. 2.7(c).

According to Ferraris (2008), OD theory on structures of equivalent layers is substantially complete up to date. The derivation of 400 possible OD groupoid families is complete and is extremely useful in deriving possible MDO structures. They are useful in understanding the complex diffraction patterns from OD structures. OD theory is a valuable tool for analyzing complex materials with many polytypes. It can provide valuable insights into the cause of disorder.

The compound being investigated in this thesis, Pigment Red 170, has a very peculiar diffraction pattern dominated by rods of diffuse scattering. The average structure models developed for this compound clearly show that this material has two obvious polytypes. In Chapter 3, the diffraction pattern from this material will be discussed in detail. Insights obtained from OD theory in this respect will be used in order to draw useful conclusions. In Chapter 4, the power of the OD theoretical approach in understanding the derived average models will be presented.

OD theory also covers the OD structures with more than one kind of layers. However, those categories will not be discussed here as such a discussion would be beyond the scope of this thesis.

## 2.3 Bibliography

Aebischer, A., Hostettler, M., Hauser, J., Krämer, K., Weber, T., Güdel, H. U. & Bürgi, H. -B. (2006). *Angew. Chem. Int. Ed*. **45**, 2802-2806.

Angel, R. J. (1986). *Z. Kristallogr*. **176**, 193-204.

Baumhauer, H. (1912). *Z. Kristallogr*. **50**, 33-39.

Baumhauer, H. (1915). *Z. Kristallogr*. **55**, 249-259.

Dornberger-Schiff, K. (1956). *Acta Cryst*. **9**, 593-601.

Dornberger-Schiff, K. & Grell-Niemann, H. (1961). *Acta Cryst*. **14**, 167-177.

Dornberger-Schiff, K. (1964). Grundzüge einer Theorie der OD-Strukturen aus Schichten. *Abhandlunge der deutschen Akademie der Wissenschaften zu Berlin. Klasse für Chemie, Geologie unf Biologie*, **3**, 1-107.

Dornberger-Schiff, K. (1966). *Lehrgang über OD-Strukturen*, Berlin: Akademie-Verlag.

Dornberger-Schiff, K. (1979). *Kristall und Tecknik*, **14**, 1027-1045.

Dornberger-Schiff, K. (1982). *Acta Cryst*. A**38**, 483-491.

Dunitz, J. D. (1995). *X-Ray Analysis and the Structure of Organic Molecules*, 2nd ed. p. 13. VCH: Basel.

Durovič, S. (2006). *International Tables for Crystallography*, Vol. C, 1st online ed., edited by E. Prince, ch. 9.2.2, pp 760-773. Chester: International Union of Crystallography.

Durovič, S. (1994). *Significance of superposition structures in the polytypism of phyllosilicates*. *Aperiodic '94, Proceedings of International Conference on Aperiodic Crystals*, edited by G. Chapuis & W. Paciorek, pp 595-599. World Scientific: Singapore/New Jersey/London/Hong Kong.

Ferraris, G., Makovicky, E. & Merlino, S. (2008). *Crystallography of Modular Materials*, New York: Oxford University Press.

Fichtner, K. (1977). *Beitr. Algebra Geom*. **6**, 71-79.

Fultz, B. & Howe, J. (2013). *Transmission Electron Microscopy and Diffractometry of Materials*, Heidelberg: Springer.

Grell, N. (1984). *Acta Cryst*. A**40**, 95-99.

Guinier, A. (1963). *X-Ray Diffraction*, San Francisco: W. H. Freeman & Company.

Merlino, S. (1997). *EMU Notes in Mineralogy*, Vol. 1, *Modular Aspects of Minerals*, pp 1-28. Budapest: Eötvös University Press.

Nespolo, M. (2009). *OD structures and ploytypes*, Chester: International Union of Crystallography, Commission on Mathematical and Theoretical Crystallography. (http://www.crystallography.fr/mathcryst/OD_structures.htm).

Nield, V. M. & Keen, D. A., (2001). *Diffuse Neutron Scattering from Crystalline Materials*, Oxford: Clarendon press Oxford.

Simonov, A., Weber, T. & Steurer, W. (2014). *J. Appl. Cryst*. **47**, 1146-1152.

Thompson, J. B. (1981). *Polytypism in complex crystals: contrast between mica and classical polytypes. Structure and bonding in Crystals II*, edited by M. O'Keefe, & A. Navrotsky, pp. 168-196. New York/London/Toronto/Sydney/San Francisco: Academic Press.

Weber, T. & Simonov, A. (2012). *Z. Kristallogra.* **227**, 238-247.

Welberry, T. R. (2004). *Diffuse X-ray Scattering and Models of Disorder*, Oxford: Oxford University Press.

# Diffraction pattern of a crystal of the β-phase of Pigment Red 170

The first part of this chapter briefly describes the chemistry and the uses of the compound Pigment Red 170 in general. It covers the known polymorphic forms and the crystal structures of some of them. The β-phase of Pigment Red 170; the subject compound of this thesis is introduced and the crystallization method is presented. The second part of this chapter includes a detailed analysis of the X-ray diffraction pattern coming from a crystal of the β-phase of Pigment Red 170. The first part of this section covers the coarse features while the second part covers the fine features of the diffraction pattern.

Most of the materials presented in this chapter have already been published (Warshamanage *et al*., 2014). Therefore, this chapter duplicates the published material to some extent.

## 3.1 Pigment Red 170

Azo pigments are an important class of chemicals because of their insolubility in most solvents and their remarkable colouristic properties. They are used in various applications, e.g. in paints and coatings, in the textile industry, in plastics, resins and inks (Herbst & Hunger, 2004). Pigment Red 170 (P.R.170) is a representative of this class (Fig. 3.1); it belongs to the Naphthol AS class ("Naphthol AS" = "Naphthol + Amid der Säure" = naphthoic acid amide).

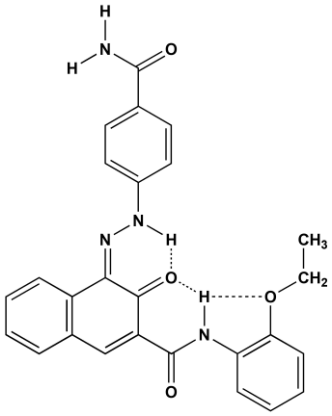


Figure 3.1: Pigment Red 170, $C_{26}H_{22}N_4O_4$

P.R.170 exists in three known crystalline phases: the nanocrystalline brown α-phase emerges from the synthesis. Its crystal structure was determined by X-ray powder diffraction *via* the

isotypic structure of a methylated derivative using lattice-energy minimization (Schmidt *et al.*, 2006). The molecules form a three-dimensional hydrogen-bonded network with the molecules arranged in a herringbone fashion and is shown in Fig. 3.2.

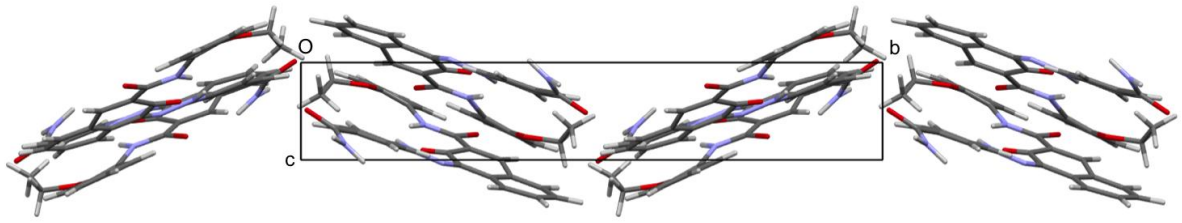


Figure 3.2: Packing diagram of α-P.R.170 when viewed down **a**. Horizontal axis is **b** and vertical axis is **c**.

The α-phase is metastable and transforms into the red β-phase upon heating in boiling water. Single-crystals of the β-phase are obtained by recrystallizing the pigment in high boiling solvents like N-methylpyrrolidone at about 473 K. The β-phase is used in industry for the colouration of plastics (Herbst & Hunger, 2004). When the α-phase is heated in water under pressure to 413 K for three hours, it transforms into the γ-phase, which is used in industry for lacquers and coatings, and has a bright red shade. In the γ-phase, the molecules form a two-dimensional hydrogen-bond network, resulting in wave-like layers as show in Fig. 3.3. The β-phase has a somewhat more bluish shade than the γ-phase.

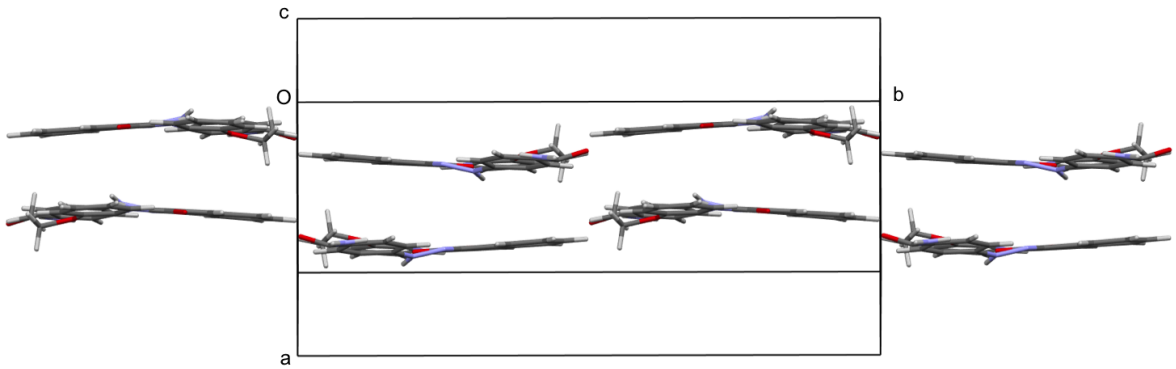


Figure 3.3: Packing diagram of γ-P.R.170 when viewed down [103]. Horizontal axis is **b** and two vertical axes are **a** and **c**.

### 3.1.1 Crystallization of the β-phase of Pigment Red 170

β-P.R.170 can be produced in large quantities and batches of up to 1 ton have been synthesized industrially. The synthesis has also been carried out on a laboratory scale. The obtained powder X-ray diffraction patterns from samples taken from both syntheses showed a very good match to those calculated from the average models. More details about crystallization can be found in Teteruk *et al*. (2014). Organic pigments by their very nature have extremely low solubility in most solvents. Therefore, growing any single crystals large enough for diffraction studies is very difficult, let alone obtaining then in significant quantities. The single crystal used in this study was obtained by dissolving a mixture of 1.0 g of the α-phase of P.R.170 and 0.2 g of the β-phase of P.R.170 in 15 ml boiling *N*-methyl-2-pyrrolidone at 476 K, and subsequent slow cooling to room temperature. The crystals were isolated by filtration, washed with ethanol and dried. Rapid cooling yields the same polymorph, but smaller crystals. The actual crystal used in this work was grown and kindly supplied by Martin Schmidt of Johann Wolfgang Goethe-Universität, Frankfurt, Germany.

### 3.1.2 X-ray data collection

A β-P.R.170 single crystal, brilliant red in colour, with approximate dimensions 0.30 × 0.15 × 0.15 mm was mounted on a loop and used for the data collection. The temperature was kept at 100 K. Three-dimensional X-ray data were collected in two stages. The first stage of the data collection was mainly focused on collecting an accurate set of Bragg data, which will be used in the average structure modelling. Accurate Bragg data with high redundancy was collected with a low-noise Titan CCD detector and four-circle KM6 diffractometer of beam line BM01A at the Swiss-Norwegian Beam Line of the ESRF. Two Bragg datasets were collected. The first dataset (Set 1) was collected at λ = 0.7083 Å with a crystal-detector distance of 100 mm, ω scan slicing of 1˚ per frame and up to 0.54 Å resolution. The exposure time per frame was chosen to provide an approximately constant dose and varied between 1 s and 8 s. The second Bragg dataset (Set 2) was collected at λ = 0.6973 Å with a crystal-detector distance of 120 mm, ω scan slicing of 0.5˚ per frame, exposure time per frame of 1 s and up to 0.81 Å resolution. All Bragg datasets were processed using the program CrysAlisPro (v.171.36.20) (Agilent Technologies, 2012).

The second stage of the data collection was mainly focused on collecting a highly accurate diffuse scattering dataset, which will be used for the local structure modelling. For his purpose, the first diffuse dataset (Set 3) was collected at the same beam line but with a MAR345 image plate at λ = 0.7083 Å with a crystal-detector distance of 300 mm, ω scan

slicing of 0.5˚ per frame and up to 0.84 Å resolution. The exposure time was chosen to be 4 s per frame. The last dataset (Set 4) was collected at the same beam line with a PILATUS 2M detector at λ = 0.6895 Å with a crystal-detector distance 444 mm, ω scan slicing of 0.1˚ per frame and up to 1.02 Å resolution. In this case the exposure time was chosen to be 0.25 s per frame.

The details of the diffraction pattern will be scrutinized using the Set 2 dataset with finer slicing. This chapter will cover the observed single-crystal diffraction pattern of β-P.R.170, its unusual features and possible interpretations of them. Set 1 dataset with its much higher resolution was used for modelling the average structure and is discussed in chapter 4. A detailed description on detectors for diffuse data collection and preparation of diffuse data for local structure modelling is given in chapter 5.

## 3.2 Diffraction pattern

The diffraction pattern consists of Bragg reflections and rods of strong diffuse scattering. The latter run in one direction only and pass through Bragg reflections, *i.e.* there are no rows of Bragg reflections that are not coincident with at least some diffuse scattering. The diffuse features that can readily and clearly be seen are described in section 3.2.1 while those which need more detailed analysis are described in section 3.2.2.

The Laue symmetry of the total diffraction pattern is 2/*m* and is conveniently described in a monoclinic unit cell with parameters **a** = 14.4285(5), **b** = 24.7715(5), **c** = 24.9914(8) Å, β = 109.738(3)˚ and diffuse streaks running parallel to **a***. The derivation of possible unit cells from the Bragg reflections, and the difficulties associated therewith, will be described in detail in chapter 4.

### 3.2.1 Coarse features

The reciprocal lattice layers *h*n*l* (n = 0 to 23 and is integer), *hk*0 and 0*kl* clearly show that the rods of diffuse scattering are always parallel to **a***. With increasing n the diffuse features in successive *h*n*l* layers cycle through a pattern with a repeat of 6.3**b***. A cycle starts with a layer showing what looks like sharp Bragg reflections (e.g. *h*0*l*) and quite weak and short diffuse lines. It progressively moves through weakening Bragg and strengthening diffuse features to a maximum of strong diffuse rods with barely discernable Bragg reflections (e.g. *h*3*l*), then the trend reverses and returns to the sharp Bragg/weak diffuse pattern (e.g. *h*6*l*) before the cycle starts again. The layers can be divided into three basic classes depending on where in the cycle each layer is. The *Bragg-like layers* (*type A*) clearly show the Bragg lattice [e.g. *h*0*l*,

*h*1*l*, *h*6*l*, *h*7*l*, *h*13*l*, *h*19*l* and *h*20*l*. Fig. 3.4(*a*)]. On the *Mixed type layers* (*type B*) Bragg like reflections can be seen throughout the reciprocal layer; however reflections at higher angles are smeared out along **a*** sometimes forming continuous lines compared to lower angle reflections. Typical examples are *h*2*l* [Fig. 3.4(*b*)], *h*5*l*, *h*8*l*, *h*9*l*, *h*11*l*, *h*12*l* and *h*14*l*. Bragg reflections on the *layers dominated by diffuse scattering* [*type C*, *e.g. h*3*l*, Fig. 3.4(*c*), *h*4*l*, *h*10*l*, h15l, *h*16*l*, *h*17*l* and *h*23*l*] are superimposed by strong diffuse streaks. Identifying the Bragg reflections is difficult.

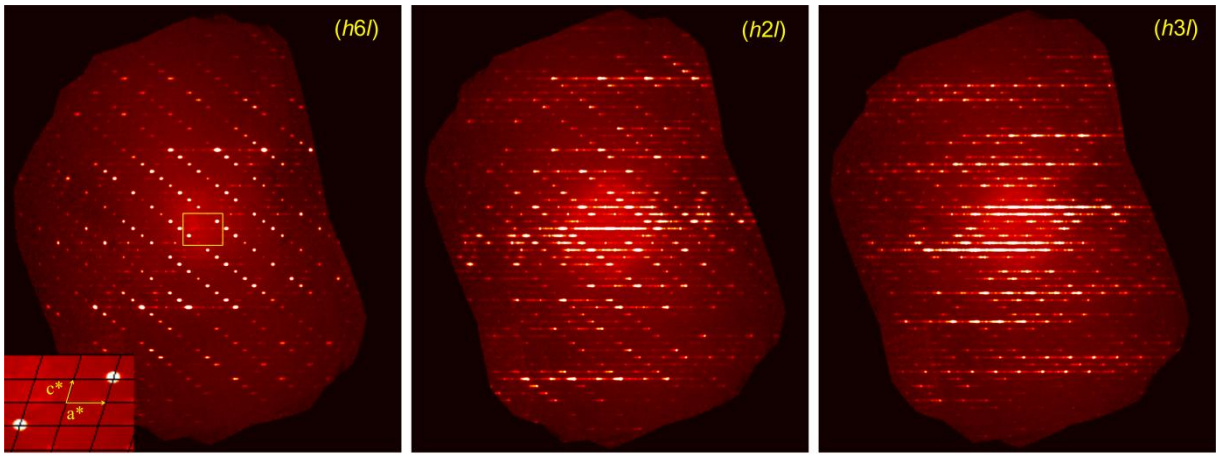


Figure 3.4: Reconstructions of reciprocal lattice layers showing (*a*) a *type A* layer (*h*6*l*: reciprocal unit cell axes are shown in the inset); (*b*) a *type B* layer (*h*2*l*); (*c*) a *type C* layer (*h*3*l*).

In *type A* and *type B* layers, the majority of strong reflections fall onto rows which run parallel to [10-1] with a spacing in the **a*** direction of 4**a***. In the range $-2 \leq n \leq 2$ these reflection rows cut through the **a*** axis at $h = 4m$ (m is an integer) in *hnl* layers with n even (-2, 0, 2), while they cut **a*** at $h = 4m + 2$ in layers with n odd (-1, 1). In the range $5 \leq n \leq 8$ the situation is opposite: the case $h = 4m$ is associated with n odd, the one with $h = 4m + 2$ is associated with n even. The change-over takes place at the *type C* layers, where these rows cannot be discerned easily. This pattern also repeats with the periodicity of n ~ 6.3.

### 3.2.2 Fine features

The intensity profiles along **a*** in the neighbourhood of the Bragg reflections differ in the three types of layers. As shown in Fig. 3.5, which is representative of reflections with low *l*, the A-type reflection 660 appears to be symmetric, relatively sharp and hardly affected by diffuse scattering. The B-type reflection 620 is comparably sharp, but sits on a structured diffuse signal. Separation of the Bragg signals from the diffuse signals and the extraction of accurate B-type Bragg intensities are difficult.

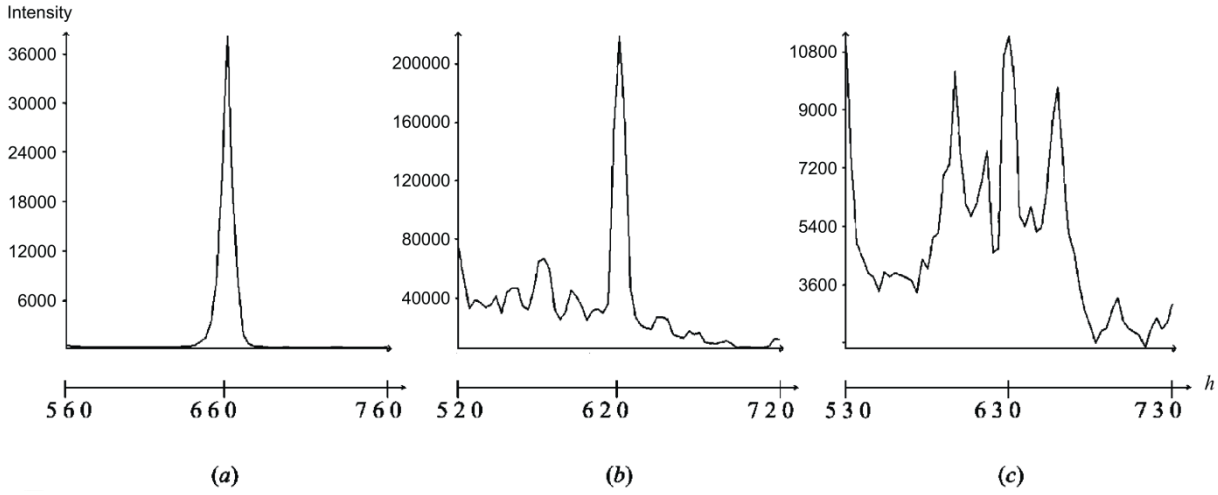


Figure 3.5: Representative intensity profiles along increasing *h.* (*a*) the *type* A reflection 660; (*b*) the *type* B reflection 620; (*c*) the *type* C reflection 630.

The C-type reflection 630 appears broader than the A- and B-type reflections and is surrounded by signals of similar magnitude. It must probably be considered as a superposition of a Bragg reflection and a comparatively intense diffuse signal, as is indicated by the diffuse maxima at non-integer *h*-values. In this situation, determination of a reliable Bragg intensity appears hopeless. Fig. 3.6 depicts a similar analysis of reflections with high *l* where the B- and C-type high-angle reflections are elongated asymmetrically along the diffuse lines in only one direction; the features of the lines chosen in Fig. 3.6 always extend to the side of more positive *h*, the direction of higher diffraction angles [Fig. 3.6 (*b*) and (*c*)]. The maxima of the profiles appear slightly displaced from integer reciprocal lattice positions. It is difficult to say whether this feature is intrinsic to this diffraction pattern or due to the orientation matrix being biased to some extent by the diffuse signals. Again, the Bragg signals are affected by the superimposed diffuse scattering.

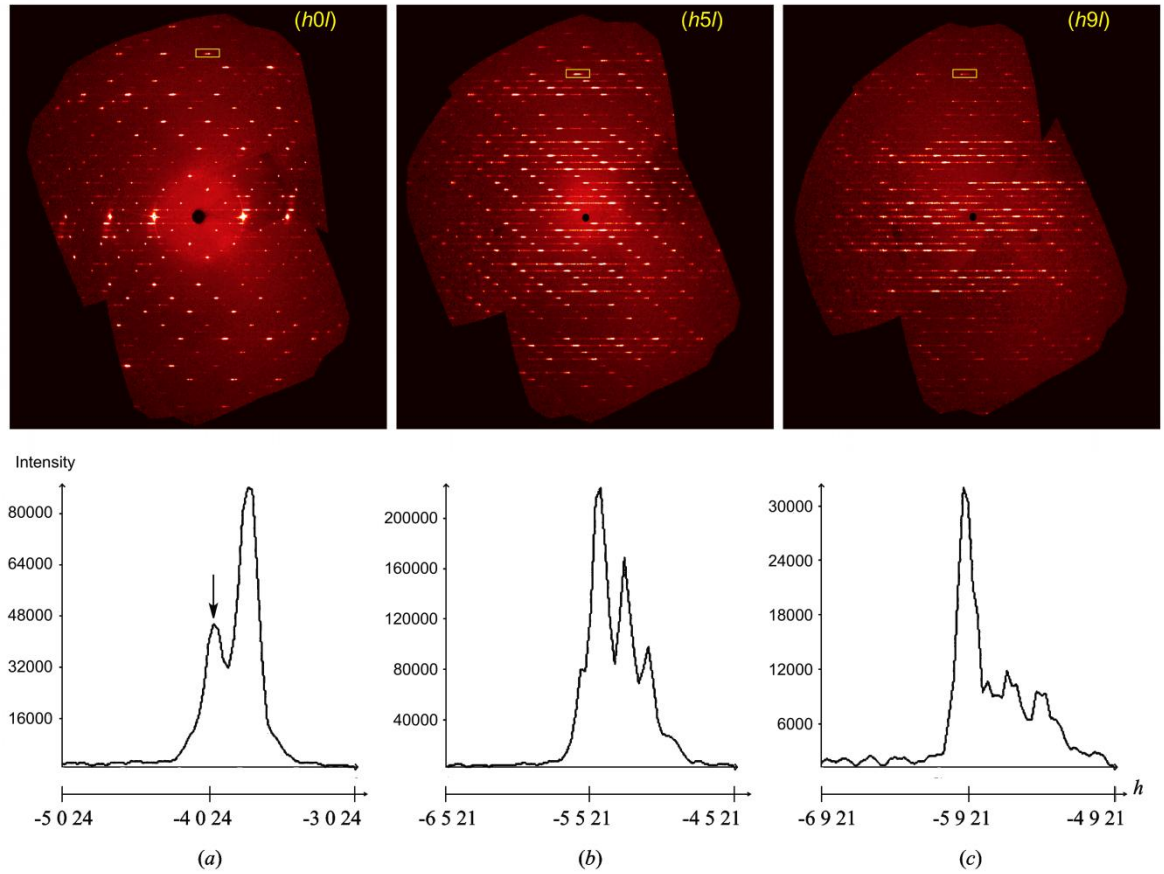


Figure 3.6: Reconstructions of different types of reciprocal lattice layers and representative intensity profiles along increasing *h* of the region taken from the yellow rectangles. (*a*) *type* A *Bragg-like* layer *h*0*l* with a profile around -4 0 24.The position of the Bragg peak is arrowed; (*b*) *Mixed-type* B layer *h*5*l* with a profile around -5 5 21; (*c*) *Diffuse-type* C layer *h*9*l* with a profile around -5 9 21.

Even in the A-type layers, higher angle Bragg reflections are poorly resolved. Unlike B- and C-type higher angle reflections, the Bragg intensity is sometimes smaller than the neighbouring diffuse maximum [Fig. 3.6 (*a*)]. It might be argued that such split peak features are the result of a poorly determined orientation matrix or a crystal that is not single. However, all attempts to find a second Bragg lattice using the CrysAlisPro multi-crystal/twin indexing routines (Agilent Technologies, 2012) were unsuccessful. Some of the features described in this section have also been identified in the raw data frames. Together these observations confirm that the observed diffraction features are most likely a signature of the disorder inherent to this material.

Given above unusual features of the diffraction pattern, any reliable indexation of peaks, the unit cell determination and the extraction of accurate Bragg intensities are at a great

challenge. In the first part of the next chapter, the attempts taken to answer these issues will be discussed.

## 3.3 Bibliography

Agilent Technologies (2012). *CrysAlisPro,* Version 1.171.36.20. Agilent Technologies, Yarnton, Oxfordshire, England.

Herbst, W. & Hunger, K. (2004). *Industrial Organic Pigments: Production, Properties, Applications*, 3rd ed. Weinheim: Wiley-VCH.

Schmidt, M. U., Hofmann, D. W. M., Buchsbaum, C. & Metz, H. J. (2006). *Angew. Chem*. **118**, 1335-1340, *Angew. Chem. Int. Ed.* 45, 1313-1317.

Teteruk, J. L., Glinnemann, J., Gorelik, T. E., Linden, A. & Schmidt, M. U. (2014). *Acta Cryst*. B**70**, 296-305.

Warshamanage, R., Linden, A., Schmidt, M. U. & Bürgi, H. -B. (2014). *Acta Cryst*. B**70**, 283-295.

# The average structure of β-Pigment Red 170

## 4.1 Introduction to the average structure of β-P.R.170

The previous chapter described the observed total diffraction pattern of β-P.R.170 in some detail. In this chapter, various challenges faced during the data processing are discussed. Possible remedies where applicable are also presented. A substantial part of the chapter is devoted to the description of the average structure models of the material. Towards the end, the average models are described in the context of OD structures. Lastly, the reciprocal space description of those models is presented.

Most of the materials presented in this chapter have already been published (Warshamanage *et al*, 2014). Therefore, this chapter duplicated the published material to a large extent.

### 4.1.1 Indexing and unit cell determination

Since the Bragg reflection profiles are affected by rods of diffuse scattering, unit cell determination, reflection indexation and determination of Bragg reflection intensities are non-trivial. In the absence of unaffected or minimally affected Bragg reflections at high scattering angles, it is very difficult to determine an unbiased orientation matrix. To deal with this difficulty, a series of unit cell determinations was carried out. In the first step of each attempt, a peak list was generated by choosing a minimum intensity threshold which eliminated as many diffuse signals as possible. The software used in this purpose is CrysAlisPro (v.171.36.20) (Agilent Technologies 2012). However, it is clear from the diffraction pattern (see Figs. 3.2 and 3.4) that the intensities of some diffuse signals are similar in magnitude to Bragg intensities. Therefore, the inclusion of some diffuse signals in the peak list is unavoidable and leads to an ambiguity in the determination of the Bravais lattice and other systematic absences.

Regardless of the peak hunting threshold value, monoclinic unit cell one (UC1) is found very frequently (Table 4.1), while unit cell two (UC2) is found only with lower thresholds. UC2 can be derived from UC1 by doubling the **a** axis and interchanging the **a** and **c** axes. In these

standard unit cell settings, the diffuse streaks are not parallel to any of the reciprocal cell axes. In order to simplify simulations of the diffuse scattering and the description of the disordered layer stacking, it is more convenient to choose unit cells which have a direct axis parallel to the stacking direction and the corresponding reciprocal axis parallel to the direction of the diffuse streaks. Therefore, for all subsequent work, the unit cells in Table 4.1 were transformed to these more convenient non-standard settings (TC1 and TC2) by using the matrix operations [0 0 -1 / 0 1 0 / 2 0 1] and [-1 0 0 / 0 -1 0 / 1 0 1] on UC1 and UC2, respectively, as shown in Fig. 4.1. The transformed unit cell parameters are given in Table 4.1.

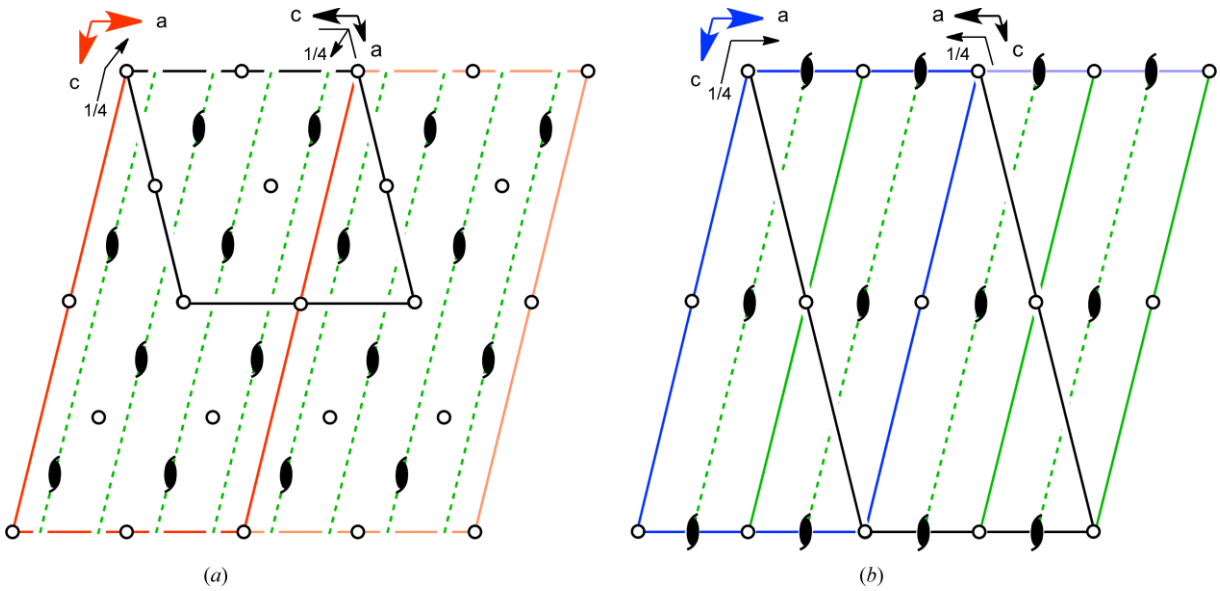


Figure 4.1: (*a*) Transformation of UC1 (black) to TC1 (red); transformation matrix, **T** = [0 0 -1 / 0 1 0 / 2 0 1]. (*b*) Transformation of UC2 (black) to TC2 (blue); transformation matrix, **T** = [-1 0 0 / 0 -1 0 / 1 0 1]. Solid and dashed green lines indicate the positions of molecular layers parallel to the b,c-plane in all unit cells. TC1 and TC2 have the same metric parameters, but the structural models in them are quite different.

Table 4.1: Lattice constants of the unit cells UC1, UC2, TC1 and TC2 after constraining to monoclinic symmetry. UC1 and UC2 correspond with the standard settings as produced by the software. TC1 and TC2 are the transformed versions of UC1 and UC2 with the transformation matrices given in Fig. 4.1.

| Cell | No. of reflections | *a, b, c* (Å) | $\beta$ (°) | Space group |
|---|---|---|---|---|
| UC1 | 46089 | 12.1367(2), 24.7715(5), 14.4285(5) | 104.283(3) | $P2_1/n$ |
| UC2 | 49256 | 14.4270(4), 24.7749(3), 24.2774(4) | 104.213(2) | $P2_1/a$ |
| TC1 | | 14.4285(5), 24.7715(5), 24.9914(8) | 109.738(3) | $B2_1/g$ |
| TC2 | | 14.4270(4), 24.7749(3), 25.0108(6) | 109.786(2) | $P2_1/a$ |

### 4.1.2 Extraction of the Bragg intensities

As described in detail in §3.2, the Bragg reflections are superimposed to varying degrees by the diffuse signals implying great difficulties in the extraction of reliable Bragg intensities. One way to cope with this problem to some extent is to fit the reflection profiles to a calculated profile. A reflection profile shape is given by the three mosaic parameters (e1, e2 and e3) where e3 is defined to be perpendicular to the detector plane, whereas e1 and e2 lie in the detector plane. For a normal, ordered crystal, e1 and e2 are usually a few tenths of a degree, while e3 depends mostly on the slicing angle. In the current study, e2 tends to be smaller than the e1 and e3 values and to show a smaller standard deviation. The e3 value varies greatly and may be as large as 2.6 degrees, as expected from the reflection profiles in Fig. 3.4. The e1 values also vary greatly. This unusual behaviour is a consequence of the strong diffuse streaks passing through the Bragg reflections. Using one common fitting function will therefore not suffice to suitably represent the majority of reflections. However, the software available to us does not have sufficient flexibility to circumvent this problem.

Mask size is an important parameter in the extraction of intensities. It determines the area on the detector integrated for each reflection. With the current data, if a large mask size is chosen, then a part of the diffuse streak near the Bragg reflection is also integrated leading to an over-estimated Bragg intensity. In fact, regardless of mask size, if some diffuse intensity lies directly under the Bragg peak position, the intensity will be over-estimated. On the other hand, if a small mask size is chosen, or the diffuse signal extends well away from the Bragg peak position, the background may include a significant amount of diffuse scattering and is over-estimated, thereby leading to a reflection intensity that is too low. The extent to which this affects each reflection is highly variable. Therefore, an optimal mask size cannot readily be derived in the present case. A series of integrations was carried out using different mask

sizes and for each case *R*-internal ($R_{int}$) was calculated. It was finally decided that the best mask size for the purpose was that which gives the lowest $R_{int}$ and this mask size was the program default. However, it is important to keep in mind that this mask size represents the best one can do given the diffraction properties of the sample and the limitations of the software. In the final step of the data extraction, an empirical absorption correction was applied using the spherical harmonics procedure in CrsyAlisPro and the frames were scaled to check whether the crystal has been centred properly in the synchrotron beam during the measurement. No anomalies were detected in the scaling output.

### 4.1.3 Space group determination

The integrated reflection intensities in each of the transformed unit cells were used for all subsequent work. Statistical analyses of intensities and space group determination were carried out using the program WinGX (Farrugia, 1999). A Wilson plot and Cumulative Probability Distribution (CPD) curves were constructed first. CPD curves are a rough, but often good indication for the presence or absence of a center of symmetry. In the current study, the experimental probability distribution curve does not match with any of the three idealized curves, as shown in Fig. 4.2. It is significantly above the hypercentric distribution suggesting the presence of non-crystallographic as well as crystallographic inversion symmetry. However, this result has to be treated cautiously, given the questionable quality of the Bragg intensities.

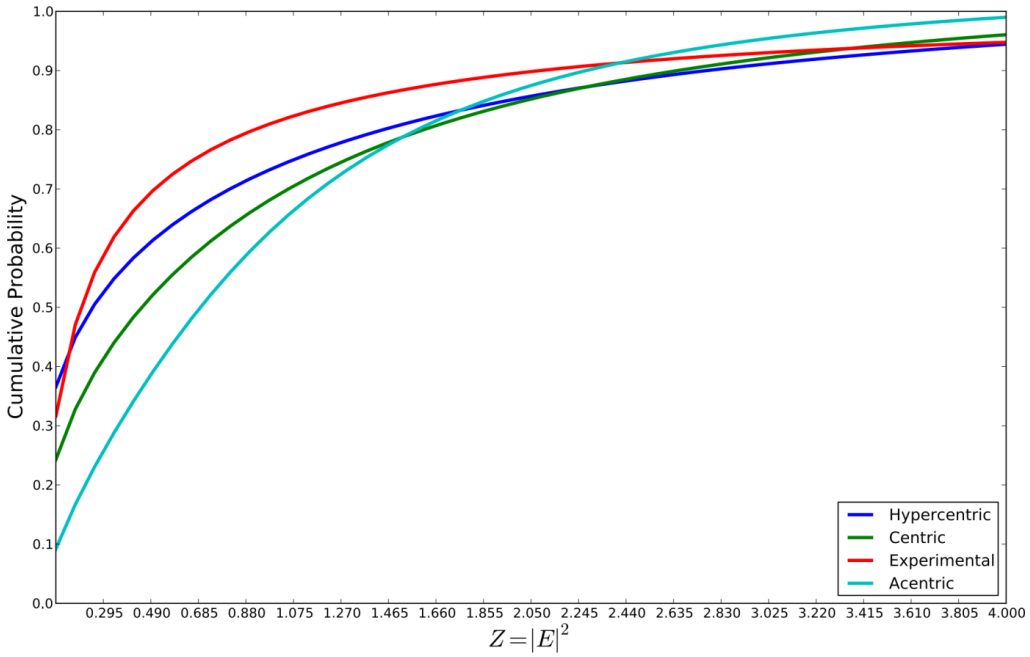


Figure 4.2: Cumulative probability distribution of $E^2$ in TC1 compared to several theoretical distributions.

The extinction conditions for the general reflections in TC1 indicate a *B*-centered lattice; those for the axial reflections 0*k*0 indicate the presence of a $2_1$ axis parallel to **b**, while the zonal reflection conditions for the *h*0*l* layer show the presence of an unconventional glide operation perpendicular to **b** with glide component (**a**-**c**)/4. In the following, this operation is depicted by the general glide symbol *g* (Fischer & Koch, 1992). Therefore, the space group was deduced to be $B2_1/g$, a non-standard, *B*-centered variant of $P2_1/c$, with $Z = 16$, $Z' = 2$. The list of symmetry operations defining this space group are given in Table 4.2 and are depicted graphically in Fig. 4.1. Note, however, that about 4% of the reflections that should be systematically absent under the *g*-glide operation (*h*0*l*, $h\text{-}l = 4n\pm1$) have significant intensities. An analogous analysis of reflections for the transformed unit cell TC2 resulted in space group $P2_1/a$, $Z = 16$, $Z' = 4$. Here, as much as ~10% of the reflections that should be systematically absent under the *a*-glide condition have significant intensities. These systematic absence violations could result from interference by the diffuse scattering signals, or be an indication that the space group symmetries are questionable. With the tools available, it is difficult, if not impossible, to distinguish these alternatives.

### 4.1.4 Attempts at structure solution and refinement

All attempts at structure solution showed the layered motif in Fig. 4.3 to be the building unit of the β-P.R.170 crystal structure. This motif is found in the γ polymorphic form (Schmidt *et at*., 2006). Its layer symmetry is approximately $p\ 1\ 2_1/c\ 1$, which is an alternative setting of layer group #17 (Kopský & Litvin, 2010). Depending on the model (see below), some of these symmetry operations become crystallographic, the rest are non-crystallographic.

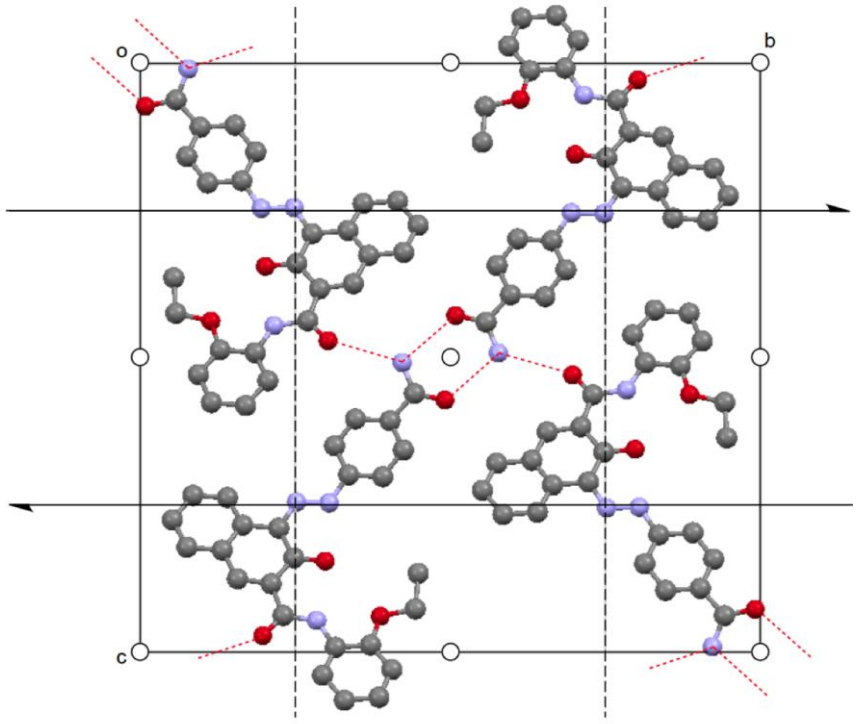


Figure 4.3: Idealized layer building block of β-P.R.170 showing *p* 1 $2_1$/*c* 1 symmetry. Intermolecular hydrogen bonds are shown as red-dashed lines.

*Model 1*

The structural model developed in the space group $B2_1/g$ will be referred to as model 1. It was found in several steps by the application of direct methods and difference Fourier syntheses (Sheldrick, 2008). The asymmetric unit (ASU) contains two nearly planar P.R.170 molecules located in the **b**,**c**-plane at $x$ = ⅛ (Fig. 4.1*a*). Initially they were assumed to have full occupation (i.e. to be ordered). This model which included hydrogen atoms at idealized positions, was refined using SHELXL97 (Sheldrick, 2008) to an $R1$ of ~0.17. Difference-Fourier (DF) maps obtained from this model showed the first 50 difference density peaks to be significant compared to the r.m.s. deviation from the mean residual density. Almost all the largest difference density peaks could be interpreted in terms of two additional P.R.170 molecules shifted relative to the ASU found previously by the vector -0.158**b**. The geometry of each of the new molecules was tightly restrained to be similar to the geometry of the existing molecules (using the instruction SAME in SHELXL97 with a standard uncertainty of 0.005 Å). The occupancies of the new and original molecules were constrained to add to 1. After several full-matrix least squares refinement cycles (all non-hydrogen atoms anisotropic, hydrogen atoms isotropic and combined to ride on their parent atoms), $R1$ improved to ~0.12

and the principal mean square atomic displacement parameters (ADPs) of the major components became more reasonable, whereas those of the minor components seemed unreasonably large. The latter were then constrained to be identical with the corresponding ADPs of the major components (using the EADP instruction in SHELXL97). This model refined to an *R*1 of 0.12 with occupancies of 0.9294 (7) and 0.0706 (7) for the major and minor components, respectively, and reasonable ADPs. The DF maps synthesized from the final model (Fig. 4.4) did not show any electron density peaks that could readily be interpreted as representing the positions of additional molecules. However, this observation should be treated cautiously given the uncertain quality of the integrated intensities, as described earlier. The displacement of 0.158**b** between the major and minor positions in the layer is responsible for the periodicity of 6.33**b*** (= 1/0.158**b**) relating the A-, B- and C-type reciprocal lattice layers described in §3.2.1.

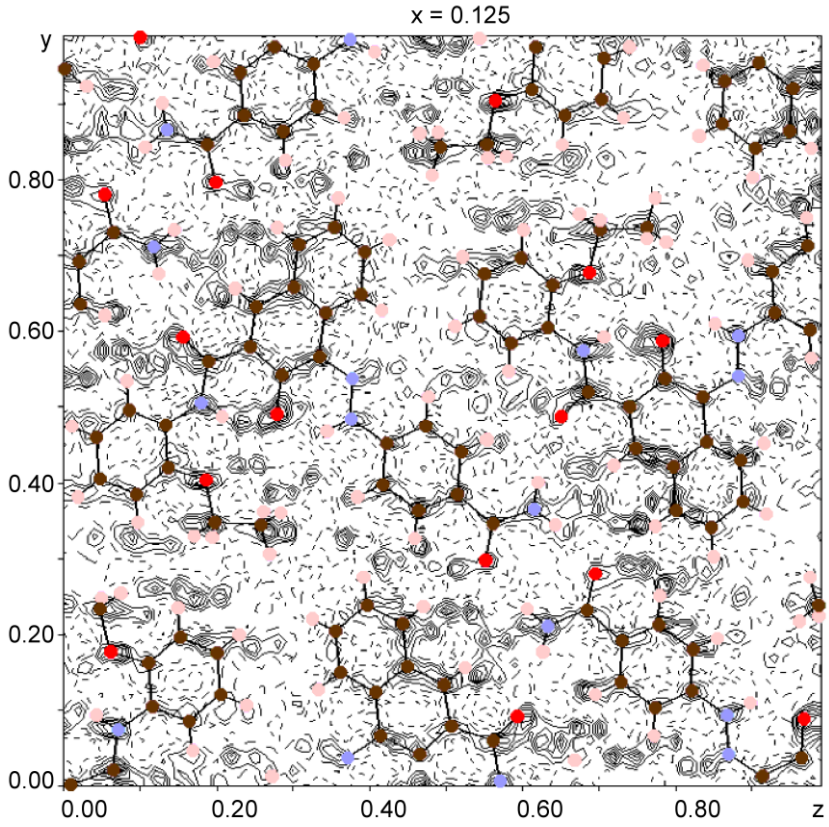


Figure 4.4: Difference electron density map at $x$ = 0.125 of model 1 in $B2_1/g$. Positive and negative contour levels are shown by solid and dashed lines respectively, step 0.2 e/Å$^3$. Only the molecules with the occupation factor 0.9294(7) are shown. Minor molecules can be located by translating major molecules with the vector [0, -0.158, 0].

This model resembles the structure obtained by Christie and co-workers (Christie, 2002; Christie *et al.*, 2014). They obtained single crystals of β-P.R.170 by recrystallisation from nitrobenzene. They measured the X-ray diffraction pattern at 160 K using a point detector. The structure was solved in the monoclinic unit cell UC1 with dimensions $a$ = 12.156(5), $b$ = 24.713(5), $c$ = 14.464(5) Å, $\beta$ = 104.63°(5), space group $P2_1/n$, $Z$ = 8 and $Z'$ = 2. The structure of Christie corresponds to our model 1 if only the major positions are considered.

*Model 2*

The structural model 2 in TC2 was developed with space group $P2_1/a$, analogously to the development of model 1. There are four molecules in the ASU. Two ordered molecules are located in a layer parallel to the **b**,**c**-plane at $x$ = 0 (Fig. 4.1*b*). The other two independent molecules are located in the layer at $x$ = ¼ parallel to the first layer and are disordered over two sites related by the vector 0.158**b**. The disorder is similar to that in model 1, although this time the major and minor components have occupancies of 0.6478 (7) and 0.3522 (7) respectively. The refinement was carried out in an analogous fashion to that for model 1, including the use of geometric restraints and ADP constraints. At convergence, $R1$ was 0.19.

DF maps from the ordered layer in this model showed difference density peaks greater than 2 e/Å$^3$, which suggest the presence of additional molecules, thus indicating that the ordered layer might actually be disordered. All attempts to include the additional molecules in a refinement were unsuccessful. This observation and the difficulties in separating Bragg from diffuse scattering led us to question the validity of the chosen space group symmetries and to pursue the analysis of both models further (§4.3).

## 4.2 Description of the average structures

The P.R.170 molecules exhibit the usual hydrazone-tautomeric form (-NH-N=C), which is also observed in all other Naphthol AS pigments (Kobelt *et al.*, 1972, 1974; Whitaker, 1978; Paulus, 1982; Chang *et al.*, 2003, 2009; Schmidt *et al.*, 2006). In most textbooks, P.R.170 and other Naphthol AS pigments are still drawn in the azo-tautomeric form (-N=N-C). The H atom of the CONH moiety forms a bifurcated intramolecular hydrogen bond to the oxygen atom of the ethoxy group and of the naphthoquinone system, as drawn in Fig. 3.1. The molecules are not perfectly planar. The mean deviation of the atoms from the plane is ~0.65Å.

The crystal structure of β-P.R.170 is composed of molecular layers. Within these layers, molecules interact through a network of two types of hydrogen bonds. Pairs of molecules are connected by hydrogen bonds between the $CONH_2$ groups across the layer inversion centers

as shown in Fig. 4.3. Additional intermolecular hydrogen bonds can be found between the second hydrogen atom of the $CONH_2$ moiety and the O atom of the CONH group in a neighbouring molecule. The centrosymmetric pairs are arranged into a close-packed pattern by two *c*-glide operations perpendicular to **b** and $2_1$ screw rotations parallel to **b**.

The layers are parallel to the **b**,**c**-plane and stack along the **a** axis in both models; however, their placement along the stacking axis is different in the two models. As mentioned in §4.1.1, the layers show approximate *p* 1 $2_1$/*c* 1 layer symmetry. Only some of the layer symmetry operations appear as crystallographic symmetry operations in the two models, with a different subset being crystallographic in each case, as described in the next two subsections.

### 4.2.1 Model 1

In model 1, the **b**,**c**-planes at *x* = ⅛, ⅜, ⅝, *etc*. are occupied with a superposition of two geometrically very similar molecular layers shifted relative to one another by 0.158**b**, as shown in Fig. 4.5*a*, and with major and minor occupations of M = 0.9294 (7) and m = 0.0706 (7), respectively. The space group $B2_1/g$ (Table 4.2) implies that these layers are symmetry equivalent.

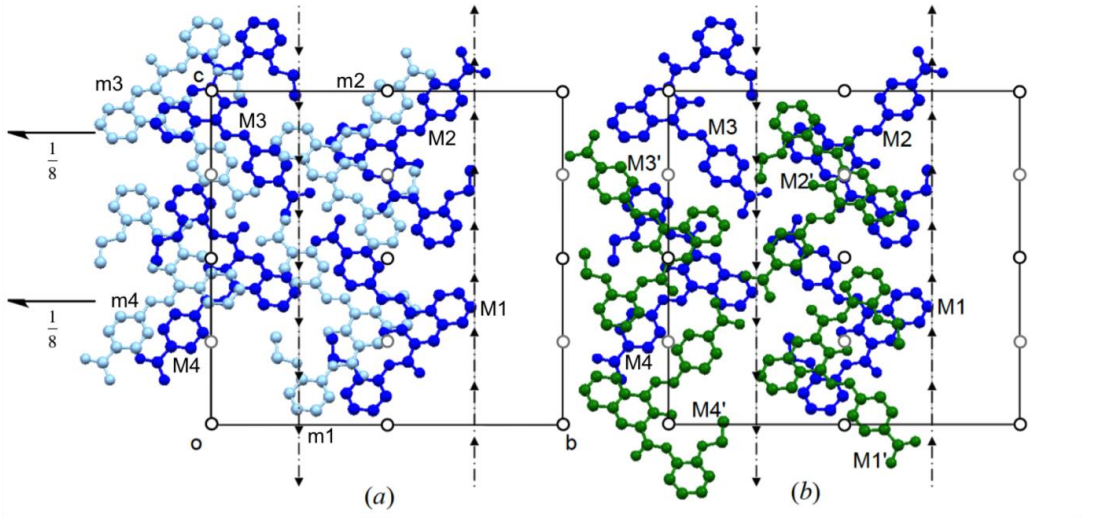


Figure 4.5: (*a*) The molecular layer at *x* = ⅛ in model 1 viewed down **a** showing the major (M, dark blue) and minor (m, light blue) positions related by -0.158**b**. (*b*) The two adjacent layers, at *x* = ⅛ (blue molecules, M1 – M4) and *x* = ⅜ (green molecules, M1' – M4') in model 1 viewed down **a**. Only the major components and the symmetry relationships between them are shown. In this figure only the first layer (*x* = ⅛) $2_1$ axes are shown. Black circles represent inversion centers at *x* = 0 and ½ while grey circles are inversion centers at *x* = ¼ and ¾. The *g*-glide planes at *x*, ¼, *z* and *x*, ¾, *z* are also shown.

### 4.2.2 Model 2

In model 2, the layer stacks are built from two symmetry-independent molecular layers. One type of layer is located at $x$ = 0 and ½ while the other independent type is found at $x$ = ¼ and ¾. The layer at $x$ = 0 is ordered with molecules showing full occupation (F), whereas the layers at $x$ = ¼ and ¾ are disordered over two positions again related by the shift vector 0.158**b**; occupation factors for the major (P) and minor (p) positions are 0.6478(7) and 0.3522(7), respectively. In the layer at $x$ = 0 only the inversion centers of the layer group $p$ 1 $2_1/c$ 1 are crystallographic symmetries; in the layer at $x$ = ¼ only the $2_1$ operations are crystallographic (see Figs. 4.1*b* and 4.6).

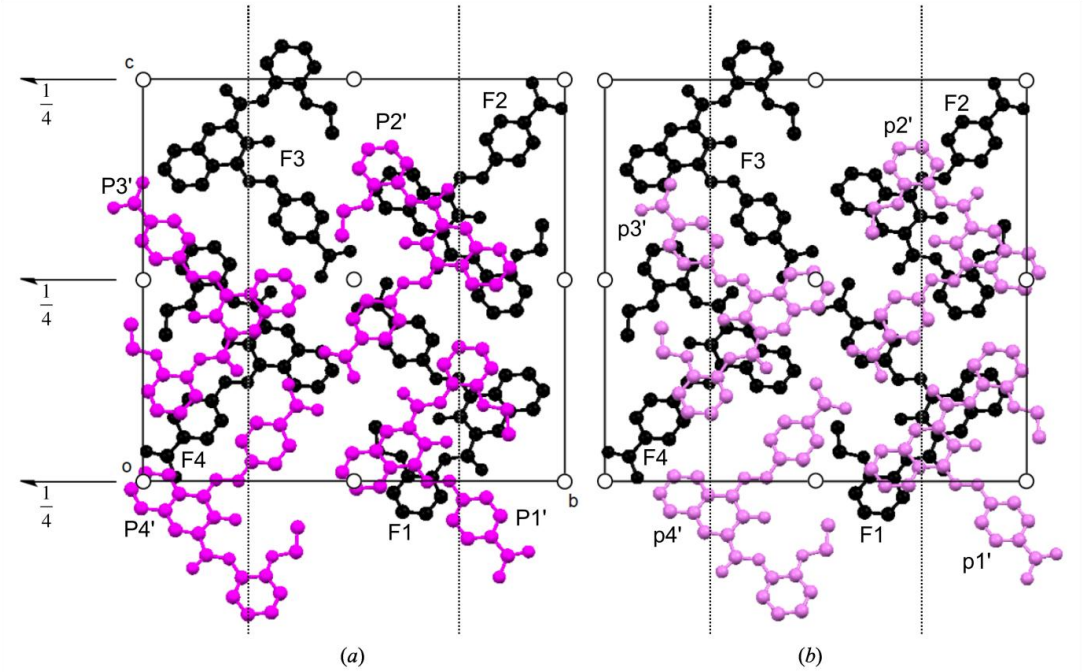


Figure 4.6: Projection of molecular layers at $x$ = 0 (ordered, black) and ¼ (disordered, magenta and violet) down **a** in model 2. (*a*) The arrangement of the major component of the layer at $x$ = ¼ (magenta) with respect to the ordered layer. The two layers are related to each other by non-crystallographic inversion centers at (⅛, ¼ - 0.039, ⅛); (⅛, ¼ - 0.039, ⅝); (⅛, ¾ - 0.039, ⅛); (⅛, ¾ - 0.039, ⅝) and non-crystallographic *g*-glide planes at $y$ = 0 - 0.039 and ½ - 0.039. (*b*) Non-crystallographic inversion centers at (⅛, ¼ + 0.039, ⅛); (⅛, ¼ + 0.039, ⅝); (⅛, ¾ + 0.039, ⅛); (⅛, ¾ + 0.039, ⅝) and non-crystallographic *g*-glide planes at $y$ = 0 + 0.039 and ½ + 0.039 relate the minor component (violet) of the layer at $x$ = ¼ to the ordered layer at $x$ = 0. The crystallographic $2_1$ axes located in both major and minor layers at $x$ = ¼ are shown, while black dotted lines running parallel to the **c** axis at $y$ = ¼ and ¾ indicate crystallographic *a*-glide planes.

Table 4.2: Crystallographic data for both models

| | | |
|---|---|---|
| **Crystal data** | | |
| Chemical formula, *M*r | $C_{26}H_{22}N_4O_4$, 454.48 | |
| Crystal size (mm) | 0.30 × 0.15 × 0.15 | |
| Crystal system | Monoclinic | |
| $D_x$ (Mg m$^{-3}$) | 1.436 | |
| $\mu$ (mm$^{-1}$) | 0.10 | |
| **Data collection** | | |
| Diffractometer | Onyx CCD, KM6 SNBL, ESRF | |
| λ (Å) | 0.7083 | |
| Resolution (Å) | 0.54 | |
| Scan slicing (°) per frame | 1 | |
| Temperature (K) | 100 | |
| | Model 1 | Model 2 |
| *a*, *b*, *c* (Å) | 14.4285(5), 24.7715(5), 24.9914(8) | 14.4270(4), 24.7749(3), 25.0108(6) |
| $\alpha$, $\beta$, $\gamma$ (°) | 90, 109.738(3), 90 | 90, 109.786(2), 90 |
| *V* (Å$^3$) | 8407.5(4) | 8411.8(3) |
| *Z, Z'* | 16, 2 | 16, 4 |
| $R_{int}$ | 0.0699 | 0.0851 |
| Space group | $B2_1/g$ | $P2_1/a$ |
| Equivalent positions | *x, y, z*; ½+*x, y,* ½+*z*; ¾+*x,* ½-*y,* ¼+*z*; ¼+*x,* ½-*y,* ¾+*z*; -*x*, -*y*, -*z*; ½-*x*, -*y,* ½-*z*; ¼-*x,* ½+*y,* ¾-*z*; ¾-*x,* ½+*y,* ¼-*z* | *x, y, z* ; ½-*x,* ½+*y*, -*z* ; ½+*x,* ½-*y, z* ; -*x*, -*y*, -*z* |
| No. of measured reflections | 201947 | 405722 |
| No. of unique reflections | 27617 | 55249 |
| **Refinement** | | |
| *R*1 [$F^2 > 2\sigma(F^2)$], *wR*($F^2$), *S* | 0.1184, 0.3607, 1.398 | 0.1857, 0.5888, 2.028 |
| Occupation [major, minor] | 0.9294(7), 0.0706(7) | 0.6478(7), 0.3522(7) |

| | | |
|---|---|---|
| No. of reflections | 27617 | 55249 |
| No. of parameters | 822 | 1435 |
| No. of restraints | 528 | 1320 |
| $\Delta\rho_{max}$, $\Delta\rho_{min}$, rmsd (e/Å$^3$) | 1.77, -0.67, 0.18 | 1.20, -1.90, 0.15 |

### 4.2.3 Similarities and differences between models 1 and 2

It is important to identify the similarities and differences between the two proposed models for β-P.R.170 in order to understand and judge the meaning of models 1 and 2 with respect to the experimental scattering data and the structural disorder. A tool to analyse disordered arrangements of layers is provided by Order-Disorder (OD) theory (Dornberger-Schiff, 1956) and the main elements of this concept have been discussed in Chapter 2 (see §2.2). In the present case, it implies scrutinizing models 1 and 2 for local symmetries of individual layers and of pairs of layers. These symmetries are summarized in an OD groupoid symbol (§4.2.3.1), which characterizes all periodic and non-periodic polytypes in a single family. Groupoids are usually referred to a coordinate system with the usual translation vectors in the two periodic directions and an interlayer vector in the stacking direction, here $\mathbf{a}_0 = \mathbf{a}/4$, **b**, **c**. The local symmetries may produce non-standard systematic absences. These aspects are analysed in §4.2.3.2.

#### 4.2.3.1 Similarities and differences in direct space, OD-analysis

As mentioned before, both models are built from the same layers with approximate *p* 1 $2_1$/*c* 1 symmetry. Both models show displacive disorder to varying degrees arising purely from two disordered positions in the layers. The two positions are related by the vector 0.158**b**. Although the arrangement of the layers is different in the two average structure models, the relationships between nearest neighbour layers are the same. We discuss this aspect for model 1 only.

Detailed relationships between the molecules in a single layer of model 1 are shown in Fig. 4.5*b*. M1 and M2 (or the symmetry-related M4 and M3, respectively) constitute the asymmetric unit of the major component and, although symmetry independent, are related by the non-crystallographic glide plane perpendicular to **b** at $y$ = ½+0.039 with glide component [0, 0, ½]. Neighbouring layers are related by centres of inversion and *g*-glide operations of the *B*$2_1$/*g* space group.

Symmetry-independent molecules in neighbouring layers are related by non-crystallographic, local symmetry operations. A detailed analysis of these local symmetries shows that a molecule in a given layer is *always* related to one or more crystallographically independent molecules of the same orientation in the adjacent layers by one of the vectors [-1/4, 0.42, -1/4] (= -**a**/4 + 0.42**b** - **c**/4), [1/4, 0.42, 1/4], [1/4, -0.42, 1/4] or [-1/4, -0.42, -1/4] of length ~12.1 Å. As an example, M1 at $x$ = ⅛ is related to M3' at $x$ = ⅜ by the second vector above (Fig. 4.7). Alternatively, the route from M1 to M3' at $x$ = ⅜ can be given in terms of a combination of crystallographic and non-crystallographic symmetry operations. First, M1 is transformed to its inversion-related mate, M1' [see Fig. 4.5*b*] in the layer at $x$ = ⅜ by the crystallographic inversion center at (¼, ½, ¼) and then M1' is transformed to M3' by the non-crystallographic layer inversion center at (3/8, ~0.709, 3/8). The major molecule M1 is also related to the minor molecule m3' of the same orientation at $x$ = ⅜ by the vector [1/4, -0.42, 1/4]. Alternatively, M1 is found to be symmetry-related to m3' by the crystallographic inversion symmetry operation $\bar{1}$(¼,½,¼) followed by the non-crystallographic layer inversion operation $\bar{1}$(3/8, ~0.290, 3/8). The relationships discussed here for individual molecules hold for entire layers. Two neighbouring layers are also related by a twofold screw operation with a translational component of + or -0.079**b** at (1/4, y, 0), for example. The presence of alternative positions for the molecules in a successive layer of β-P.R.170 can be considered in terms of the analogy of close packing of spheres, as depicted in Fig. 2.1. Given a close-packed layer, A, there are two possible geometrically and energetically equivalent positions, B or C, for the next layer, such that spheres in B or C sit over the interstices in A. At any one time only half of the interstices are occupied in this way, so only one position (either B or C) is realized.

The local relationships in model 2 are the same, but because of the different space group, the separation of operations into global and local ones is different from that in model 1.

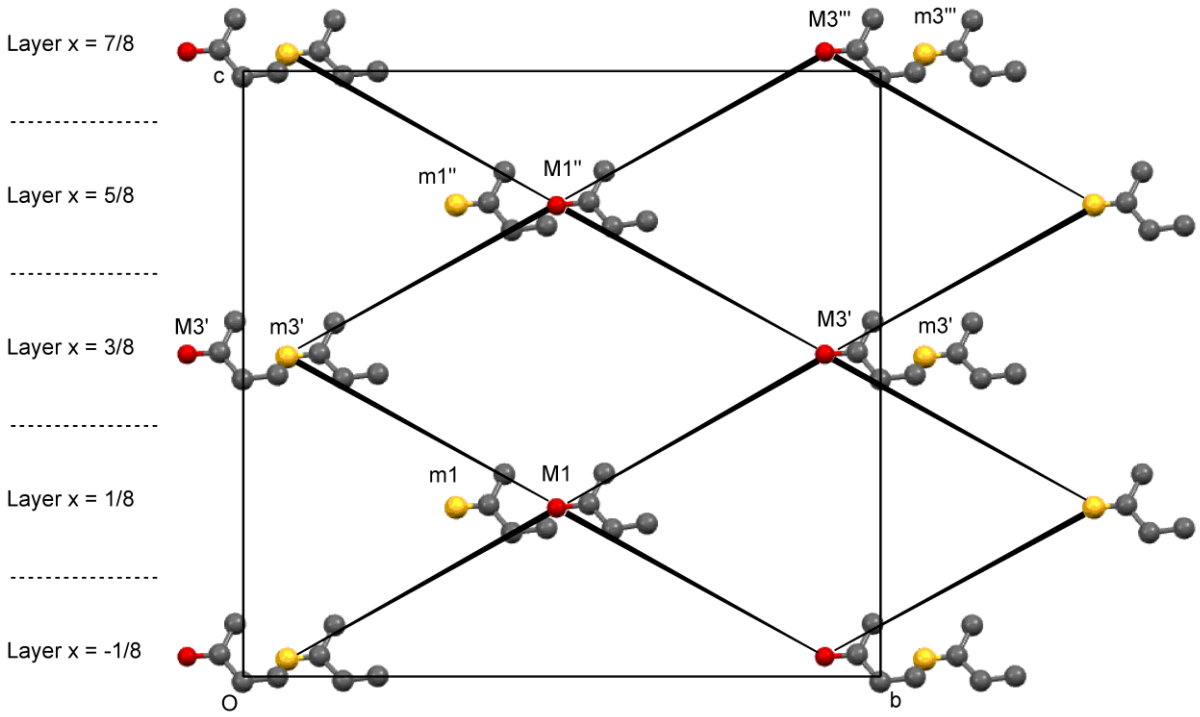


Figure 4.7: The arrangement of vectors relating molecules of the same orientation in model 1, as viewed down **a**. Layers of P.R.170 molecules are schematically represented by four atom fragments whose *x*-coordinates are given at the left of the figure and represented by primed symbols. Red spheres represent the keto-oxygen atoms in molecules of the major component while yellow spheres represent the same atom in the minor components (Fig. 3.1). Oxygen and attached carbon atoms (grey) define the orientation of the molecule in each layer. Wedged bonds (black) connecting oxygen atoms represent layer-to-layer vectors. Note that molecule M3' is shifted by [0, 1, 0] relative to molecule M3' in Fig. 4.5*b*.

There is one exception to the local symmetry relationships described in the preceding paragraph. The minor components in two consecutive layers of model 1 would be related by screw operations with translational components of + or -0.24**b**.

Summarizing in terms of groupoid language, every pair of layers in both models 1 and 2 is related by local twofold screw operations with screw component +0.079**b** or -0.079**b**, symbols $2_{0.158}$ and $2_{-0.158}$, and diagonal glide operations with glide components [¼, 0, -¼] or [1, 0, -¼] if referred to $\mathbf{a}_0$, **b**, **c**, symbol $n_{-1/2,2}$. The combination of the two operations implies local inversion operations and non-crystallographic translations, symbols $t_+$ = [¼, 0.421, ¼] and $t_-$ = [¼, -0.421, ¼], or [1, 0.421, ¼] and [1, -0.421, ¼] if referred to $\mathbf{a}_0$, **b**, **c**. These operations lead to the following groupoid symbol:

$P \quad (1) \qquad 2_1/c \qquad 1$

$\{(1) \qquad \frac{2_{0.158}}{n_{-1/2,2}} \qquad 1\}$

The local inversion and translation operations between layers mentioned above are implied by this groupoid.

The screw and inversion operations of an individual layer imply that both sides of a layer are symmetry-related and thus equivalent. Together with the local screw and inversion operations between layers, it follows that all interlayer contacts in both models 1 and 2 are equivalent. However layer triples, quadruples, *etc*. differ in the two models. To the extent that the crystal cohesive energy is dominated by nearest neighbour, pairwise contacts, the different stackings will differ little in crystal energy implying a disordered stacking sequence. However, its exact nature will depend on the next-to-nearest neighbour and higher interactions as well as the crystal growth conditions (Dornberger-Schiff & Grell-Niemann, 1961; Durovič, 2006).

The simplest way to describe the layer sequences of models 1 and 2 is in terms of $t_+$ and $t_-$. Thus the major components of model 1 are related by the translation sequence $t_+$, $t_-$, $t_+$, $t_-$ when starting with M1 in Fig. 4.7. There are then two possible alternating sequences of layers with major and minor occupation: starting from M1 with the translation sequence $t_-$, $t_+$, $t_-$, $t_+$, or from M3' with the sequence $t_+$, $t_-$, $t_+$, $t_-$. For model 2, the layer sequence starting from an ordered layer, e.g. F1 in Fig. 4.8, is either $t_+$, $t_-$, $t_-$, $t_+$ when including the disordered layer with major occupation (P3') or $t_-$, $t_+$, $t_+$, $t_-$, when including the disordered layer with minor occupation (p3') (Figs. 4.6*b* and 4.8). In model 1, the operation $n_{-1/2,2}$ is global. The structure formed by the layers with major occupation therefore has a maximum degree of order [MDO; Dornberger-Schiff, (1982)]. In model 2, none of the operations relating the layers into pairs is global; any sequence of layers includes more than one type of layer, i.e. layers with full and layers with major or minor occupation, and is thus a non-MDO polytypic structure in the OD family. Note that the above sequences of layers are meant to describe the average structures in a simple way. They are not necessarily the ones occurring most frequently in the disordered crystal.

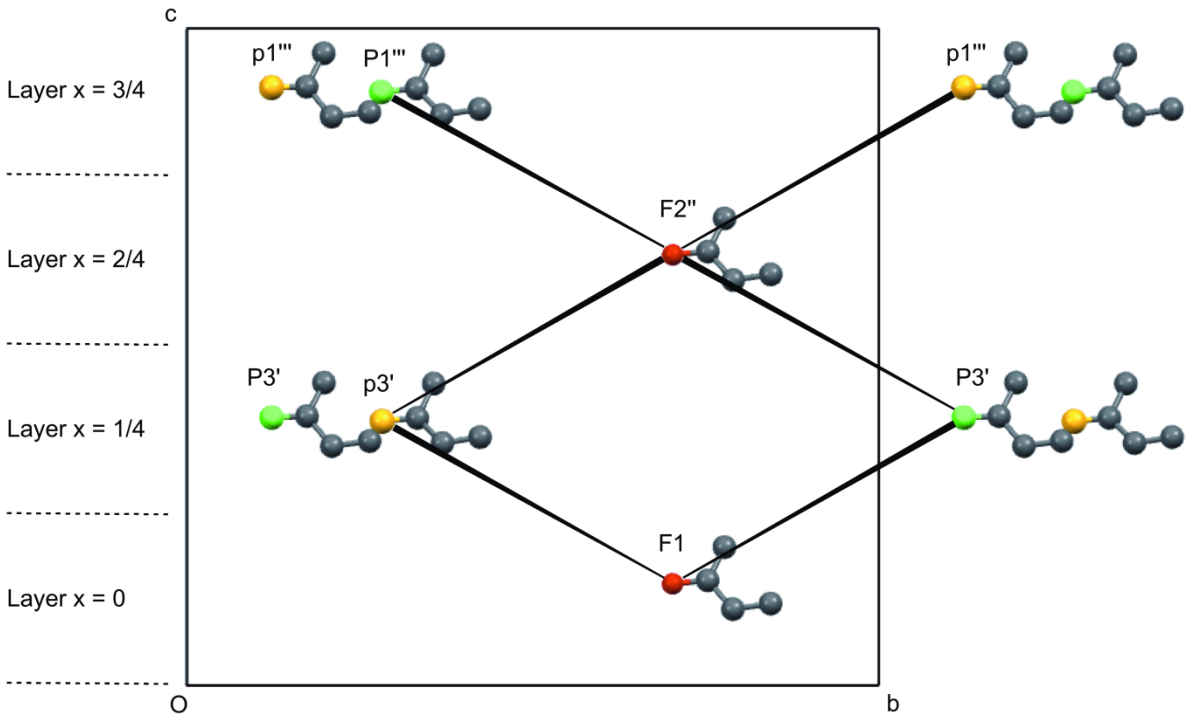


Figure 4.8: The arrangement of vectors relating molecules of the same orientation in model 2 as viewed down **a**. Layers of P.R.170 molecules are schematically represented by four-atom fragments whose *x*-coordinate is given at the left of the figure and represented by primed symbols. Red spheres indicate exocyclic oxygen atoms in fully occupied molecular layers while green spheres indicate the same oxygen atoms of the major component in the disordered layer. Corresponding oxygen atoms in the minor component are represented by yellow spheres. Wedged bonds (black) connecting oxygen atoms represent layer-to-layer vectors.

### 4.2.3.2 Similarities and differences in reciprocal space

The displacement between the major (M or P) and the minor (m or p) components along **b** explains the features in the diffraction pattern that tend to recur with a periodicity of (1/0.158)**b*** (= 6.33**b***, see §3.2.1). The superposition of equal layers with major and minor occupation can be considered as binary disorder. In such cases, the diffuse scattering is proportional to the difference in the scattering of the disordered species (Welberry, 2004). In the present case, this difference is $2(A + B)[1 - \exp 2\pi i(0.158k)]$ [$2(A + B)$ is the layer form factor taking into account the layer symmetry $p\ 1\ 2_1/c\ 1$] and implies that when $0.158k$ is an integer, e.g. 0 or 1 for $k$ = 0 or 6.33, the difference is zero and there is no diffuse scattering, as observed, at least approximately for $h0l$ and $h6l$. Conversely, the diffuse scattering is maximal if $0.158k$ is half-integer, e.g. 1/2 or 3/2 for $k$ = 3.16 or 9.5, again as observed for $h3l$, $h9l$ and $h10l$ (Figs. 3.2 and 3.4). The same observation also holds for higher values of $k$.

The local symmetries usually lead to non-crystallographic absences (Merlino, 1997). In the present case, these are fairly complex and not always perfect due to the fact that the local screw and translation components are not simple fractions of **b** (*viz*. 0.079**b** and 0.421**b**). The structure factor for model 1 can be written as

$$\begin{aligned} F(hkl) &= 2[\Sigma \cos 2\pi(hx_i + ky_i + lz_i) + \Sigma \cos 2\pi(hx_i - ky_i + lz_i) \cos 2\pi(k/2 + l/2)] \\ &\quad [2M \cos 2\pi(h/8 + l/8 + 0.21k) + 2m \cos 2\pi(h/8 + l/8 - 0.63k) \\ &\quad + 2M \cos 2\pi(3h/8 + 3l/8 - 0.21k) + 2m \cos 2\pi(3h/8 + 3l/8 + 0.63k)] \\ &= 2(A + B)\,[2M \cos 2\pi(h/8 + l/8 + 0.21k) + 2m \cos 2\pi(h/8 + l/8 - 0.63k) \\ &\quad + 2M \cos 2\pi(3h/8 + 3l/8 - 0.21k) + 2m \cos 2\pi(3h/8 + 3l/8 + 0.63k)] \end{aligned}$$

corresponding to layers with occupation M at (1/8, 0.21, 1/8), (-1/8, -0.21, -1/8), (3/8, -0.21, 3/8) and (-3/8, 0.21, -3/8) and layers with occupation m at (1/8, -0.63, 1/8), (-1/8, 0.63, -1/8), (3/8, 0.63, 3/8) and (-3/8, -0.63, -3/8); The structure factor for model 2 can be written analogously:

$$\begin{aligned} F(hkl) &= 2(A + B)[1 + 2P \cos 2\pi(h/4 + l/4 + 0.42k) + \\ &\quad 2p \cos 2\pi(h/4 + l/4 - 0.42k) + \cos 2\pi(h/2 + l/2)] \end{aligned}$$

corresponding to fully occupied layers F at (0, 0, 0) and (½, 0, ½) and partially occupied layers P or p displaced by $t_+$ or $t_-$. To the extent that the atoms in a given layer are coplanar, the layer form factor $2(A + B)$ essentially consists of continuous lines at integer values of $k$ and $l$ which are parallel to **a***. Its absolute value decreases with increasing $h$ due to the decrease of the atomic scattering factors, as may be gleaned from the diffuse scattering pattern.

The patterns of strong and weak lines of reflections ($h+n$, $k$, $-h$) in the (1 0 -1) direction described at the end of §3.2.1 and discernible from Figs. 3.2 and 3.4, follow from the modulation of the layer form factor by the terms in square brackets. Their values calculated for different values of $k$ and $n$ are given in Table 4.3. Their pattern is very similar for both models 1 and 2. The main difference is in the lines ($h+2n+1$, $k$, $-h$), which are absent in model 1 due to the B-centering and present, but weak in model 2. The presence of the diffuse scattering makes it very difficult to decide whether or not the reflections ($h+2n+1$, $k$, $-h$) are present in the experimental data and thus to distinguish qualitatively between the *B*-centred lattice of model 1 and the primitive lattice of model 2. The similarity of the patterns of strong and weak lines ($h+2n$, $k$, $-h$) precludes a distinction based on a purely qualitative comparison.

The *R*-factors (*R*1) calculated with only the (*h*+2*n*, *k*, -*h*) reflections, which overall are stronger than the (*h*+2*n*+1, *k*, -*h*) reflections, are 0.12 for model 1 and 0.18 for model 2 indicating that model 1 is probably a better explanation of the data than model 2.

Note also that in regions with distinct Bragg scattering, the intensity alternation for the lines (*h*+2*n*, *k*, -*h*) is relatively clear-cut (e.g. *k* = 0, 1, 2, 5, 6, 7, 8), whereas in regions with strong diffuse scattering the alternation disappears (e.g. *k* = 3, 4, 9, 10).

Table 4.3: Coefficients of the layer form factor along (*h*+n, *k*, -*h*)

| ***k*** | **n** | **Model 1** | **Model 2** | ***k*** | **n** | **Model 1** | **Model 2** |
|---|---|---|---|---|---|---|---|
| 0 | 0 | **4** | **4** | 6 | 0 | -0.18 | 0.02 |
| 0 | 1 | 0 | 0 | 6 | 1 | 0 | 0.08 |
| 0 | 2 | 0 | 0 | 6 | 2 | **-3.99** | **3.98** |
| 0 | 3 | 0 | 0 | 6 | 3 | 0 | -0.08 |
| 0 | 4 | **-4** | **4** | 6 | 4 | 0.18 | 0.02 |
| | | | | | | | |
| 1 | 0 | 0.73 | 0.25 | 7 | 0 | **-3.89** | **3.86** |
| 1 | 1 | 0 | -0.29 | 7 | 1 | 0 | 0.22 |
| 1 | 2 | **-3.81** | **3.75** | 7 | 2 | -0.55 | 0.14 |
| 1 | 3 | 0 | 0.29 | 7 | 3 | 0 | -0.22 |
| 1 | 4 | -0.73 | 0.25 | 7 | 4 | **3.89** | **3.86** |
| | | | | | | | |
| 2 | 0 | **-3.28** | **3.07** | 8 | 0 | -1.31 | 0.73 |
| 2 | 1 | 0 | 0.51 | 8 | 1 | 0 | -0.46 |
| 2 | 2 | -1.51 | 0.93 | 8 | 2 | **3.44** | **3.27** |
| 2 | 3 | 0 | -0.51 | 8 | 3 | 0 | 0.46 |
| 2 | 4 | **3.28** | **3.07** | 8 | 4 | 1.31 | 0.73 |
| | | | | | | | |
| 3 | 0 | -2.33 | 1.87 | 9 | 0 | 2.73 | 2.37 |
| 3 | 1 | 0 | -0.6 | 9 | 1 | 0 | 0.59 |
| 3 | 2 | 2.53 | 2.13 | 9 | 2 | 2.13 | 1.63 |
| 3 | 3 | 0 | 0.6 | 9 | 3 | 0 | -0.59 |

| | | | | | | | |
|---|---|---|---|---|---|---|---|
| 3 | 4 | 2.33 | 1.87 | 9 | 4 | -2.73 | 2.37 |
| 4 | 0 | 1.72 | 1.15 | 10 | 0 | 2.92 | 2.62 |
| 4 | 1 | 0 | 0.54 | 10 | 1 | 0 | -0.57 |
| 4 | 2 | 3.11 | 2.85 | 10 | 2 | -1.92 | 1.38 |
| 4 | 3 | 0 | -0.54 | 10 | 3 | 0 | 0.57 |
| 4 | 4 | -1.72 | 1.15 | 10 | 4 | -2.92 | 2.62 |
| 5 | 0 | **3.7** | **3.62** | | | | |
| 5 | 1 | 0 | -0.35 | | | | |
| 5 | 2 | -0.92 | 0.38 | | | | |
| 5 | 3 | 0 | 0.35 | | | | |
| 5 | 4 | **-3.7** | **3.62** | | | | |

## 4.3 Subgroup analysis

In the two preceding sections, relationships between models 1 and 2 have been discussed. One may also ask whether there are models of lower symmetry common to models 1 and 2 and providing better descriptions of the average structure. To answer this question, both models were refined in all subgroups of their respective space group down to *P*1 and introducing additional (disordered) molecules if a difference Fourier indicated them. None of these models lead to *R*1 significantly lower than the value of ~0.12 found for the *B* $2_1/g$ model 1 (see Table 4.4). From this observation, it is concluded that model 1 is the most economic description of the Bragg data available in this study, *i.e*. the model with the highest symmetry, the smallest number of refinable parameters and the lowest *R*-factor.

Table 4.4: Important parameters of subgroup analysis of the two average models

| **Subgroup** | **Origin Shift** | **Unique ref.** | ***R***(int) | ***R*1** [$F_o$>4σ($F_o$)] | ***R*1** (all) |
|---|---|---|---|---|---|
| | | **Model 1 subgroups** | | | |
| *P*1 | ¼, 0, ¼ | 101466 | 0.081 | 0.1268 (47470) | 0.1947 (101466) |
| $P\bar{1}$ | ¼, 0, ¼ | 101466 | 0.081 | 0.1525 (47470) | 0.2191 (101466) |

| | | | | | |
|---|---|---|---|---|---|
| $P\bar{1}$ | 0, 0, 0 | 101466 | 0.081 | 0.1504 (47470) | 0.2174 (101466) |
| $P2_1$ | ⅜, 0, ⅛ | 56141 | 0.085 | 0.1291 (28583) | 0.1875 (56141) |
| $P2_1$ | ⅛, 0, -⅛ | 56141 | 0.085 | 0.1266 (28583) | 0.1854 (56141) |
| $B1$ | ¼, 0, ¼ | 50680 | 0.066 | 0.1188 (33855) | 0.1479 (50680) |
| $B\bar{1}$ | ¼, 0, ¼ | 50680 | 0.066 | 0.1333 (33855) | 0.1609 (50680) |
| $B2_1$ | ⅜, 0, ⅝ | 28066 | 0.070 | 0.1197 (19769) | 0.1445 (28066) |
| $Bg$ | ¼, -½, ¾ | 27639 | 0.070 | 0.1203 (19696) | 0.1445 (27639) |
| $B2_1/g$ | 0, 0, 0 | 27617 | 0.070 | 0.1319 (19694) | 0.1543 (27617) |
| **Model 2 subgroups (a** and **c** interchanged in TC2**)** | | | | | |
| $P1$ | 0, 0, 0 | 101466 | 0.081 | 0.1252 (47470) | 0.1929 (101466) |
| $P\bar{1}$ | 0, 0, 0 | 101466 | 0.081 | 0.1938 (47470) | 0.2600 (101466) |
| $P2_1$ | ¼, 0, 0 | 56141 | 0.085 | 0.1259 (28583) | 0.1844 (56141) |
| $Pc$ | 0, ¼, 0 | 55271 | 0.085 | 0.1719 (28316) | 0.2319 (55271) |
| $P2_1/c$ | 0, 0, 0 | 55249 | 0.085 | 0.1948 (28314) | 0.2504 (55249) |

## 4.4 Summary and Conclusions

The scattering of the disordered β-phase of Pigment Red 170 shows a mix of what looks like Bragg diffraction superimposed by rods of strong diffuse scattering that is difficult to disentangle. As a first step in the analysis of the total scattering of the crystal and the establishment of models describing the local structure, determination of an average structure has been attempted, but doing so was far from routine. The extraction of reliable Bragg intensities from the diffraction data is severely impeded by the interference from the diffuse scattering and the available integration software does not have sufficient flexibility to circumvent this problem. Two plausible models, with different space groups, were obtained for the average structure and non-standard space group settings were chosen so as to align the

rods of diffuse scattering along **a***; a convenience for comparing the models and the upcoming local structure modelling. Both models are built from the same molecular layers, which possess approximate *p* 1 $2_1$/*c* 1 symmetry and are stacked along **a***. Model 1 was established in the non-conventional space group *B*$2_1$/*g* with *Z* = 16. The asymmetric unit contains two disordered molecules which lie in the same layer and are each disordered over two positions related by a translation of 0.158**b**. Adjacent layers are related by crystallographic centers of inversion between the layers and by crystallographic *g*-glide planes, while the layers themselves have crystallographic $2_1$ symmetry, but only non-crystallographic inversion symmetry. Model 2 was developed in the space group *P*$2_1$/*a*. There are four independent molecules in the asymmetric unit distributed across two independent layers. One of the layers is fully ordered and alternates with the second layer, in which the two independent molecules are each disordered over two positions again related by the 0.158**b** translation. In contrast to the *B*$2_1$/*g* model, the ordered layers now have crystallographic inversion symmetry and non-crystallographic $2_1$ symmetry, while the disordered layers possess crystallographic $2_1$ axes and as well as non-crystallographic inversion centers.

A detailed analysis of the local and global symmetries using OD-theory showed not only that individual layers always show approximate *p* 1 $2_1$/*c* 1 symmetry, but also that all direct layer contacts are geometrically equivalent, as expected for polytypes within an OD-family. Salient features of the experimental diffraction pattern are explained qualitatively by both models. The agreement *R*-factors calculated for model 2 with all or a subset of reflections common to models 1 and 2 were significantly higher than that from model 1 and the difference Fourier maps obtained from the ordered layer in model 2 suggested the presence within these layers of additional disordered positions for the molecules, which, however, could not be modelled successfully. The tentative conclusion from this analysis is that the model developed in *B*$2_1$/*g* is the most appropriate representation of what we consider to be the average structure of β-P.R.170.

The diffraction pattern of β-P.R.170 is a fine example of a system that is right at the limit of being tractable with the tools developed for standard single crystal structure analysis. A number of important limitations are present. Since a considerable fraction of Bragg reflections are almost completely immersed in the diffuse streaks, obtaining a reliable orientation matrix and accurate Bragg intensities is extremely difficult. Secondly, although the layer stacking within each of the two models is different, they share common layer and nearest neighbour geometries. This complicates identifying differences between the two models. Lastly, the

choice of space group influences whether the various local symmetry elements in the real structure are required to be crystallographic or non-crystallographic. There is also no simple transformation between the two models. Although the model in space group $B2_1/g$ appears to be the most appropriate for describing the average structure of β-P.R.170, the limitations and difficulties described suggest that the model in space group $P2_1/a$ or indeed other polytypes are equally probable candidates for the average structure of this sample. This ambiguity may only be resolved after the local structure derived from the total scattering pattern has been established. This problem will be discussed in chapter 5.

*Note in Proof:*

During discussions at the 23rd IUCr Congress and General Assembly in Montreal, Canada, in August 2014 we learnt that crystals of the β-polymorph of Pigment Red 170 obtained from nitrobenzene are completely ordered (Rossair, 2014). The atomic coordinates of the ordered structure model were developed in the space group $P2_1/n$ and fit almost exactly those of the major occupied sites of the model 1 of the average structure developed in this thesis.

## 4.5 Bibliography

Chang, C. -H., Christie, R. M. & Rosair, G. M. (2003). *Acta Cryst*. C**59**, o556-o558.

Chang, C. H., Christie, R. M. & Rosair, G. M. (2009). *Dyes & Pigments,* **82**, 147-155.

Christie, R. M. (2002). Presentation on *Colorchem'02, 9th International Conference on Dyes and Pigments*, 12-16 May 2002. Špindlerův Mlýn, Czech Republic.

Christie, R. M., Huang, H.-Y., Chang, C. -H., Rossair, G. M. & Powell, A. (2014). In preparation.

Dornberger-Schiff, K. (1956). *Acta Cryst*. **9**, 593-601.

Dornberger-Schiff, K. (1982). *Acta Cryst*. A**38**, 483-491.

Dornberger-Schiff, K. & Grell-Niemann, H. (1961). Acta Cryst. **14**, 167-177.

Durovič, S. (2006). *International Tables for Crystallography*, Vol. C, 1st online ed., edited by E. Prince, ch. 9.2.2. pp. 760-773. Chester: International Union of Crystallography.

Farrugia, L. J. (1999). *J. Appl. Cryst.* **32**, 837-838.

Fischer, W. & Koch, E. (1992). *International Tables for Crystallography*, Vol. A, 3rd ed., edited by Th. Hahn, p. 795. Dordrecht: Kluwer Academic Publishers.

Kobelt, D., Paulus, E. F. & Kunstmann, W. (1972). *Acta Cryst*. B**28**, 1319-1324.

Kobelt, D., Paulus, E. F. & Kunstmann, W. (1974). *Z. Krist*. **139**, 15-32.

Kopský, V. & Litvin, D. B. (2010). Editors. *International Tables for Crystallography*, Vol. E, 2nd online ed., ch. 4.1, pp. 221-391. Chester: International Union of Crystallography.

Merlino, S. (1997). *EMU Notes in Mineralogy*, Vol. 1, *Modular Aspects of Minerals*, pp 1-28. Budapest: Eötvös University Press.

Paulus, E. F. (1982). *Z. Krist*. **160**, 235-243.

Rossair, G. (2014). Private communication. 23rd IUCr Congress and General Assembly, 5 -12 August 2014, Montreal, Canada.

Schmidt, M. U., Hofmann, D. W. M., Buchsbaum, C. & Metz, H. J. (2006). *Angew. Chem*. **118**, 1335-1340, *Angew. Chem. Int. Ed.* **45**, 1313-1317.

Sheldrick, G. M. (2008). *Acta Cryst.* A**64**, 112-122.

Warshamanage, R., Linden, A., Schmidt, M.U. & Bürgi, H.-B. (2014). *Acta Cryst*. B**70**, 283-295.

Welberry, T. R. (2004). *Diffuse X-Ray Scattering and Models of Disorder*, Oxford: Oxford University Press.

Whitaker, A. (1978). *Z. Krist.* **146**, 173-184.

# Beyond the average structure of β-P.R.170

## 5.1 Introduction to the local structure of β-P.R.170

According to OD theory, the two average structures obtained for β-P.R.170 in the previous chapter are valid superposition structures corresponding to two distinct layer-stacking sequences. Although OD theory nicely explains the symmetry aspect of different layer sequences, it cannot provide the sequence of stacking of layers. Teteruk *et al*. (2014) recently carried out extensive lattice-energy minimization calculations in order to obtain possible stacking sequences of layers. According to their calculations, the stacking sequences depend not only on the interaction energies of neighboring layers, but also on next-neighbor layers. This chapter covers the alternative possibility of using the Monte Carlo method to estimate the layer stacking sequences.

In the case of β-P.R.170, the outcome of the local structure modeling will be expressed as a set of conditional probabilities for the occurrence of different layer pairs. The modeling process begins by generating a random model crystal in the computer, with the proviso that the average site occupancies of the different alternative positions for the molecules found in the average structure are retained. In the next step, various modifications to this model crystal are introduced through MC simulations in order to get the energetically most favorable arrangement of layers. Lastly, the resulting model crystal is Fourier transformed and both the Bragg and diffuse intensities calculated. These calculated intensities are then compared with the experimental diffraction data. The most suitable set of MC parameters describes a model crystal that resembles the real crystal statistically. Therefore, the outline of this chapter is as follows: the first part covers the preparation of the experimental diffraction data for the local structure modeling; the second part will explain the construction of the model crystal. The calculation of intensities from the model crystal and comparison with the experimental diffraction intensities will be discussed in the last part of this chapter.

## 5.2 Experimental data for the local structure modeling

### 5.2.1 Measurement of diffuse scattering

Typical diffuse scattering intensities are on the order of ~$10^3$ – $10^4$ less intense than Bragg intensities (Welberry, 2004). However, exceptions like β-P.R. 170 are possible. Since diffuse scattering data, in general, are much weaker than Bragg data, the reliability of diffuse scattering data often depends on the quality of the experiments. Such experiments usually try to eliminate air scattering as far as possible and to avoid geometric distortions of diffuse scattering sometimes using curved detectors (Welberry, 2004). Also it is important to keep the same detector sensitivity by fixing the crystal-to-detector distance throughout the whole experiment (Welberry, 2004). Since diffuse scattering is continuous in reciprocal space, it is best measured with area detectors. Three types of detectors come into consideration for work of this kind.

*Using an image plate (IP) detector*

Image plates superseded the use of conventional photographic films in many fields such as the medical, industrial and crystallographic ones mainly due to their higher sensitivity and higher dynamic range (Estermann & Steurer, 1998). They fall into the category of area detectors. Their working principle is as follows. The photo-stimulable phosphor [BaF(Br,I): $Eu^{2+}$] of an image plate is capable of detecting X-rays within a broad energy range (5 – 100 keV). The X-rays pump electrons from the valence band to the conduction band where the electrons remain for longer periods. Over the time period chosen (exposure time) more and more electrons are pumped into the conduction band thereby integrating the signal. When the phosphor is stimulated by a red laser, the trapped electrons return to their ground states by emitting excess energy as photons. These photons are counted by a photomultiplier and the number of photons is proportional to the number of absorbed X-ray photons (Ermrich *et al*., 1997).

Image plates have a fairly good spatial resolution of 50-150 micron compared with 20 micron for photographic film. They also have a better dynamic range of $10^5$-$10^6$ compared with $10^2$-$10^3$ for photographic films (Estermann & Steurer, 1998). Despite the above advantages, several drawbacks can be identified.

The photons from high intensity Bragg peaks can completely swamp the detector. In these situations anomalous counts are recorded over a considerable number of pixels thus broadening the reflection envelope. This effect is known as the blooming effect and is quite

common with image plate detectors (Welberry, 2004). The blooming effect can greatly perturb the diffuse data collection.

Apart from the blooming effect there is another problem associated with image plates. When Bragg peaks are overexposed during diffuse scattering data collection, at the center of each bloomed region, a significant number of pixels are saturated. Fig. 5.1 shows the reciprocal lattice layer *h*3*l* from a β-P.R.170 crystal reconstructed with Marview using Mar data [dataset 3 (§3.1.2); Kabsch, 1988]. The regions shown in green are saturated and must be discarded prior to any analysis. This affects not only the *h*3*l* layer, but overall a significant portion of the data is saturated including some of the diffuse scattering signals, making dataset 3 less useful for disordered structure modeling.

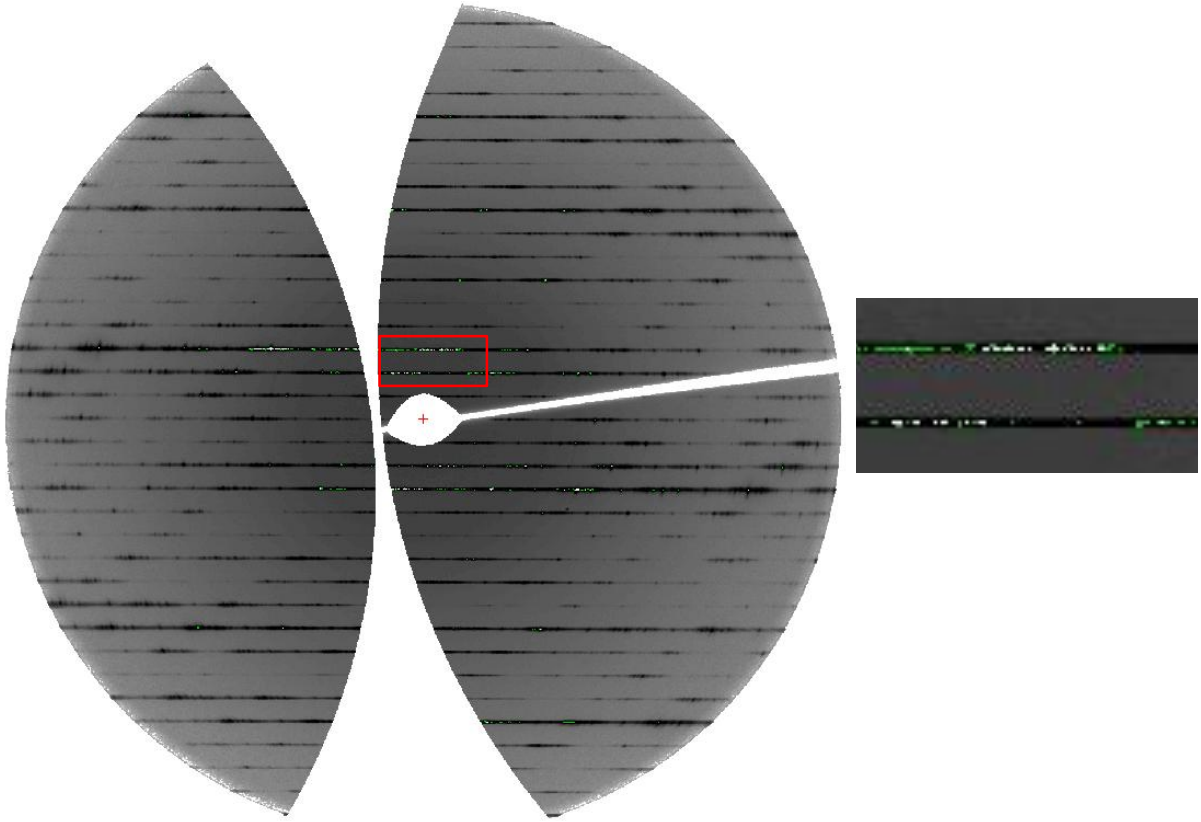

Figure 5.1: *h3l* reciprocal lattice layer of β-P.R.170 reconstructed with Marview (Kabsch, 1988). The region taken from the red rectangle is shown in the enlarged window. Regions shown in green are saturated.

There is another problem associated with very highly intense peaks. When the detector is in operation mode, each pixel is read out followed by a laser scan erasure. However, a single passage of the laser will not be sufficient to completely erase the image if pixels are saturated. In such cases, a part of the previous image will be retained and act as a ghost peak in

subsequent exposures. Depending on how strongly a detector area is overexposed, the ghost may remain for several subsequent scans. This effect is seen in reconstructed layers as powder lines (marXpert, 2014). Fig. 5.2 shows the *h*0*l* reciprocal lattice layer reconstructed from dataset 3 and the powder-like tails coming from the incomplete erasure of previous images.

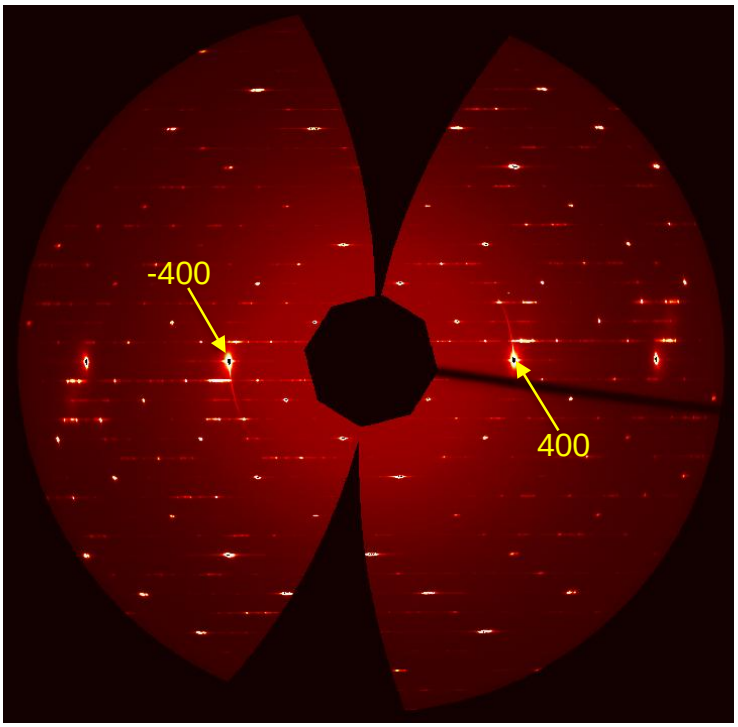


Figure 5.2: h0l reciprocal lattice layer of β-P.R.170. Readout effects are clearly seen as long curved tails on the 400 and -400 reflections.

Also image plates have a relatively long reading-and-erasing time. It depends on the size of the imaging plate and it is usually of the order of minutes (0.5 - 4) (Estermann & Steurer, 1998).

Fig. 5.3 shows a representative profile of a saturated reflection of dataset 3. The green columns represent the saturated pixels for which the count value exceeds the saturation limit of 2.5 x $10^5$ counts for the Mar345 image plate (marXperts, 2014). Some pixels in the middle part of the profile do not carry any value. Although the reason for not having values on some pixels is not known yet, the problem associated with this kind of profile is obvious. The remaining unsaturated peaks in the middle region of the envelope can be mistaken as sharp peaks which – if interpreted - will lead to wrong conclusions. It is worth mentioning how these features affected the current study.

One of the goals of the study was to determine the Laue symmetry of the diffuse diffraction pattern. It was attempted by carefully selecting a considerable number of (complete) reflection profiles from all parts of reciprocal space not knowing that a significant portion of dataset 3 is saturated. The results obtained from the symmetry analysis using Mar data (dataset 3) showed that the 2/*m* Laue symmetry, on which the average models were based, is not valid, not only for the diffuse scattering but also for the Bragg scattering. Since it is now known that the Mar data are problematic, conclusions made from the symmetry analysis of these data are incorrect.

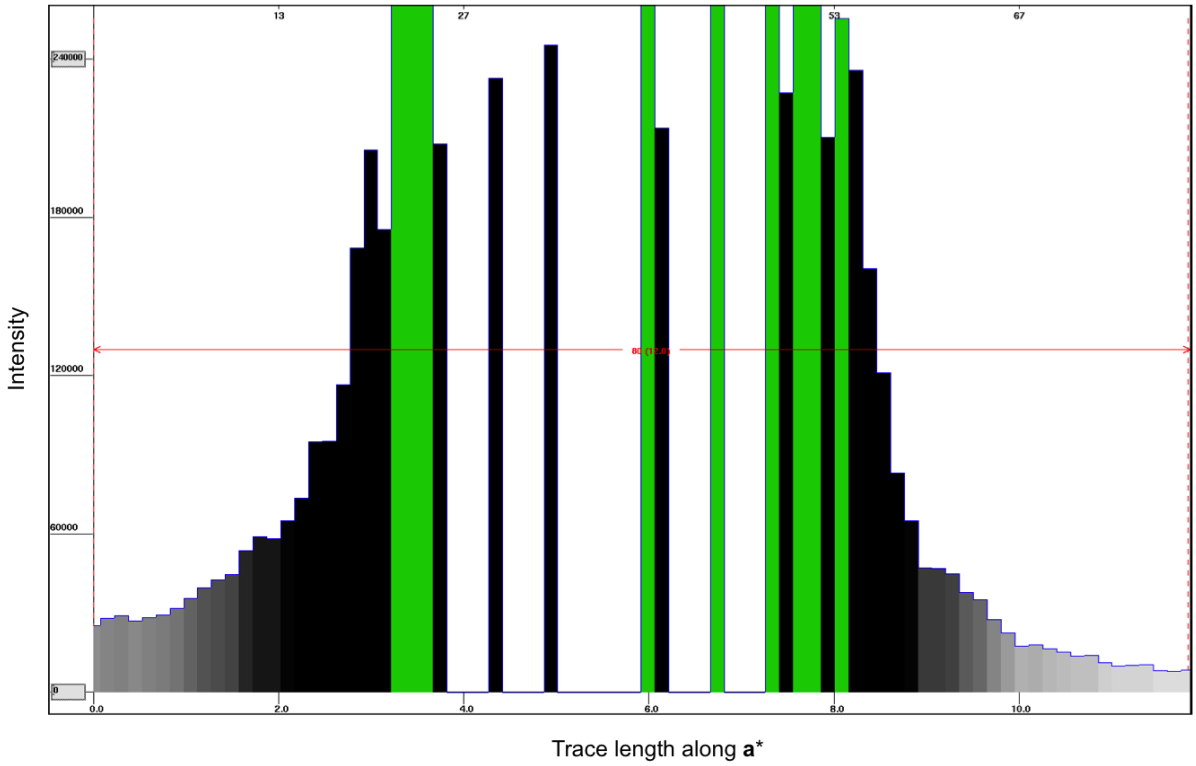


Figure 5.3: Profile of the 252 reflection along **a***. Vertical axis: intensity; horizontal axis: width of the reflection along **a*** in arbitrary units. For a detailed explanation of this figure see text.

All the above indicators suggested that our Mar data (dataset 3) from β-P.R.170 is problematic and not suitable for carrying out any reliable diffuse scattering study. At this point it was decided to re-measure the sample using the PILATUS 2M detector which has only recently been installed at the SNBL, so was unavailable when the project began.

*Using a CCD detector*

The datasets 1 and 2 (§3.1.2) measured on the KUMA CCD detector at the SNBL/ESRF were also not suitable for any diffuse scattering interpretation due to the following reasons. The available area of the CCD detectors is generally smaller than that of imaging plates. In order

to obtain the same coverage of reciprocal space, the detector must be brought closer to the crystal. Consequently, the spatial resolution of the diffuse signals becomes poorer. Similar to IP detectors, the blooming effect is also common to CCD detectors. In this case, the blooming is a result of the overflow of electric charge from one pixel to another when a high intensity Bragg peak saturates one or several pixels in the CCD chip (Welberry, 2004). Another problem associate with the CCD detectors is dark current noise. Dark current arises when the thermally excited electrons in the silicon lattice of the CCD enter the conduction band. Dark current often results in non-uniform noise in the signals (Truesense imaging, 2012). Therefore diffuse scattering data recorded with a CCD detector is not suitable for any accurate local structure modeling procedure.

*Using a PILATUS 2M detector*

Unlike image plates, these detectors are able to count just those X-ray photons which are above a certain energy threshold. The threshold is adjustable and the value should be chosen according to the type of experiment. The count rate is limited to ~$1.5 \times 10^6$ counts per second per pixel. The dynamic range of these detectors is about 1 - $10^6$ (20 bits). In PILATUS detectors, the point spread function (PSF), which is a measure of the detector contribution to the peak broadening, is only one pixel compared to several pixels in IPs. The pixel size is 0.172 mm for PILATUS detectors compared to 0.05 - 0.15 mm for IPs (Kraft, 2010). Since the noise is added to the signal per pixel (Estermann & Steurer, 1998), the signal-to-noise ratio is higher in PILATUS data than that in imaging plate data. The read-out time per frame for the PILATUS detector is negligible compared to image plates and is about ~2 ms (Kraft, 2010). This decreases the data collection time from hours to minutes. Therefore the use of PILATUS detectors is becoming popular in diffraction studies.

For the P.R.170 data recorded using the PILATUS detector, it was first checked that no pixels are saturated. In Fig. 5.4 the properly corrected H41 profile for Mar and PILATUS data are compared (preparation of diffuse data for quantitative modeling is discussed in section 5.2.2). This profile is the averages from four profiles according to the 2/m Laue symmetry. The intensity of the Mar profile is given on a logarithmic scale because of its large range. The intensity of the Pilatus profile is given on an absolute scale. In both plots, intensities are given in arbitrary units. Note that the horizontal axis H in each plot represents **a*** in the range $h$ = -10 to +10 along the diffuse streak. The region between two consecutive integers in $h$ has been

sampled with 100 subunits. Therefore the Bragg peaks are positioned at multiples of 100. H = 1000 corresponds to $h = 0$.

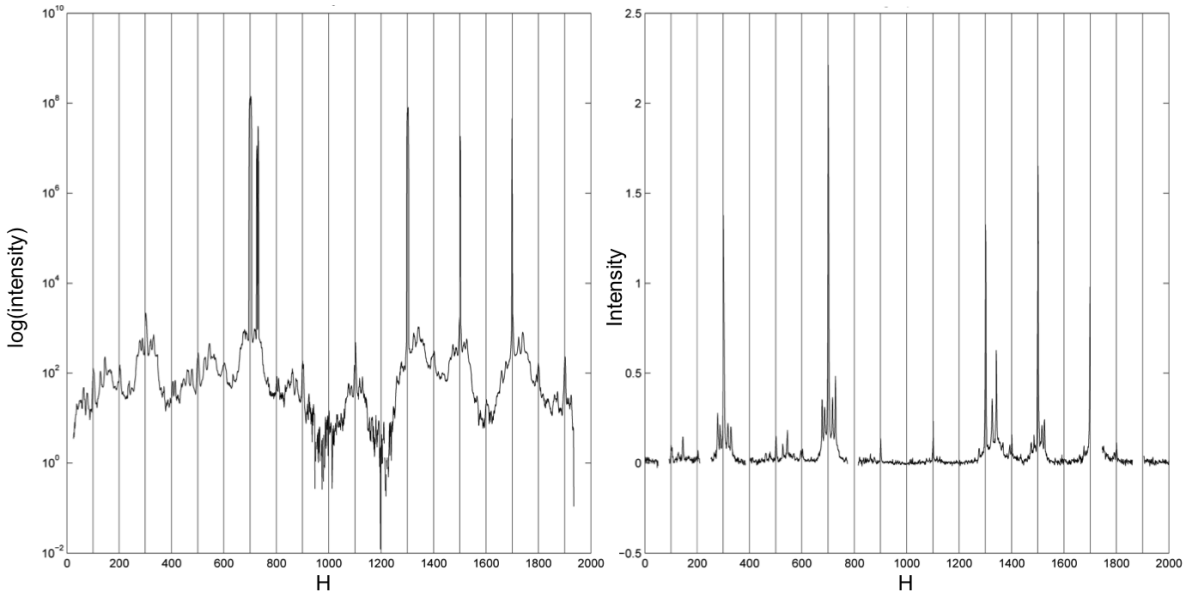


Figure 5.4: Symmetry-averaged H41 profiles from Mar data (left) and Pilatus data (right). Positions of Bragg peaks are marked with vertical lines.

The intensity levels in the two plots are significantly different by a factor of ~$4 \times 10^7$. The spatial resolution of peaks in the right figure is much better than that in the left figure. The better resolution can be attributed to the finer angular slicing used to measure the Pilatus data (i.e. 0.1° compared to 0.5° for the Mar data). Another distinct feature between the two profiles is that the intense satellite peak to the right of the Bragg peak at H = 700 in the Mar profile is not unusually intense in the Pilatus profile. The origin of this unusually intense peak in the Mar profile is not known yet. This anomaly appeared in many of the profiles constructed from the Mar data. Subsequently, for all modeling purposes, the diffuse scattering data collected with the PILATUS 2M detector were used.

### 5.2.2 Preparation of diffuse data for modeling

Diffuse scattering data need to be properly prepared before using them in the modeling. In order to extract scattering data from specific regions in reciprocal space, first the pixel data need to be reconstructed into a 3D volume of reciprocal space so that the scattering can be visualized and then extracted. This process requires the definition of a laboratory coordinate system, the distance between the crystal and the detector, the number of pixels and the length of each pixel along the $X_D$ and $Y_D$ coordinates of the detector, the orientation matrix of the

detector, the unit cell parameters, the *x*, *y*, *z*-coordinates of the unit cell axes in direct space and the wavelength of the radiation (Estermann, 2001).

The laboratory coordinate system can be any convenient right-handed orthonormal system whose origin is usually set at the intersection between the incident beam, and the rotation axis of the crystal. During data processing, the chosen laboratory coordinate system must be transferred into the data processing software. The laboratory coordinate system on the detector is dependent on the detector manufacturer. The convention for the PILATUS 2M detector is shown in Fig. 5.5.

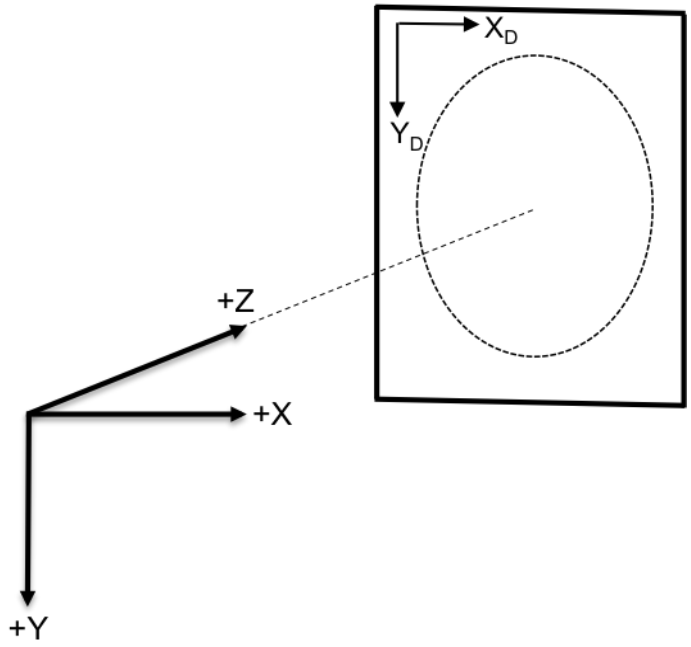


Figure 5.5: The laboratory coordinate system of the PILATUS 2M detector. The vectors $X_D$ and $Y_D$ denote the detector coordinate system.

The vector Z is parallel to the detector normal (when the swing angle of the detector is zero) and is positive from the X-ray source towards the detector. The vector X is parallel to the spindle axis.

The orthonormal vectors $X_D$ and $Y_D$ represent the detector coordinate system. Each reflection recorded on the detector is associated with a set of detector coordinates. The reciprocal unit-cell vectors **a***, **b*** and **c*** are determined by using a list of such reflections. The orientation matrix supplies the relationship between the reciprocal unit cell vectors (reciprocal lattice coordinate system) and the laboratory coordinate system if all goniometer angles equal zero.

For instance, assume that there is a vector $\boldsymbol{H}$ in the reciprocal coordinate system such that $\boldsymbol{H} = h\mathbf{a}^* + k\mathbf{b}^* + l\mathbf{c}^*$ where $h$, $k$ and $l$ are integers. With the aid of two matrices, namely **B** and **U**, $\boldsymbol{H}$ is transformed into an orthogonal vector $\boldsymbol{H}_{\text{orth}}$ in the laboratory coordinate system.

$$\boldsymbol{H}_{\text{orth}} = \mathbf{UB}\boldsymbol{H} \qquad (5.1)$$

The **U** matrix is known as the orientation matrix. The product of the two matrices **UB** is

$$\mathbf{UB} = \begin{bmatrix} a_x^* & b_x^* & c_x^* \\ a_y^* & b_y^* & c_y^* \\ a_z^* & b_z^* & c_z^* \end{bmatrix} \qquad (5.2)$$

where the elements of each column represent the components of each reciprocal base vector when expressed in the laboratory coordinate system. Thus knowledge of the **UB** matrix implies knowledge of the unit cell parameters.

The data processing program XDS (Kabsch, 1993) outputs all the necessary parameters for the reciprocal space imaging in the form of file XPARM.XDS which can be used directly as an input for reciprocal space imaging programs. In the current study, the diffuse data were processed with the imaging program XCAVATE (Estermann, 2001) and with MATLAB scripts (hereafter scripts) kindly supplied by Arkadiy Simonov of ETH Zürich, Switzerland. The file XPARM.XDS and the rotation images were used as input for both programs. The measured raw scattering data has to be corrected for several experimental factors such as polarization, crystal absorption and air absorption before using them in the qualitative and quantitative modeling of the material's disorder. Usually these corrections are applied pixelwise to the intensity data. Detailed procedures for the application of these corrections can be found in Estermann & Steurer (1998) and Estermann (2001).

With the scripts the desired volume of reciprocal space was reconstructed on a grid defined in the crystal coordinate system. The volume chosen has the following dimensions: $-10 < h < 10$; $-20 < k < 20$ and $-20 < l < 20$. The resolution along $h$ was chosen to be $0.01\mathbf{a}^*$, meaning that the distance between two consecutive Bragg maxima was sampled with 100 data points. Similarly, the resolution along $k$ and $l$ was chosen to be $0.1\mathbf{b}^*$ and $0.1\mathbf{c}^*$, respectively. The reason for finer sampling of $h$ is that in the current case the diffuse scattering runs as streaks along $\mathbf{a}^*$. The fine structure of these streaks will only be seen with finer sampling along that direction.

## 5.3 Construction of a model crystal

The construction of a model crystal in the computer is the first step of any local structure modeling process. This step is primarily based on the insights obtained from the average structure. It consists of two steps.

1. Disentanglement of the disordered average structure into chemically plausible structures (chemical units).
2. Building the initial crystal using the chemical units.

### 5.3.1 Disentanglement of the average structure and defining chemical units

The average structure is the projection of the whole crystal into one unit cell. Thus it may contain partially occupied atom sites, molecules or even molecular layers. Such an arrangement in a real crystal is chemically impossible. Each unit cell in a real crystal contains only one chemically feasible arrangement of atoms, molecules or molecular layers. The process of disentanglement separates the fictitious average structure into its physically meaningful components that occur in real crystals. For β-P.R.170, this process can be further explained as follows.

In order to facilitate the local structure modeling, it was first convenient to expand the two average structure models into space group $P\bar{1}$. [The lowering of space group symmetry was necessary because of limitations of the local structure modeling software (ZODS) at the time of this project.] Neither the coordinates nor the thermal parameters of the atoms were optimized after the transformation. Model 1 upon transformation from $B2_1/g$ to $P\bar{1}$ yielded two independent molecular layers, both disordered, one at $x$ = 1/8 and one at 3/8. Similarly, model 2 upon transformation from $P2_1/a$ to $P\bar{1}$ yielded two independent half-layers at $x$ = 0 and ½, both ordered, and one independent disordered molecular layer at $x$ = ¼ (Fig. 5.6).

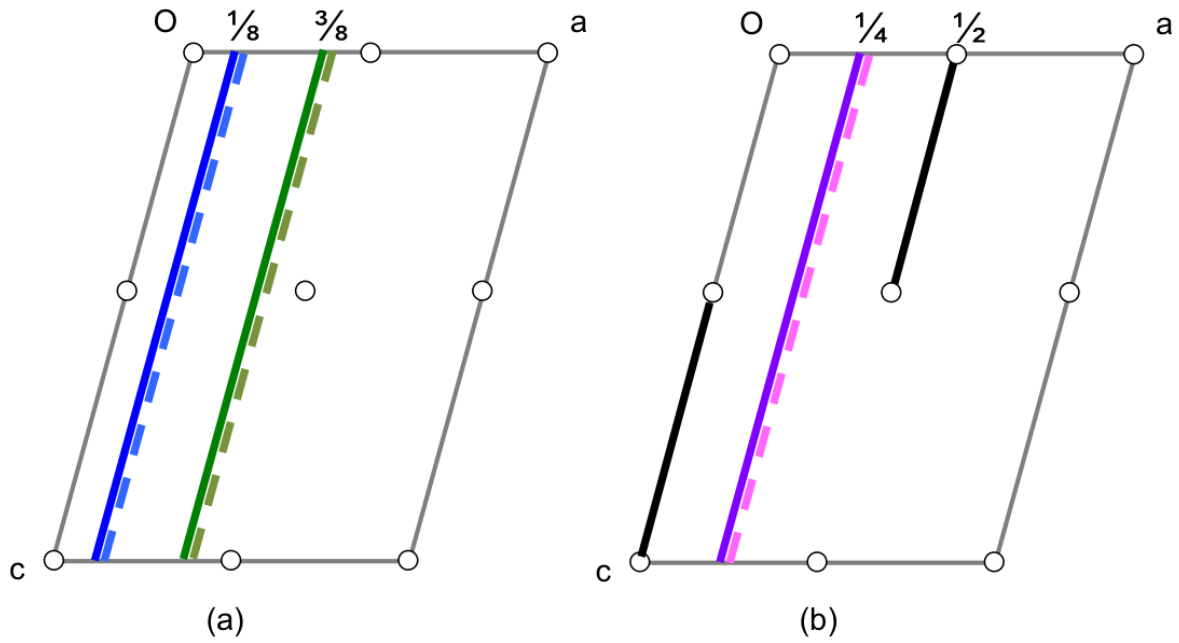


Figure 5.6: Schematic representation of the $P\bar{1}$ extension of (a) model 1: molecular layers are shown in blue and green. Dark blue and green solid lines represent major layer components at *x* = 1/8 and 3/8, respectively. Light blue and green dashed lines represent minor layer components at *x* = 1/8 and 3/8, respectively; (b) model 2: molecular layers are represented in black, purple and violet. Solid black layers are ordered. Solid purple (major) and dashed violet (minor) represent the components of the compound layer at *x* = ¼.

In the $P\bar{1}$ extension of model 1, each independent layer is disordered resulting in major (dark blue/green) and minor (light blue/green) layer components with occupancies of ~0.9 and ~0.1, respectively. Similarly, in the $P\bar{1}$ extension of model 2, the major (purple) and the minor (violet) layer components of the disordered layer at *x* = ¼ have an occupancy ratio of ~0.65 to ~0.35, respectively.

Even though two superimposed, disordered layers are possible in the average structure of β-P.R.170, the real crystal cannot have disordered layers. Only one of the two possibilities, either the major or the minor layer arrangement, is realized in any one layer in the real crystal. Therefore, it is necessary to disentangle the average structure into its physically occurring and chemically feasible building units before the model crystal is built. These building units are named *chemical units* (CUs). A chemical unit is defined as the set of atoms or molecules physically occurring in a given unit cell of a real crystal (Chodkiewicz *et al*., 2014). The process of obtaining them from the average structure is called the *disentanglement* of the average structure. Fig. 5.7 shows the average layers of model 1 of β-P.R.170. Since the $P\bar{1}$

extension of this model contains two disordered independent molecular layers, disentanglement results in four CUs, i.e. CU1, CU2, cu3 and cu4; 'CU' and 'cu' represent the chemical units with major and minor occupations, respectively.

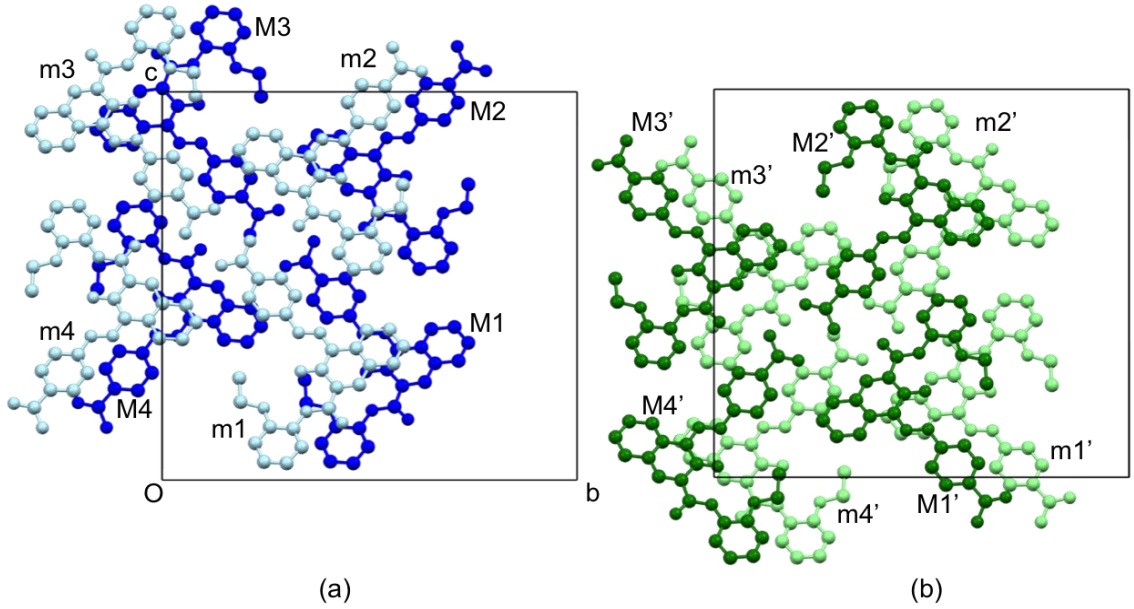


Figure 5.7: Average layers and disentanglement into chemical units of the $P\bar{1}$ extension of model 1. (a) compound layer at *x* = 1/8. CU1 = dark blue molecules (M1 – M4); cu3 = light blue molecules (m1 – m4). CU1 and cu3 form a set of alternatives (SOA-1). (b) compound layer at *x* = 3/8. CU2 = dark green molecules (M1' – M4'); cu4 = light green molecules (m1' – m4'). CU2 and cu4 form the second set of alternatives (SOA-2).

The model crystals should contain all four CUs in their correct proportions. The two independent layer positions of the $P\bar{1}$ extension of model 1 are occupied by one CU of the pair CU1/cu3 and one CU of the pair CU2/cu4, respectively. For example, the layer-position at *x* = 1/8 is occupied either by CU1 or cu3. They cannot occupy the same layer-position simultaneously. Their occurrence is mutually exclusive. [Note: it is important to realize that the disordered crystals are neither translationally symmetric nor is there a unit cell in the conventional sense.] The occupancy of a CU is always full and cannot be partial. CU1 and cu3, taken together, define the first set of alternatives (SOA-1). Similarly, the layer-position at *x* = 3/8 is occupied either by CU2 or cu4. These two chemical units form the second set of alternatives (SOA-2).

According to (the non-extended) model 1 of the average structure, any pair of consecutive layers is related by inversion symmetry. The same relationship should also be maintained between neighboring layers (CUs) of the model crystal. The only way of achieving this

arrangement in the model crystal is by alternating between the two sets of alternatives SOA-1 and SOA-2 in the layer stack.

Analogous to model 1, disentanglement of the $P\bar{1}$ extension of model 2 may be explained as follows. As mentioned earlier, this model has two independent ordered half-layers at $x$ = 0 and ½ and one independent disordered layer at $x$ = ¼. The ordered parts do not contribute to diffuse scattering, but they do contribute to the Bragg scattering. Therefore the disentanglement was performed in such a way that the ordered parts are also included in the resulting CUs. The disentanglement is shown in Fig. 5.8. The disordered layer at $x$ = ¼ was disentangled into major (magenta, left) and minor (violet, right) units. The ordered half-layers at $x$ = 0 and ½ shown in black are common to both CUs. Taken together, the two CUs (CU1 and cu2) form the set of alternatives in this model.

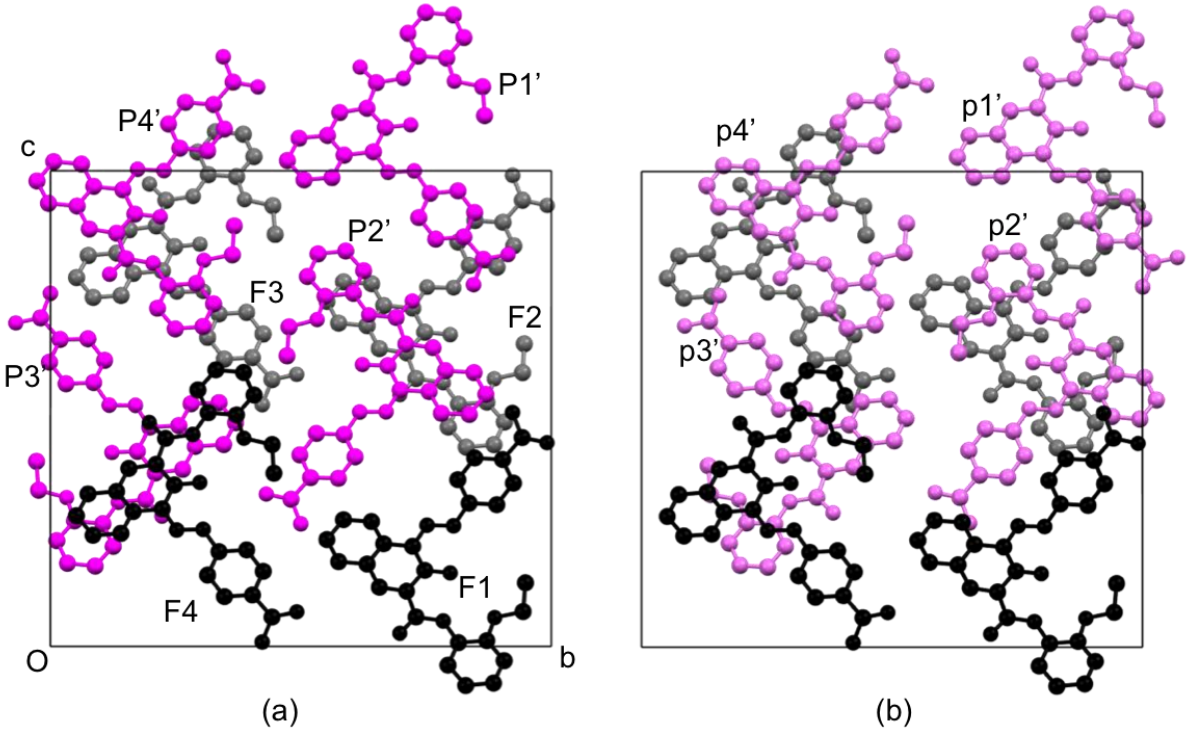


Figure 5.8: Disentanglement of the $\boldsymbol{P\bar{1}}$ extension of model 2. The half-layer at $x$ = 0 shown in grey consists of molecules F3 and F2. The half-layer at $x$ = ½ shown in black consists of molecules F1 and F4. (a) CU1 = full (F1 – F4) + major (magenta, P1' – P4') (b) cu2 = full (F1 – F4) + minor (violet, p1' – p4'). Note that F1 and F4 are the glide related molecules of F1 and F4 shown in Fig. 4.6.

### 5.3.2 Model crystal building and energy minimization

Once the average structure has been disentangled, the next step is to build the initial crystal. Starting with one chemical unit the crystal is grown layer-by-layer in the computer. The

disordered crystal of β-P.R.170 can be thought of as a linear array of two-dimensionally periodic molecular layers. However the sequence of CUs in the stack is not known but is to be found through modeling. The model crystal was chosen to consist of 1000 layers in the stacking direction and 1×1 unit cell in the periodic perpendicular directions. These dimensions were kept constant throughout the whole modeling process.

In general, the model crystal can be built in two different ways. One way is to use a simple Markov chain (Welberry, 2004). In this case the type and the probability of stacking faults should be known prior to building the crystal. Usually the knowledge of the type(s) of stacking is obtained via a detailed analysis of the Bragg diffraction pattern. The probability of stacking faults can be taken as an *a priori* value. Once the first CU is chosen randomly, the next CU to be added is controlled by a random number generated in the range 0 to 1. If the random number is lower than the stacking fault probability, a fault is introduced into the stack at the next layer position. If the number is greater than the stacking probability, no fault is introduced. The crystal obtained according to this method is used directly to calculate intensities. If the match between the calculated and the experimental intensities is unsatisfactory, then another crystal is created with a different set of stacking fault probabilities. This is the method used by Berliner and Werner (1986) for building disordered layer sequences of cubic and hexagonal close-packed structures of equal spheres. The best set of stacking fault probabilities can be obtained by global optimization method such as differential evolution (Weber & Bürgi, 2002).

The second method of model-crystal building uses estimated values for interaction energies instead of estimated stacking fault probabilities. This is the method used to grow the model crystal of β-P.R.170. The initial crystal is totally random, except for the condition that the average occupancies of the different alternative positions for the molecules found in the average structure are retained, but does not contain any correlation between CUs on average. This is achieved with the help of a random number generator.

In the next step, correlations between CUs are introduced in terms of interaction energies and the crystal energy is calculated. Then the crystal energy is minimized via a Monte Carlo simulation and the equilibrated crystal is obtained. Vectorial relationships between adjacent layers in both average models of β-P.R.170 were already discussed in the average structure section (§4.2.3.1). In this section, those relationships are expressed in terms of interactions between CUs. Model 1 will be discussed first.

The model 1 when expressed in $P\bar{1}$, contains two independent disordered layers resulting in four CUs, namely CU1, CU2, cu3 and cu4. All possible nearest neighbor interactions among the four CUs located in the two adjacent independent layers (Nos. 1 – 4) and those between symmetry related CUs (Nos. 5 – 12) are given in Table 5.1. According to OD theory and the vectorial relationships between adjacent layers discussed in §4.2.3.1, layer-to-layer interactions can be simplified. Those simplified interactions are presented in the last column of Table 5.1.

Table 5.2: All possible interactions in the $\boldsymbol{P\bar{1}}$ model from model 1. The vectors given correspond to those between two interacting molecules as shown in Fig. 4.7. Translated versions of M3''' and m3''' are indicated by (-**a**)

| No. | Vector | Vec. components | Interaction | Parameter |
|---|---|---|---|---|
| 1 | M1→ M3' | ¼, 0.42, ¼ | CU1(X, Y, Z) – CU2(X, Y, Z) | P1 |
| 2 | M1 → m3' | ¼, -0.42, ¼ | CU1(X, Y, Z) – cu4(X, Y, Z) | P2 = P1 |
| 3 | m1 → M3' | ¼, -0.42, ¼ | cu3(X, Y, Z) – CU2(X, Y, Z) | P3 = P1 |
| 4 | m1 → m3' | ¼, -0.26, ¼ | cu3(X, Y, Z) – cu4(X, Y, Z) | P4 |
| 5 | M1 → M3'''(-a) | -¼, 0.42, -¼ | CU1(X, Y, Z) – CU1(-X, -Y, -Z) | P5 = P1 |
| 6 | M1 → m3'''(-a) | -¼, -0.42, -¼ | CU1(X, Y, Z) – cu3(-X, -Y, -Z) | P6 = P1 |
| 7 | m1 → M3'''(-a) | -¼, -0.42, -¼ | cu3(X, Y, Z) – CU1(-X, -Y, -Z) | P7 = P1 |
| 8 | m1 → m3'''(-a) | -¼, -0.26, -¼ | cu3(X, Y, Z) – cu3(-X, -Y, -Z) | P8 = P4 |
| 9 | M3' → M1'' | ¼, -0.42, ¼ | CU2(X, Y, Z) – CU2(1-X, -Y, -Z) | P9 = P1 |
| 10 | M3' → m1'' | ¼, 0.42, ¼ | CU2(X, Y, Z) – cu4(1-X, -Y, -Z) | P10 = P1 |
| 11 | m4 → M1'' | ¼, 0.42, ¼ | cu4(X, Y, Z) – CU2(1-X, -Y, -Z) | P11 = P1 |
| 12 | m4 → m1'' | ¼, 0.26, ¼ | cu4(X, Y, Z) – cu4(1-X, -Y, -Z) | P12 = P4 |

The value of P4 was set to be dependent on P1 according to the formula P4 = -P1. For the modeling, only the non-redundant, i.e. OD symmetry independent interactions 1, 2, 3, 4, 5, 6, 8, 9, 10 and 12 have to be considered in ZODS. The parameter value for P1 was arbitrarily

chosen to be -0.65. The absolute magnitudes of the interaction parameters are not important, but their relative values determine which interactions are going to be important in the structure. For example, P1 < P4 means that CU1 – CU2 interactions are more favorable than cu3 – cu4 interactions.

Next, the interactions of the $P\bar{1}$ extension of model 2 are discussed. This model contains ordered half layers at $x$ = 0 and ½ and one disordered layer at $x$ = ¼ [see Fig. 5.6(b)]. Upon disentanglement, two chemical units CU1 and cu2 were obtained (see Fig. 5.8). In space group $P\bar{1}$, four interactions are possible and are given in Table 5.2. According to OD theory and vectorial relationships shown in Fig. 4.8, all layer-to-layer relationships are the same. Since equivalent layer pairs imply equivalent energies, all combinations of CUs are energetically equivalent. The simplified interactions are also presented in the last column of Table 5.2.

Table 5.2: All possible interactions in the $\boldsymbol{P\bar{1}}$ model from model 2. The vectors given include both layer-to-layer vectors between the two interacting molecules shown in Fig. 4.8.

| No. | Vector | Vec. components | Interaction | Parameter |
|---|---|---|---|---|
| 1 | P3’ → F2’’<br>F2’’ → P1’’’ | ¼ , -0.42, ¼<br>¼ , -0.42, ¼ | CU1(X, Y, Z) – CU1(-X, -Y, -Z) | P1 |
| 2 | P3’ → F2’’<br>F2’’ → p1’’’ | ¼ , -0.42, ¼<br>¼ , 0.42, ¼ | CU1(X, Y, Z) – cu2(-X, -Y, -Z) | P2 = P1 |
| 3 | p1’’’ → F2’’<br>F2’’ → P3’ | -¼ , -0.42, -¼<br>-¼ , 0.42, -¼ | cu2(X, Y, Z) – CU1(-X, -Y, -Z) | P3 = P1 |
| 4 | p3’ → F2’’<br>F2’’ → p1’’’ | ¼ , 0.42, ¼<br>¼ , 0.42, ¼ | cu2(X, Y, Z) – cu2(-X, -Y, -Z) | P4 = P1 |

Only the non-redundant, OD-symmetry independent interactions 1, 2 and 4 have to be included in the modeling with ZODS. The simplest interaction model considers only interactions between nearest-neighbor CUs. For model 2 the interactions for all layer pairs are

therefore equal (Table 5.2) and the resulting crystal is indistinguishable from a random crystal.

Once the interactions and their parameter values are chosen, the interaction energy of the crystal is calculated. This is done according to eq. 1.2 discussed in §1.3.1, i.e.:

$$E_{tot} = \sum_{i,j} \varphi\,(\sigma_i, \boldsymbol{r}_i, \dots, \sigma_j, \boldsymbol{r}_j, \dots)$$

For β-P.R.170, this simplifies to

$$E_{tot} = \sum_i \varphi(\sigma_i, \sigma_{i-1}). \qquad (5.3)$$

Eq. 5.3 can be rewritten according to the usual notation used in Ising models (Welberry, 2004) as follows:

$$E_{tot} = \sum_i J\sigma_i\sigma_{i-1} \qquad (5.4)$$

where $J$ is the interaction parameter between the two CUs defined by $\sigma_i$ and $\sigma_{i-1}$. $\sigma_i$ is a binary variable having only two possible values, +1 or -1 determining the sign of the interaction energy between two interacting CUs. This situation for a part of model 1 crystal is shown pictorially in Fig. 5.9.

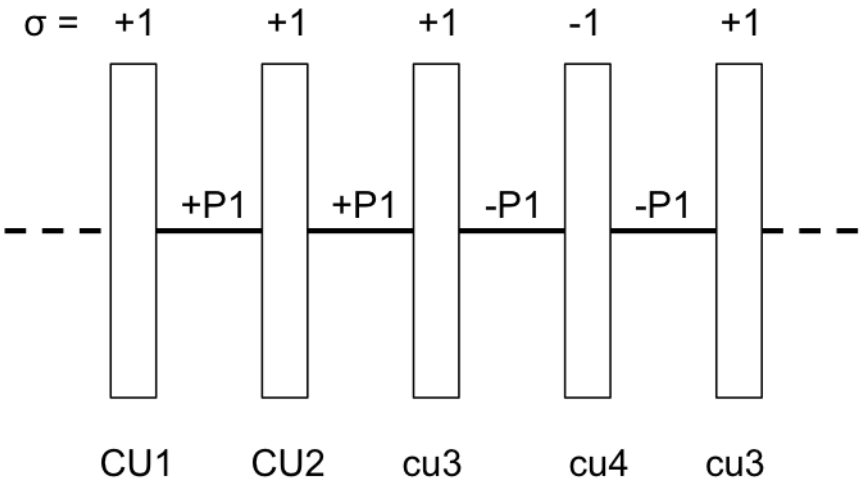


Figure 5.9: Interactions between various chemical units in a part of model crystal 1. The sign of the interaction parameter P1 depends on the product $\sigma_i\sigma_{i-1}$.

After the energy expression for the total interaction energy of the crystal is defined, the next step is to minimize the total interaction energy and to obtain the equilibrated crystal. This is achieved via a Monte Carlo simulation.

A brief introduction to this method was given in §1.3.1. Recalling the basic idea of the method, the simulation starts by choosing two CUs in the initial crystal randomly followed by a swap between them. If the total interaction energy of the new configuration ($E_{tot}^{new}$) of the crystal is lower than that of the crystal configuration before the swap ($E_{tot}^{old}$), the new crystal configuration is maintained and stored. If on the other hand, the new energy is higher than the previous, the new configuration is maintained with a probability based on a Boltzmann distribution as given by Proffen & Welberry (1998).

$$P = \frac{exp\left(\frac{-\Delta E_{tot}}{kT}\right)}{1+exp\left(\frac{-\Delta E_{tot}}{kT}\right)} \qquad (5.5)$$

where $P$ is the transition probability and $\Delta E_{tot} = E_{tot}^{new} - E_{tot}^{old}$. $T$ is the absolute temperature and $k$ is the Boltzmann constant. The number of swaps required to visit each and every layer in the crystal at least once on average is called one Monte Carlo (MC) cycle. The swapping of layers within a MC cycle stops when the number of swaps reached its limit. The crystal at equilibrium is signaled by $\Delta E_{tot} = 0$. This will require several Monte Carlo cycles. Energy as a function of cycle number for the model crystal 1 is shown in Fig. 5.10. Convergence of energy is reached in less than 10 MC cycles.

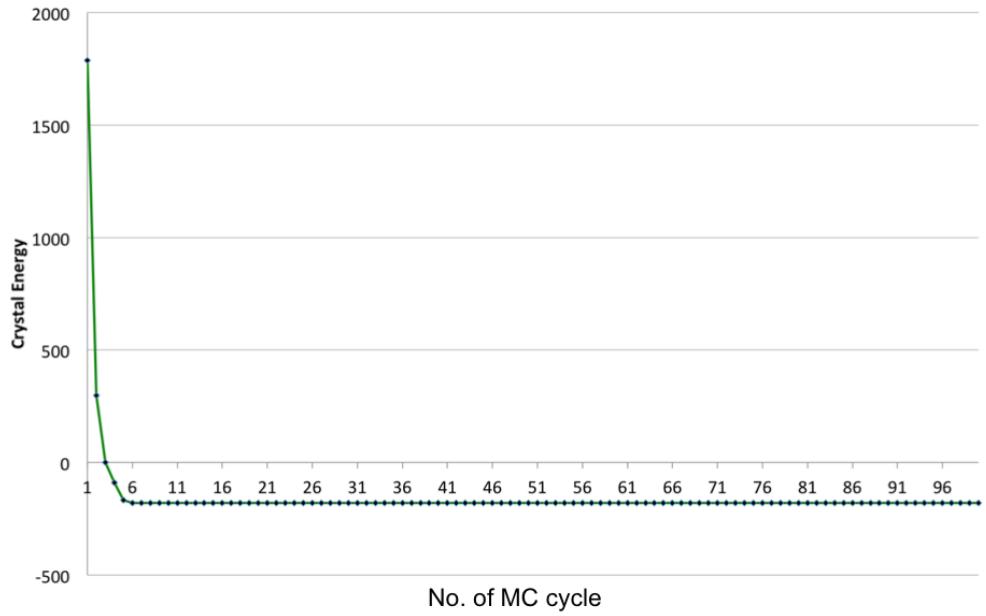


Figure 5.10: Crystal energy as a function of number of Monte Carlo cycles.

In the next step, the energy-equilibrated crystals from both models were used to compute probabilities of occurrence for chemical units and the conditional probabilities of occurrence for different pairs of CUs. As shown in Table 5.3, in model crystal 1, the occupancies of CU1

and CU2 are very similar and both are ~0.9. Those of cu3 and cu4 are also very similar and both are ~0.1. This result is expected because the crystal was built under the constraint that the probabilities of occurrence of the CUs correspond to the occupation factors of the average structure. In model crystal 2, occupancies of CU1 and cu2 are ~0.63 and ~0.37 respectively. Values supplied for the modeling are 0.65 and 0.35 for CU1 and cu2 respectively.

It is worth mentioning that the compositions of both model crystals 1 and 2 do not depend on the interactions between CUs. Therefore, the compositions given in Tables 5.3 and 5.4 are also obtained with corresponding random crystals.

Table 5.3: Compositions of the two model crystals at energy equilibrium.

| Chemical Unit | Sym. Operation | Occupancy |
|---|---|---|
| **Model crystal 1** | | |
| CU1 | X, Y, Z | 0.899 |
| CU2 | X, Y, Z | 0.922 |
| cu3 | X, Y, Z | 0.101 |
| cu4 | X, Y, Z | 0.078 |
| CU1 | -X, -Y, -Z | 0.904 |
| CU2 | -X, -Y, -Z | 0.905 |
| cu3 | -X, -Y, -Z | 0.096 |
| cu4 | -X, -Y, -Z | 0.095 |
| **Model crystal 2** | | |
| CU1 | X, Y, Z | 0.625 |
| cu2 | X, Y, Z | 0.375 |
| CU1 | -X, -Y, -Z | 0.658 |
| cu2 | -X, -Y, -Z | 0.342 |

Crystal statistics of both models show that the chosen crystal size is sufficiently large to nearly reproduce the composition of the average crystals. In general, the larger the model crystal the closer the occupancies to the real values. This statistic thus merely serves as a test of the correctness of the composition used in the modeling procedure.

Table 5.4: Conditional probabilities for different pairs of CUs for the two model crystals at energy equilibrium. The vector given correspond to those between two interacting molecules as shown in Figs. 4.7 and 4.8 for model crystal 1 and 2, respectively. Translated versions of M3''' and m3''' are indicated by (-**a**).

| Vector | Vec. components | Condition | Probability |
|---|---|---|---|
| **Model crystal 1** | | | |
| M3'''(-a) → M1 | ¼, -0.42, ¼ | P {CU1(X,Y,Z) \| CU1(-X,-Y,-Z)} | 0.896 |
| M3'''(-a) → m1 | ¼, 0.42, ¼ | P {cu3(X,Y,Z) \| CU1(-X,-Y,-Z)} | 0.104 |
| M1'' → M3' | -¼, 0.42, -¼ | P {CU2(X,Y,Z) \| CU2(1-X,-Y,-Z)} | 0.915 |
| M1'' → m3' | -¼, -0.42, -¼ | P {cu4(X,Y,Z) \| CU2(1-X,-Y,-Z)} | 0.085 |
| m3'''(-a) → M1 | ¼, 0.42, ¼ | P {CU1(X,Y,Z) \| cu3(-X,-Y,-Z)} | 0.927 |
| m3'''(-a) → m1 | ¼, -0.74, ¼ | P {cu3(X,Y,Z) \| cu3(-X,-Y,-Z)} | 0.073 |
| m1'' → M3' | -¼, -0.42, -¼ | P {CU2(X,Y,Z) \| cu4(1-X,-Y,-Z)} | 0.989 |
| m1'' → m3' | -¼, 0.74, -¼ | P {cu4(X,Y,Z) \| cu4(1-X,-Y,-Z)} | 0.011 |
| **Model crystal 2** | | | |
| P1''' → F2'' | -¼, 0.42, -¼ | P {CU1(X,Y,Z) \| CU1(-X,-Y,-Z)} | 0.620 |
| F2'' → P3' | -¼, 0.42, -¼ | | |
| P1''' → F2'' | -¼, 0.42, -¼ | P {cu2(X,Y,Z) \| CU1(-X,-Y,-Z)} | 0.380 |
| F2'' → p3' | -¼, -0.42, -¼ | | |
| p1''' → F2'' | -¼, -0.42, -¼ | P {CU1(X,Y,Z) \| cu2(-X,-Y,-Z)} | 0.635 |
| F2'' → P3' | -¼, 0.42, -¼ | | |
| p1''' → F2'' | -¼, -0.42, -¼ | P {cu2(X,Y,Z) \| cu2(-X,-Y,-Z)} | 0.365 |
| F2'' → p3' | -¼, -0.42, -¼ | | |

Conditional probabilities contain information about the occurrence of layer pairs in the model crystal. For example, in model crystal 1, P {CU1(X,Y,Z) | CU1(-X,-Y,-Z)} = 0.896 means that given CU1 at the layer position -X, -Y, -Z, the probability of finding CU1 at the layer position X, Y, Z is 0.896. This high probability implies that the likelihood of a CU1 (major) being followed by another CU1 (major) is high. Similarly, P {CU2(X,Y,Z) | CU2(1-X,-Y,-Z)} = 0.915 indicates the same trend. The conditional probabilities P {cu3(X,Y,Z) | CU1(-X,-Y,-Z)} = 0.104 and P {cu4(X,Y,Z) | CU2(1-X,-Y,-Z)} = 0.085 indicate that the likelihood of any major occupied

layer (CU*i*) being followed by a minor occupied layer (cu*i*) is low. The probability of a cu*i* to be followed by a CU*i* is very high as indicated by the conditional probabilities P {CU1(X,Y,Z) | cu3(-X,-Y,-Z)} = 0.927 and P {CU2(X,Y,Z) | cu4(1-X,-Y,-Z)} = 0.989. This is further implied by having small probability values 0.073 and 0.011 for P {cu3(X,Y,Z) | cu3(-X,-Y,-Z)} and P {cu4(X,Y,Z) | cu4(1-X,-Y,-Z)}, respectively.

Note that for model crystal 2 the conditional probabilities that a CU*i* is followed by another CU*i* and that a CU*i* is followed by a cu*i* are very similar to the occupation factors supplied for the CU*i*'s and cu*i*'s, respectively, during the model building. This is because given a layer, there are only two positions available for the next layer to be placed. The realization of one of these positions is based on the layer occupations.

The conditional probabilities shown in Table 5.4 may not be the final values as the interaction parameters (*J* and possibly non-nearest neighbor interactions) may not have their final values. Final values of interaction parameters are obtained only via a global optimization process such as differential evolution (Weber & Bürgi, 2002). However, the Fourier transforms of the model crystals 1 and 2 with the given conditional probabilities in Table 5.4 show that they are sufficient to carry out a qualitative comparison with the experimental data.

## 5.4 Intensity calculation and qualitative analysis of models

The calculated diffraction patterns from the two model crystals were visually compared with the experimental data. The Fourier transform of just a single layer unit shown in Fig. 4.3 is given in section 4.2.3.2 is repeated here:

$$F(\boldsymbol{h}kl) = 2\left[\sum_i cos2\pi(\boldsymbol{h}x_i + ky_i + lz_i) + \sum_i cos2\pi(\boldsymbol{h}x_i - ky_i + lz_i)cos2\pi\left(\frac{k}{2} + \frac{l}{2}\right)\right]$$

where ***h*** is the continuous variable in the **a*** direction perpendicular to the molecular layers. The calculated *h*3*l* section of the layer form factor corresponding to an ordered layer of the average model 2 is shown on the right side of Fig. 5.11. This has to be compared with the corresponding section of the experimental pattern shown on the left.

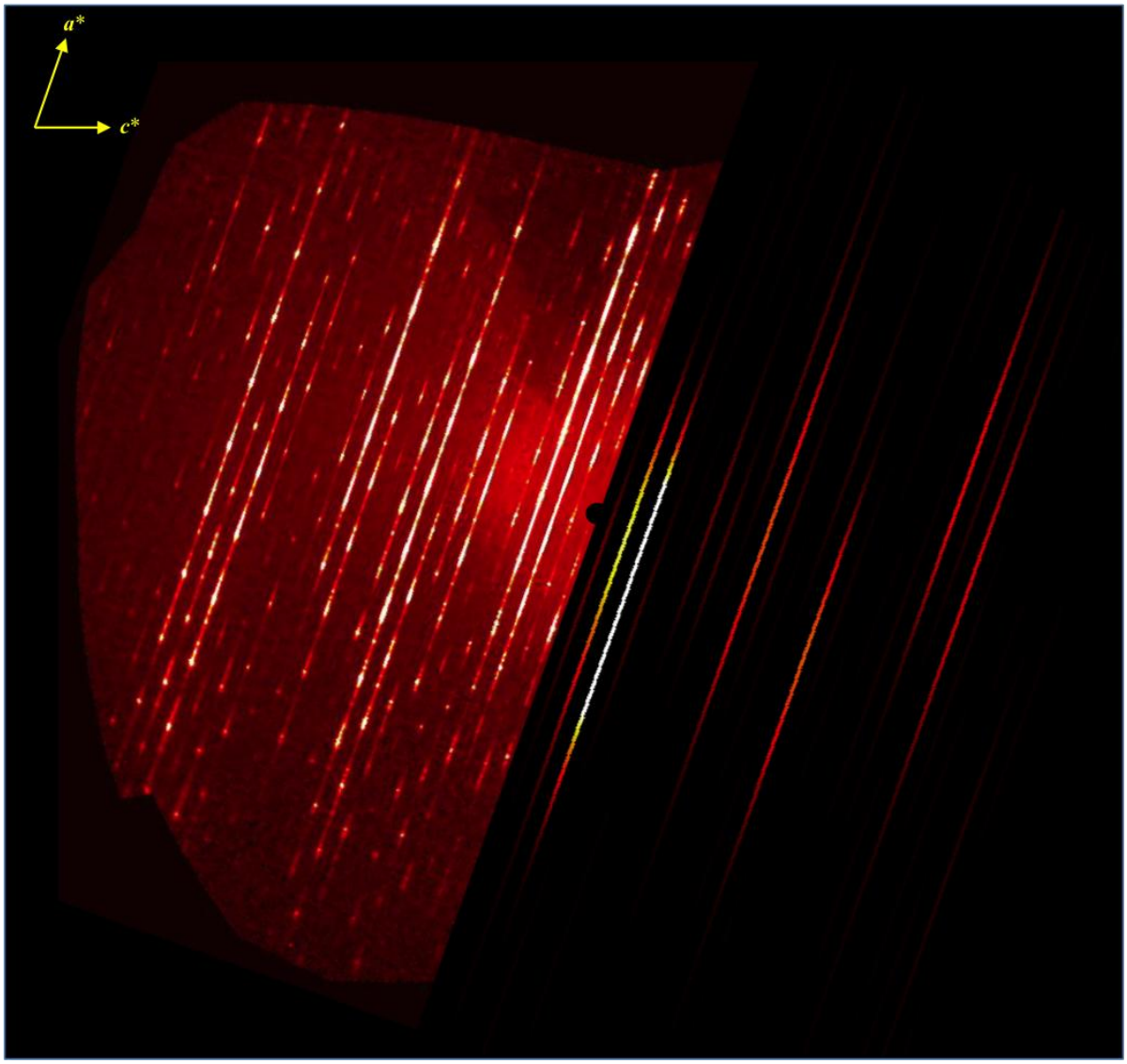


Figure 5.11: *h*3*l* section of the experimental diffraction pattern (left) and the Fourier transform of the layer form factor (right: rotated by 180° about the common origin indicated by a small circle).

As one can clearly see, the intensity variation of the whole pattern as a function of *l* is very similar in both patterns. The high intensity lines in both patterns are of particular interest. Intensity modulation along these lines (along ***h***) depends on the degree of order of the layer stacking along **a**; the continuous fall-off of intensity of the lines in the single layer form factor is due to the fall-off of the atomic form factors at higher scattering angles and the damping of the intensities by thermal motion. The distribution of the intensity in reciprocal space is determined by the layer form factor while the modulation of the intensity is coming from the degree of order of the stack. If it is a perfectly ordered stack of layers, no diffuse scattering will be observed. If on the other hand, the stack is totally random, no modulation of the diffuse scattering will be observed.

The intensities for both model crystals were calculated according to eq. 2.40 (§2.1.1.1.2.1) given in chapter 2. For β-P.R.170, this equation can be written as follows.

$$I_N(\boldsymbol{h}) = |F|^2\{1 + 2\sum_{m=1}^{\infty}(N - |m|)(1-\alpha)^{|m|}cos(2\pi \boldsymbol{h} m)\} \qquad (5.6)$$

where *F* is the layer form factor. All other symbols were introduced in chapter 2. The term $N - |m|$ can be rewritten as $N\left(1 - \frac{|m|}{N}\right)$.

If $|m|$<< N then $1 - \frac{|m|}{N} \approx 1$. Therefore eq. 5.6 can be written as

$$I_N(\boldsymbol{h}) = |F|^2\{1 + 2N\sum_{m=1}^{\infty}(1-\alpha)^{|m|}cos(2\pi \boldsymbol{h} m)\} \qquad (5.7)$$

If the layer stack is completely random (i.e. $\alpha = 0$ ), then eq. 5.7 takes the form

$$I_N(\boldsymbol{h}) = |F|^2\{1 + 2N\sum_{m=1}^{\infty} cos(2\pi \boldsymbol{h} m)\} .$$

Fig. 5.12 shows the *h*0*l* sections from random model crystals 1 and 2 and compares them with the experimental data. Both calculated sections were made using the same intensity scale, which differs from the intensity scale of the experimental section. The software available for manipulating the experimental intensities did not have sufficient flexibility to adjust the scale as desired. Note that the color scheme in the calculated patterns has been chosen such that the variations in the diffuse features are visible. This choice comes at the expense of not distinguishing the intensities of the Braggs.

The reciprocal lattice section *h*0*l* corresponds to the projection of the crystal structure down **b**. If the CU*i*'s differed from the cu*i*'s only by the translation vector (0, 0.16, 0), the crystal structure would be ordered in this projection and the *h*0*l* reciprocal lattice section should not contain diffuse scattering. However, both calculated and experimental *h*0*l* sections do show diffuse streaks along **a***, which indicates that there are structural differences between the CU*i*'s and the cu*i*'s in addition to the (0, 0.16, 0) translation. These additional differences have not been discussed in chapter 4 because they are small. The corresponding section calculated from the layer form factor shows a similar variation in the intensity. Thus the diffuse streaks in Figs. 5.12 a) and b) arise from the layer form factor. There are a few notable differences between the two calculated patterns. The diffuse streak at *l* = 0 is only present in a), but not in b). It is also present in the Fourier transform of the layer form factor (not shown). The streak at *l* = 21 is more intense in a) than in b). The opposite is true for the streak

at $l$ = 3. These variations between the two patterns may be due to the different degrees of out-of-plane warping of the layer-structural units of the two model crystals.

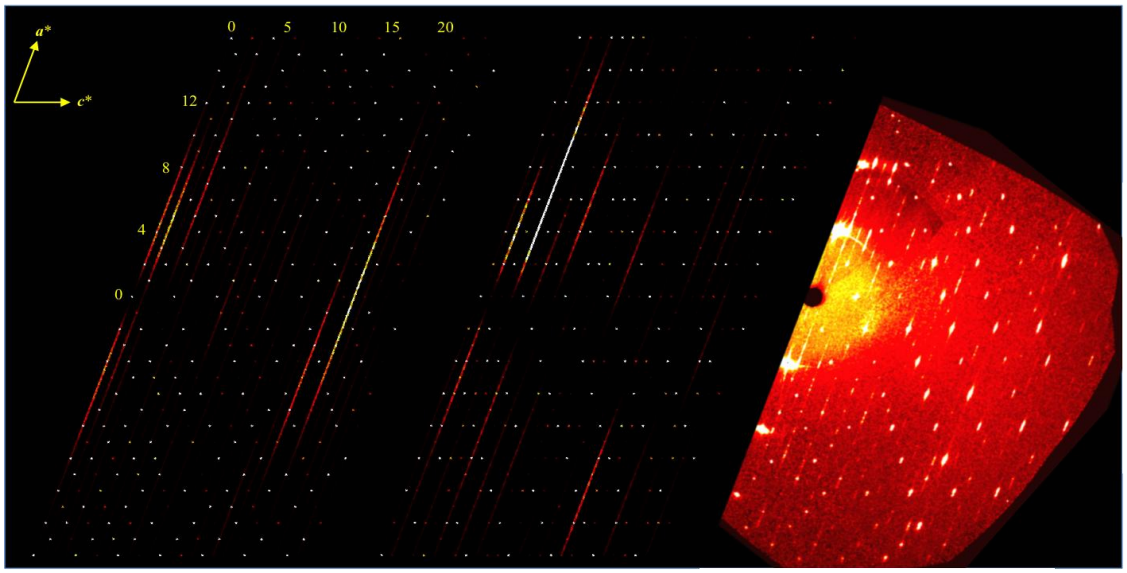


Figure 5.12: *h*0*l* reciprocal lattice sections a) and b) calculated from random model crystals 1 and 2, respectively. c) The corresponding section of the experimental diffraction pattern.

Fig. 5.13 shows the *h*3*l* section calculated from random model crystals 1 and 2. The diffuse scattering seen in both calculated patterns does not show modulation and is thus purely the contribution of the layer form factor (see Fig. 5.11). The tailing of higher angle peaks in the experimental pattern Fig. 5.13(c) is not present in either calculated pattern. This is expected because the models are random, assuming no interactions between the layers, albeit, as always, with average structure constraints on the average occupancies of the different alternative positions for the molecules.

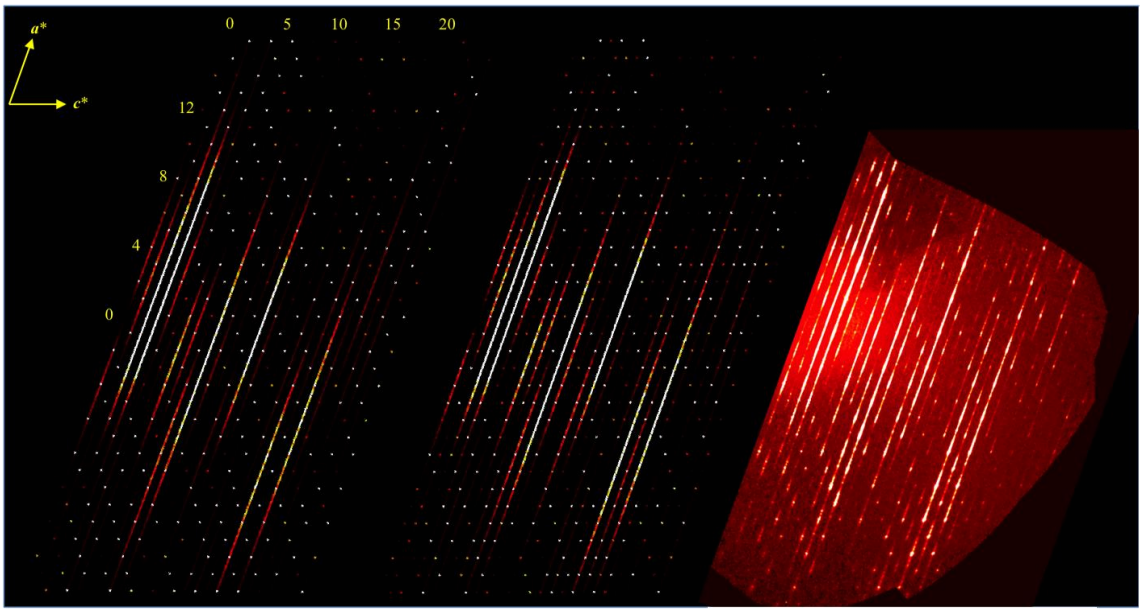


(a) (b) (c)

Figure 5.13: *h3l* reciprocal lattice sections a) and b) calculated from random crystals for model 1 and 2, respectively. c) The same section reconstructed from experimental data.

When the crystal deviates from a random sequence of layers, which, as described above, is only possible for model crystal 1, the diffuse scattering exhibits a fine structure in accordance with eq. 5.7. Fig. 5.14 shows the *h*2*l* section of the reciprocal space calculated from both model crystals 1 and 2. The interaction parameter for model 1 is P1 = -P4 = -0.65.

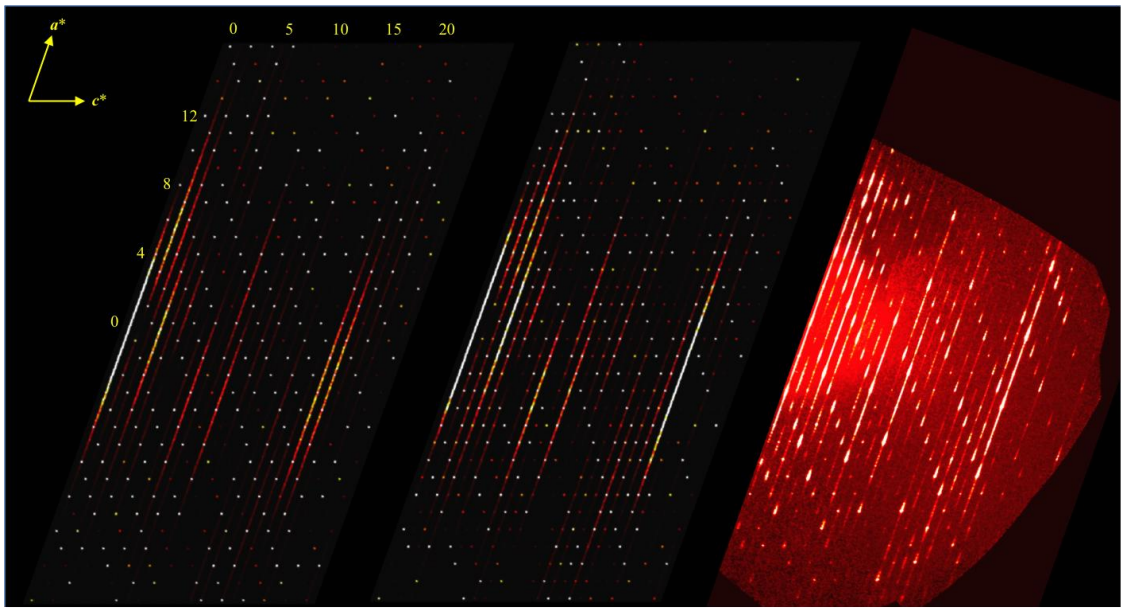


(a) (b) (c)

Figure 5.14: *h*2*l* reciprocal lattice sections a) and b) calculated from model crystals 1 and 2, respectively. c) The corresponding section reconstructed from the experimental data.

Both calculated plots Fig. 5.14 a) and b) were drawn using the same intensity scale. Except for the contribution from the layer form factor, it is difficult to see any evidence of structured diffuse scattering in either pattern. The tailing of higher angle reflections in c) is not seen in any of the calculated plots. Since pattern b) comes from model crystal 2 with equal interaction energies between all layers, it should not show structure in the diffuse scattering. In order to see the fine structure in the scattering, 1D plots along some selected streaks were constructed.

Fig. 5.15 shows the 1D plot of the H20 profiles obtained from the two model crystals and the corresponding experimental profile. The intensities have been calculated using the same grid that was used for the experimental data processing. The size of this grid is 20 × 40 × 40 (= $h$ × $k$ × $l$) and the resolutions along the three unit cell vectors are 0.01$h$, 0.1$k$ and 0.1$l$, respectively. The diffuse streaks run along $h$ and hence $h$ has 10 times finer resolution than $k$ and $l$. The lower and the upper limits of $h$ are -10 to +10, respectively. These $h$ limits were dictated by the availability of the experimental data. The horizontal axis of the plot varies from H = 0 to 2000, corresponding to $h$ = -10 and +10, respectively. The vertical axis represents the intensity in arbitrary units. The figure shows a zoomed-in view with the intensity of the Bragg reflection cut off at 10 so that the fine variation in the weaker diffuse scattering is clearly visible. Note that in order to obtain an overlay of the broad observed and calculated diffuse scattering intensities adjusted to approximately the same vertical scale , the calculated intensities have been scaled by an arbitrarily chosen factor of $2.5\times10^{-8}$. H20 is a symmetric profile as the 2-fold axis is perpendicular to $h$ at $h$ = 0 (H = 1000). All even Bragg reflections in all profiles (calculated and experimental) are orders of magnitude more intense than the nearby diffuse signals. In particular, the Bragg reflections -620; -420; -220; 020; 220; 420 and 620 are very strong. The Bragg reflections with $h$ odd from model crystal 2 (red plot) are much stronger than nearby diffuse signals, but not as strong as $h$ even reflections. The intensities of these reflections in the blue plot from model crystal 1 are virtually zero as predicted by the average space group symmetry of model crystal 1, which would require $h$ odd reflections in H20 to be systematically absent.

In general, the Bragg intensities with $h$ even from model crystal 1 (blue line) are more intense than those from model crystal 2 (red line). On the other hand, the diffuse signals from model crystal 2 are somewhat stronger than those from model crystal 1. This is because the total intensity in reciprocal space for a given amount of material is a constant, but can be

distributed differently between Bragg and diffuse scattering depending on the degree of order in the samples.

The non-Bragg scattering in the experimental plot in Fig. 5.15 contains broad diffuse scattering features dominated by sharp satellite peaks. The broad diffuse scattering appears as several “humps” lying predominantly between the Bragg reflections. In contrast, the two calculated patterns (blue and red) show only a single very broad Gaussian-like “hump” centered about $h = 0$ and extending over nearly the entire width of the pattern. A great deal of fine structure is superimposed on this diffuse pattern, however it is not known at this stage if this fine structure arises from some form of modulation in the calculated structures or if it comes from statistical noise from the Monte Carlo calculations. Further lengthy calculations to try to ascertain the true cause of this fine structure are necessary, but are outside the scope of this thesis. Note the smaller hump-like structures about the Bragg reflections at h = 0, ±2, ±4 and ±6 in the red plot for model crystal 2, but not in the blue plot for model crystal 1. No intensities within the region of the humps in the calculated plots go to zero.

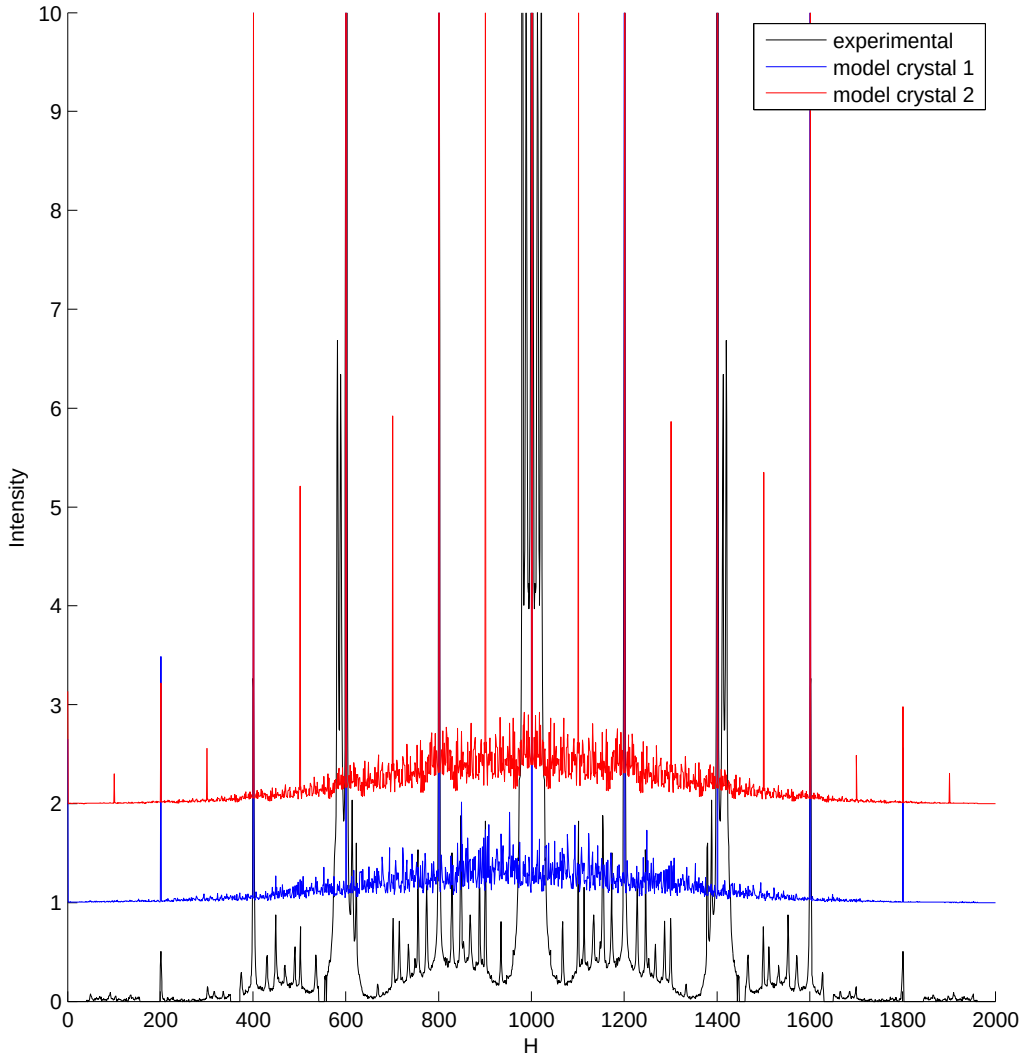


Figure 5.15: Traces of the H20 profile. The scale factor between the calculated and the experimental plots is $2.5\times10^{-8}$. Bragg peaks at integer multiples of 100, $h$ = 0 at H = 1000. Note that the red and the blue plots have been moved up with respect to the black plot by 2 and 1 intensity units, respectively, for clarity.

Fig. 5.16 shows the H30 profiles. In order to show the features of the diffuse scattering in the calculated plots clearly, the scale factor between the calculated and the experimental plots was arbitrarily chosen to be $1\times10^{-7}$.

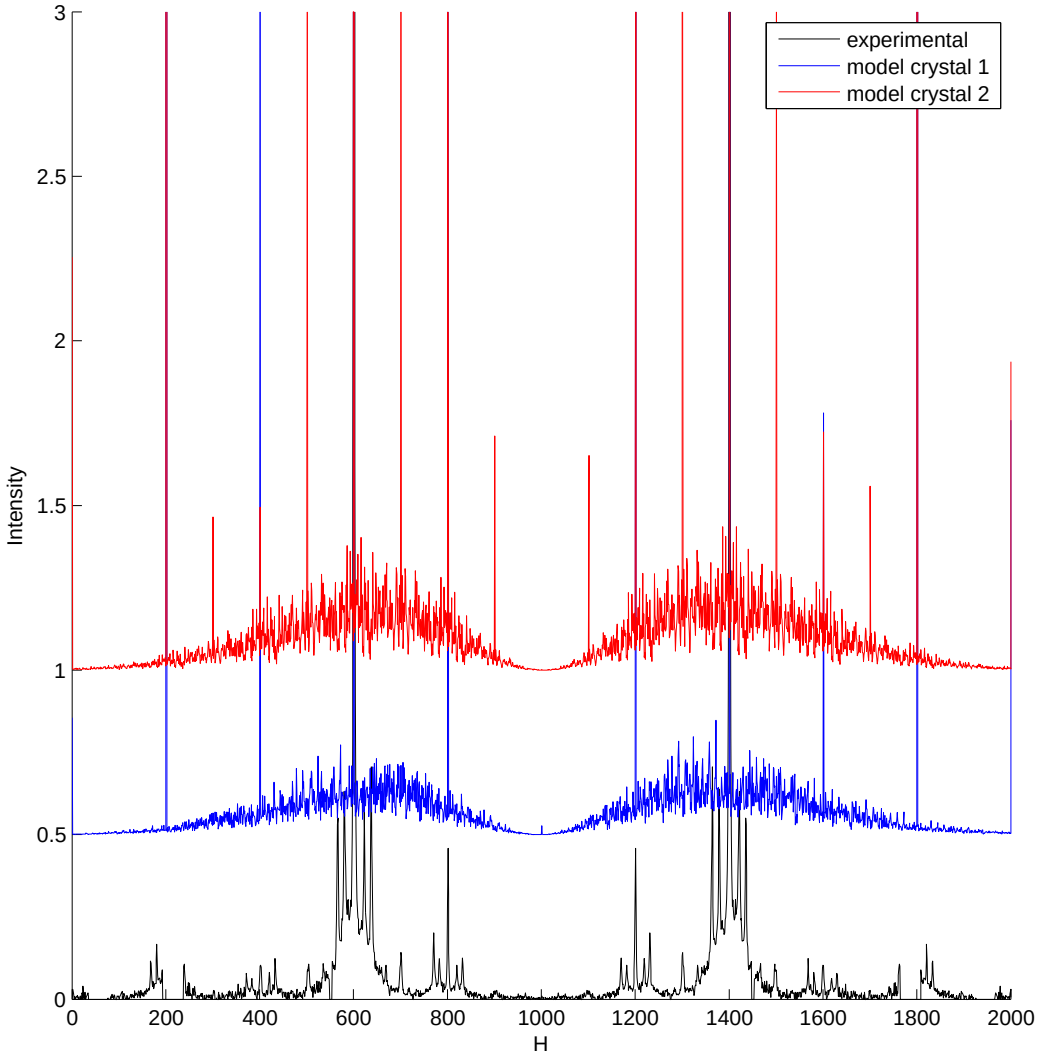


Figure 5.16: The H30 profile. Note that the blue and the red plots have been moved up relative to the black plot by 0.5 and 1 intensity units, respectively for clarity.

The experimental pattern is symmetric about $h = 0$. Narrow regions of strong diffuse scattering are centered about $h$ even reflections, except for $h = 0$ where the diffuse scattering is zero. Superimposed satellite peaks modulate the broad diffuse scattering features. Note that the intensities of the satellite peaks are asymmetrically distributed about their Bragg peak.

Unlike in the experimental patterns, both calculated patterns do not strictly maintain 2-fold symmetry about $h = 0$. Gaussian-like broad regions of diffuse scattering in the calculated plots are centered about $h = -4$ and 4 and extend from $h = 0$ to high $|h|$. Similar to the experimental pattern, the diffuse intensity at $h = 0$ is zero. Fine sharp features that modulate the broad

diffuse scattering are also present, however, as before, it is difficult to decide if this fine structure is due to a degree of order present in the calculated crystals, or arises from statistical noise in the calulations.

The lack of 2-fold symmetry about $h = 0$ in the calculated patterns can be explained in two ways. Firstly, one can argue that the fine structure in the pattern is coming solely from the statistical noise, which is randomly distributed in the calculations, so that it is very likely that the 2-fold symmetry is lost. Secondly, it is also possible that some fine structure comes from the crystal stacking sequences and does have 2-fold symmetry, but that statistical noise on top of this fine structure destroys the symmetry. Therefore, it is very important to remove as far as possible the statistical noise contribution to the calculated pattern. This can be achieved by running a much larger number of simulations. If the fine structure in the calculated pattern is due solely to statistical noise, it will be smoothed out into broad Gaussian-like features when the average intensity is derived. On the other hand, if the fine structure persists when the number of simulations increases, the fine structure is real. Such a test, which involves very lengthy calculations, has not been performed in the current study due to time constraints.

The basic features of the satellite peaks in the experimental H*kl* profiles are presented next. The initial investigations of the satellite peaks in the diffraction pattern from this compound showed that there is possibly more than one set of satellite peaks. For example, the satellite peaks about the Bragg reflections at H = 200, 600, 1000, 1400, 1800 in the experimental H20 profile are shown in Fig. 5.18 below. Note that the distance between the first satellite and the main (Bragg) peak is not equal to the distance between the first and the second satellites.

The distribution of satellite peaks about the Bragg reflections is asymmetric in high angle profiles. For example, Fig. 5.19 shows the distribution of satellite peaks in the H 2 10 profile at H = 400, 800, 1200 and 1600. The asymmetric distribution of satellite peaks is nicely visible.

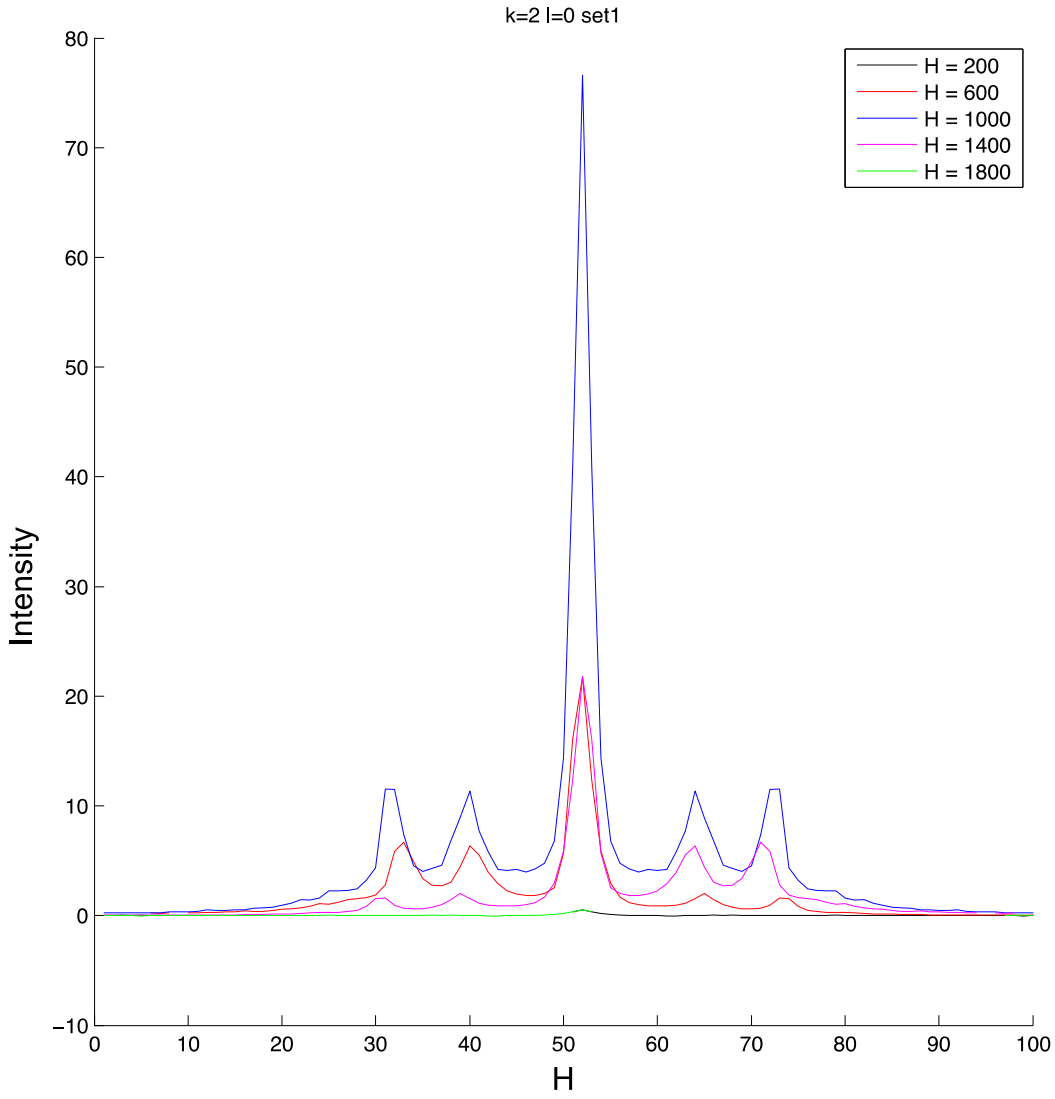


Figure 5.18: Distribution of the satellite reflections about the Bragg reflections in the experimental H20 profile. Horizontal axis: reciprocal axis range $h$-0.5 ≤ $h$ ≤ $h$+0.5; vertical axis: intensity.

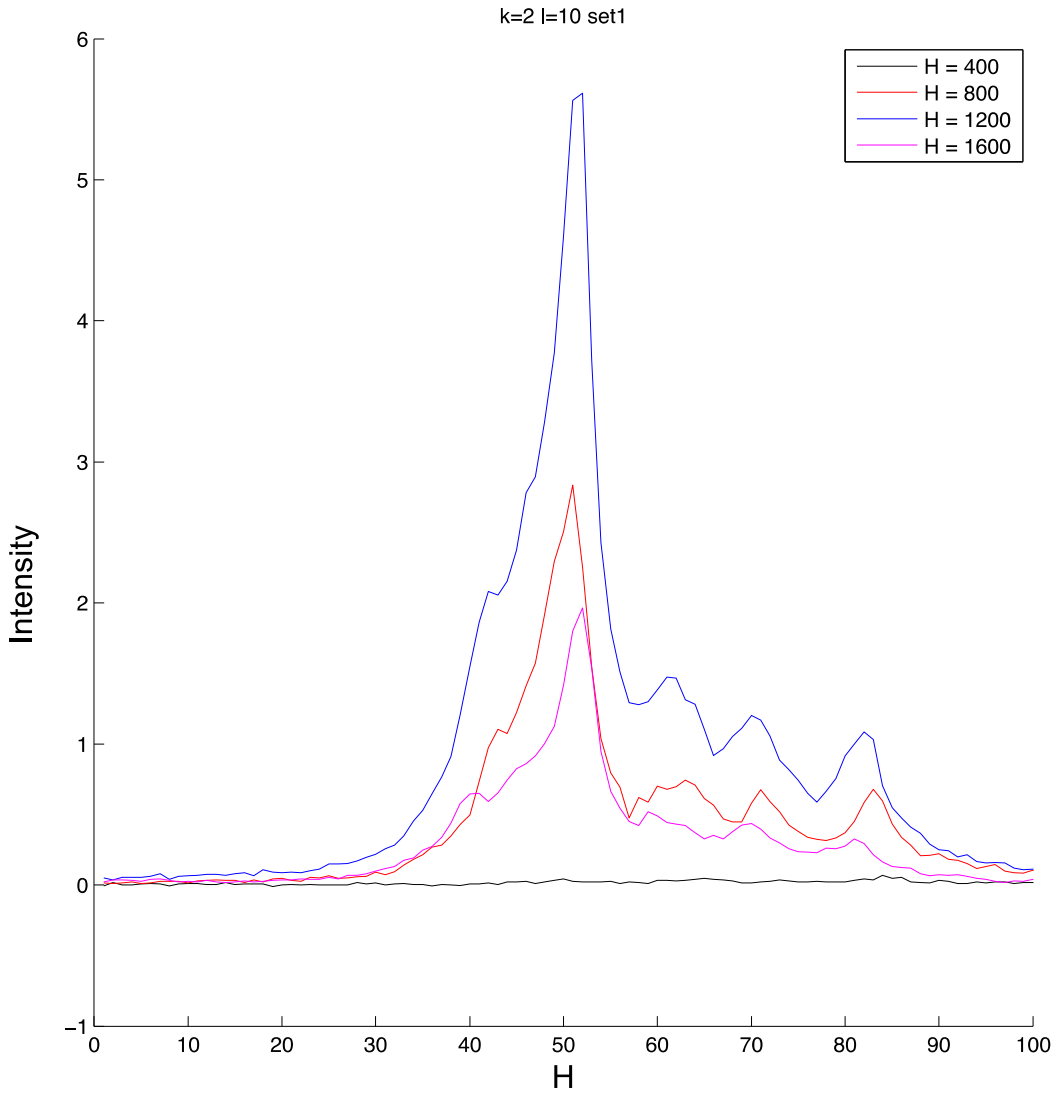


Figure 5.19: Distribution of satellite reflections about the Bragg reflections in the experimental H 2 10 profile. Horizontal axis: reciprocal axis range $h$-0.5 ≤ $h$ ≤ $h$+0.5; vertical axis: intensity.

## 5.5 Summary and Conclusions

Initial attempts at modeling of the local structure of the β-phase of Pigment Red 170 have been made. First the two average structures were disentangled into physically occurring and chemically feasible units, called “Chemical Units (CUs)”. Starting with different CUs obtained from the two different average structures described in chapter 4, two random crystals were built. Random crystals do not contain correlations between CUs. In the next step, correlations between CUs were introduced and the interaction energy of each model crystal was calculated and minimized according to the Monte Carlo method. The Monte Carlo optimized crystals were then used for the intensity calculation.

The disordered model crystals tested in this work produced broad diffuse scattering features superimposed with some sharp fine features. The fine features might be due to some underlying order of molecular layers in the model crystals, but could also be a contribution from statistical noise in the calculations. Therefore, prior to any conclusion, the origin of the fine, sharp diffuse scattering features ("satellites") must be investigated further in future work.

## 5.6 Bibliography

Berliner, R. & Werner, S. A. (1986). *Phys. Rev*. B, **34**, 3586-3603.

Chodkiewicz, M., Ahrenberg, L., Weber, T. & Bürgi, H. -B. (2014). *Zürich Oak Ridge Disorder Simulation (ZODS)* User Manual, unpublished.

Ermrich, M., Hahn, F. & Wölfel, E. R. (1997). *Textures and Microstructures*, **29**, 89-101.

Estermann, M. A. (2001). *XCAVATE* User Manual Version 3.5.

Kabsch, W. (1988). *J. Appl. Cryst*. **21**, 67-71.

Kabsch, W. (1993). *J. Appl. Cryst*. **26**, 795-800.

Kraft, P. (2010). *PILATUS 2M. A Detector for Small Angle X-ray Scattering*, (Doctoral dissertation).

marXperts (2014). Private communication.

Proffen, Th. & Welberry, T. R. (1998). *Phase Transitions: A Multilingual Journal*, **67**, 373-397.

Teteruk, J. L., Glinnemann, J., Gorelik, T. E., Linden, A. & Schmidt, M. U. (2014). *Acta Cryst*. B**70**, 296-305.

Truesense Imaging Inc. (2012). "*CCD IMAGE SENSOR NOISE SOURCES*" Reference Document.

Weber, T. & Bürgi, H.-B. (2002). *Acta Cryst*. A**58**, 526-540.

Welberry, T. R. (2004). *Diffuse X-Ray Scattering and Models of Disorder*, Oxford: Oxford University Press.

# Conclusions and Outlook

The single-crystal X-ray diffraction pattern from the β-phase of the industrially important Pigment Red 170 (β-P.R.170) consists of a difficult-to-disentangle mixture of Bragg diffraction superimposed by rods of diffuse scattering and satellite peaks. This extremely complicated diffraction pattern illustrates the complexity of real world crystals, whose underlying structure is far from the concept of a crystal being a regular periodic arrangement of unit cells usually presented in introductory crystallography textbooks. Such complex structures still present a big challenge to practitioners of X-ray crystallography.

Rods of diffuse scattering indicate that the structure is one-dimensionally disordered, or in other words contains stacking faults. The P.R.170 molecules are nearly planar and arrange themselves into planar layers, which then stack in a disordered sequence in the crystal. This arrangement manifests itself in the diffraction pattern as rods of diffuse.

The rods of diffuse scattering pass through most Bragg reflections. As a consequence, obtaining a reliable orientation matrix for integration and accurate Bragg intensities is difficult and not well catered for my conventional integration software. Furthermore, analysis of systematic absences leads to ambiguity in the choice of space group. While such space group ambiguities are usually resolved by the structure being solvable and chemically reasonable in only one of the possible space groups, in the P.R.170 case, two completely plausible and different average structures in different space groups, $B2_1/g$ and $P2_1/a$, were obtained. The two models differ in their space group symmetry, the number of molecules in the asymmetric units, the site occupation factors of the molecules, and their placement in the unit cell and the number of crystallographic and non-crystallographic symmetry elements in the average unit cell. One model is built from one type of symmetry-independent disordered layer, while the other model is built from two independent layers, one of which is ordered and the other disordered.

The two models are similar in the following ways. The structure of the basic layer in both models is the same. It possesses the layer group symmetry $p\ 1\ 2_1/c\ 1$. These units are stacked along **a***. In both models, the geometry of any adjacent layer pair in the stack of layers is the same. According to Order-Disorder theory, these two models are two members of the same polytypic family although the $B2_1/g$ model is an MDO (maximum degree of order) type, while the $P2_1/a$ model is a non-MDO type. They differ only by their stacking of layers. In the end, even after extensive subgroup analysis, it was not possible to unequivocally choose which model was correct based on the Bragg data alone. This open question can only be answered once the full local structure is understood, which requires detailed modeling of the disorder and comparison of the calculated and experimentally observed diffuse scattering.

The modeling of the local structure was then attempted. Two model crystals were constructed in the computer with the aid of a random number generator using the disentangled chemical units (CUs) from the two average structures. The correlations between the CUs were introduced and the total interaction energy of each crystal was minimized according to the Monte Carlo (MC) method. The MC minimized crystals were then used to calculate total scattering intensities.

Both disordered models tested in this work produced broad diffuse scattering features superimposed with some fine structure. It has not been feasible at this stage to determine if the observed fine structure in each calculated pattern is due to some underlying periodicity of molecular layers in the model crystal or is just a consequence of the statistical noise in the MC simulations. This question can be answered by running a much larger number of simulations followed by averaging the calculated intensities, although this is computationally expensive.

A visual comparison between the calculated and the experimental diffuse scattering of a few selected profiles showed that the fit is poor. After eliminating any possible statistical noise, further improvements to the interaction parameters could help to achieve a better fit to the experimental pattern. The optimization of the interaction parameters, which has not been performed in the current study, can be achieved via a global optimization method such as differential evolution.

A further step would be to improve the interaction models of both crystals. Additional interactions between the CUs beyond the immediate nearest-neighbors might be included when optimizing the constructed crystal. Since model crystal 1 is based on an MDO type average structure, according to OD theory, interactions involving additional shells of

neighbors can play an important role in the layer stacking. The model crystal 2 currently employs equal interactions between the second-nearest neighbors. Since this crystal is based on a non-MDO type average structure, the second-nearest neighbor interactions may not necessarily be equal. Therefore, the interaction model of the model crystal 2 may be improved first by differentiating the interactions according to the geometric equivalence of the interacting pairs and then by incorporating the higher order interactions.

The work in this thesis is a significant first step in elucidating the full local structure of β-P.R.170. However, more work needs to be done to fully derive the local structure, as outlined briefly above.

**Appendix: Crystallographic Information Files (CIF)**

CIFs are available only in electronic version of the thesis.

Average_model1.cif

Average_model2.cif.

They are also available from the International Union of Crystallography electronic archives *via* journals.iucr.org (search keyword: og5065).